UNIVERSITY OF CALIFORNIA, SAN DIEGO

Optimizing Cone Beam Computed Tomography (CBCT) System for Image Guided Radiation Therapy

A dissertation submitted in partial satisfaction of the requirements

for the degree Doctor of Philosophy

in

Electrical Engineering (Photonics)

by

Chun Joo Park

Committee in charge

Professor Zhaowei Liu, Chair
Professor Sadik Esener
Professor Steve Jiang
Professor Yu-Hwa Lo
Professor Todd Pawlicki
Professor William Song

2013

The dissertation of Chun Joo Park is approved, and it is acceptable in quality and form for publication on microfilm and electronically:

_____

_____

_____

_____

_____

_____

Chair

University of California, San Diego

2013

Dedication

To my supervisors, family, friends, and colleagues,

I would like to take this opportunity to express my sincere gratitude to all those who have supported me to complete this thesis. This thesis could not have been accomplished without the help of you all.

Table of Contents

List of Figures

List of Tables

Acknowledgements

First of all, I feel tremendously lucky to have had the opportunity to work with my supervisors Dr. William Song, Dr. Bongyong Song and Dr. Zhaowei Liu. I am deeply indebted and thankful for their help, guidance and encouragement during my three years of research at University of California, San Diego. It has been my greatest fortune to have them as academic supervisors.

I also would like to gratefully acknowledge Dr. Sung Ho Park, Dr. Jin Sung Kim and Dr. Ho Kyung Kim for their endless and unconditional support. I will always remember all the support that you have provided to me and I shall never forget this favor. Truly, you three are the greatest fortune, colleagues and people of my life. Words would not be enough to express my feeling for your tremendous help and support. I will try my best to give back to you in the future.

Special thanks also go to my colleagues, Matthew Webster, Kevin Kauweloa, Tyler Watkins and Daeyup Han at University of California, San Diego, Center for Advanced Radiotherapy Technologies. I am so fortunate to work together with you all who enriched my live and given me so much fun to my academic life.

Last but not least, I want to thank all of my family members, and my wife Jaeeun Chung for their love and support. You have made countless sacrifice for me, and have provided me with steady guidance and encouragement. Jaeeun Chung, all my works and academic accomplishments are dedicated to you.

The text of Chapter 2, in part or in full, is a reprint of the material as it appears in the Journal of Nuclear Instruments and Methods in Physics Research A. The dissertation author was the primary researcher and author, and the co-authors listed in this publication directed and supervised the research which forms the basis for this chapter.

The text of Chapter 3, in part or in full, is a reprint of the material as it appears in the Journal of Technology in Cancer Research and Treatment. The dissertation author was the primary researcher and author, and the co-authors listed in this publication directed and supervised the research which forms the basis for this chapter.

The text of Chapter 4, in part or in full, is a reprint of the material as it appears in the Journal of Medical Physics. The dissertation author was the primary researcher and author, and the co-authors listed in this publication directed and supervised the research which forms the basis for this chapter.

The text of Chapter 5, in part or in full, is a reprint of the material as it appears in the Journal of Medical Physics. The dissertation author was the primary researcher and author, and the co-authors listed in this publication directed and supervised the research which forms the basis for this chapter.

The text of Chapter 6, in part or in full, is a reprint of the material as a recent submission. The dissertation author was the primary researcher and author, and the co-authors listed in this publication directed and supervised the research which forms the basis for this chapter.

The text of Chapter 7, in part or in full, is a reprint of the material as it appears in the Journal of Medical Physics. The dissertation author was the primary researcher and author, and the co-authors listed in this publication directed and supervised the research which forms the basis for this chapter.

Vita

2000~2007 Bachelor of Science in Nuclear Engineering department from Hanyang University, Korea

2007~2009 Master of Science in Medical Physics and Engineering department from the Catholic University of Korea, Korea

2010~2013 Doctor of Philosophy in Electrical Engineering (Photonics) from University of California, San Diego

Publications

Park JC, Kim JS, Park SH, Liu Z, Song B, Song WY. Motion-Map Constrained Image Reconstruction (MCIR): Application to Four-Dimensional Cone-Beam Computed Tomography. Submitted.

Webster MJ, Devic S, Vuong T, Yup Han D, Park JC, Scanderbeg D, Lawson J, Song B, Watkins WT, Pawlicki T, Song WY. Dynamic modulated brachytherapy (DMBT) for rectal cancer. Medical physics 2013;40:011718.

Park JC, Park SH, Kim JH, Yoon SM, Liu Z, Song B, Sandhu A, Kauweloa, Webster MJ, Jiang SB, Mell LK, Mundt AJ, Song WY. Liver motion during CBCT-guided SBRT. Medical physics 2012;39:6431-42.

Park JC, Song B, Kim JS, Park SH, Kim HK, Liu Z, Suh T, Song WY. Fast compressed sensing-based CBCT reconstruction using Barzilai-Borwein formulation for application to on-line IGRT. Medical physics 2012;39:1207-17.

Kauweloa KI, Ruan D, Park JC, Sandhu A, Kim G, Pawlicki T, Watkins WT, Song B, Song WY. GateCT™ surface tracking system for respiratory signal reconstruction in 4DCT imaging. Medical physics 2012;39:492-02.

Park JC, Park SH, Kim JH, Yoon SM, Kim SS, Kim JS, Liu Z, Watkins WT, Song WY. Four-dimensional cone-beam computed tomography and digital tomosynthesis reconstructions using respiratory signals extracted from transcutaneously inserted metal markers for liver SBRT. Medical physics 2011;38:1028-36.

Park JC, Park SH, Kim JS, Han Y, Cho MK, Kim HK, Liu Z, Jiang, SB, Song B, Song WY. Ultra-fast digital tomosynthesis reconstruction using general-purpose GPU programming for image-guided radiation therapy. Technology in cancer research & treatment 2011;10:295-306.

Park JC, Lee HK, Song WY, Achterkirchen TG, Kim HK. Defective pixel map creation based on wavelet analysis in digital radiography detectors. Nuclear Instruments and Methethods in Physics Research A. 2011;634:101-5.

Park JC, Park SH, Kim JS, Han Y, Ju SG, Shin E, Shin JS, Park HC, Ahn YC, Song WY. Digital tomosynthesis for patient alignment system using half-fan mode CBCT projection images. Korean Journal of Medical Physics 2010;21:360-6.

Watkins WT, Li R, Lewis J, Park JC, Sandhu A, Jiang SB, Song WY. Patient-specific motion artifacts in 4DCT. Medical physics 2010;37:2855-61.

Fields of Study

Major field: Electrical Engineering (Photonics)

Studies in Photonics
Professor Zhaowei Liu

ABSTRACT OF THE DISSERTATION

Optimizing Cone Beam Computed Tomography (CBCT) System for Image Guided Radiation Therapy

by

Chun Joo Park

Doctor of Philosophy in Electrical Engineering (Photonics)

University of California, San Diego, 2013

Professor Zhaowei Liu, Chair

Cone Beam Computed Tomography (CBCT) system is the most widely used imaging device in image guided radiation therapy (IGRT), where set of 3D volumetric image of patient can be reconstructed to identify and correct position setup errors prior to the radiation treatment. This CBCT system can significantly improve precision of on-line setup errors of patient position and tumor target localization prior to the treatment. However, there are still a number of issues that needs to be investigated with CBCT system such as 1) progressively increasing defective pixels in imaging detectors by its frequent usage, 2) hazardous radiation exposure to patients during the CBCT imaging, 3)

degradation of image quality due to patients' respiratory motion when CBCT is acquired and 4) unknown knowledge of certain anatomical features such as liver, due to lack of soft-tissue contrast which makes tumor motion verification challenging. In this dissertation, we explore on optimizing the use of cone beam computed tomography (CBCT) system under such circumstances.

We begin by introducing general concept of IGRT. We then present the development of automated defective pixel detection algorithm for X-ray imagers that is used for CBCT imaging using wavelet analysis. We next investigate on developing fast and efficient low-dose volumetric reconstruction techniques which includes 1) fast digital tomosynthesis reconstruction using general-purpose graphics processing unit (GPGPU) programming and 2) fast low-dose CBCT image reconstruction based on the Gradient-Projection-Barzilai-Borwein formulation (GP-BB). We further developed two efficient approaches that could reduce the degradation of CBCT images from respiratory motion. First, we propose reconstructing four dimensional (4D) CBCT and DTS using respiratory signal extracted from fiducial markers implanted in liver. Second, novel motion-map constrained image reconstruction (MCIR) is proposed that allows reconstruction of high quality and high phase resolution 4DCBCT images with no more than the imaging dose used in a standard Free Breathing 3DCBCT (FB-3DCBCT) scan. Finally, we demonstrate a method to analyze motion characteristics of liver that are particularly important for image guided stereotactic body radiation therapy (IG-SBRT). It is anticipated that all the approaches proposed in this study, which are both technically and clinically feasible, will allow much improvement in IGRT process.

Chapter 1 Introduction

1.1 Radiation therapy

Cancer has a profound influence on the lives of every member of the family concerned and it is one of the leading causes of death in the world. There are a number of treatment modalities available to treat cancer, either as stand-alone treatments or as synergetic combinations. There are three main treatment techniques that are frequently used in current clinical settings, which are 1) surgery, 2) radiation therapy and 3) chemotherapy. Radiation therapy, or radiotherapy, utilizes high energy, penetrating waves or particles such as X-rays, gamma rays, proton rays, or neutron rays to destroy tumor cells or keep them from reproducing.[1] It utilizes ionizing radiation in a strictly controlled environment to treat cancer. High energy X-rays, gamma rays, and electron beams are common forms of ionizing radiation used. Ionizing radiation can be administered using external beam therapy or by placing a radioactive material directly into a body tissue or cavity. Radiation therapy works by damaging the DNA within cancer cells thus interfering with the cell's ability to grow and reproduce. Currently, most common cancer types are treated with radiation therapy in some way and it can be used as the primary therapy or combined with surgery, chemotherapy, hormone therapy or some mixture of them. Over past decades, radiation therapy has become the most common way to treat cancer with nearly 2/3rd of all cancers treated with some form of radiation therapy.[2] The ultimate goal of radiation therapy is to deliver maximum radiation dose to the tumor volume while minimizing excessive dose to surrounding healthy tissues or organs surrounding the tumor.

1.2 Evolution of radiation therapy

The history of radiation therapy began with the discovery of X-rays by Wilhelm Rontgen in 1895, where the internal structures of the body could be made visible without the necessity of surgery.[3, 4] Soon after the groundbreaking discovery, in 1898, Nobel Prize winning scientists [5], discover the radioactive elements polonium and radium and notice that radiation from radium killed diseased cells. This was the first historical event of radiation therapy where radiation took a role not just in diagnosis but also in treatment. During World War I and II, physicists and engineers, continued to develop higher energy X-ray machines to produce high energy, deeply penetrating beams to treat deep-seated tumors. In the 1960s, the revolutionary megavoltage high energy treatment machine called linear accelerator (Linac) was introduced [6, 7], which enabled treatment of deep-seated tumor without exerting excessive damage to overlying skin and tissue to the patient. Since then, the technologies of radiation therapy have proliferated over the last decades and more sophisticated radiation therapy techniques such as three-dimensional conformal radiation therapy (3DCRT) [8-10] and intensity modulated radiation therapy (IMRT) [11, 12] have been developed and practiced in the clinic. However, conventional simulation and portal imaging techniques to verify position of beam delivery limited potentials for delivering accurate and conformal beam while sparing normal tissues of new treatment techniques. To overcome such limitation, many investigators have developed variety of in-room imaging devices to ensure more accurate patient positioning and target localization and to facilitate the full potential of 3DCRT and IMRT. The concept of image guided radiation therapy (IGRT) [13, 14] has been introduced since then.

1.3 Image guided radiation therapy (IGRT)

The term IGRT, is defined as process of radiation treatment which use external imaging devices to identify and correct position setup errors arising from inter-and intra-fractional variation in patient setup and anatomy.[1] To date, it is considered as very promising method of treatment to ensure accurate and precise radiation delivery to the target. In IGRT settings, machines that deliver radiation (e.g. Linac) are equipped with imaging devices to image the tumor immediately during/prior to the treatment. These imaging devices are able to provide accurate information about patient positioning and organ motions, which can be used to correct positioning errors and control organ motion effects during the treatment process. By combining modern radiation therapy technique such as 3DCRT or IMRT, the radiation dose delivery accuracy is significantly improved, leading to a substantial reduction in the volume of irradiated normal tissues.[15] This reduction of the irradiated volume helps reduce the damage caused to the health tissues, allowing us to escalate the dose to the tumor to increase the tumor control probability. Moreover, IGRT increases the amount of data collected throughout the course of the treatment. Over the course of treatment, this information allows the continued assessment and refinement of treatment techniques and adapt to changes such as tumor shrinkage/expansion and changes in shape that may occur over the course of radiation therapy.

1.4 Imaging techniques in IGRT

In IGRT setting, there are many types of imaging technology that can be used to verify patient position. In this section, three most widely used imaging techniques are discussed in brief.

A. Radiological imaging

Radiological imaging is the most basic form of imaging technique where 2D projections or planar images are acquired. This image is then compared with digitally reconstructed radiograph (DRR) of computed tomography (CT) images of the patient acquired for treatment planning and simulation purpose. The size of the object imaged is dependent on the size of the detector and the distance between the detector and imaging object.

B. Fluoroscopic imaging

Fluoroscopic imaging is a continuous series of radiological imaging where patient are continuously imaged with X-rays in real-time during patient during/prior to the treatment. It allows real-time respiratory motion monitoring and verification of patient position using visible anatomical structures or implanted fiducial markers. The information can be used for the management of inter-and intra-fractional tumor motion and motion adaptive treatment in some cases.

C. Tomographic imaging

Volumetric tomography or CT images can be generated through various reconstruction processes by acquiring series of X-ray projections measured at different gantry angles. Currently, it is the most popular imaging technique that is used in the process of IGRT. Position setup error of patient can be accurately measured by

comparing translational and rotational difference of volumetric images with respect to planning CT images. Helical CT as well as cone beam CT (CBCT) system can be used as tomographic imaging device in IGRT. In particular, gantry-mounted CBCT system is the most widely used tomographic imaging device in the clinic.

1.5 Cone beam computed tomography (CBCT) systems in IGRT

Cone beam computed tomography (CBCT) system is a recently developed volumetric imaging device for IGRT where series of kilovoltage (kV) X-ray radiographs are obtained and reconstructed to produce three dimensional (3D) volumetric image of patient to calculate 3D positional offset. [16] The 3D volumetric representation verifies patient position on treatment couch to assist in matching the planned position with the current treatment position. Besides tomographic imaging CBCT system is also capable of providing other imaging techniques such as radiographic imaging and fluoroscopic imaging.

The two most popular CBCT systems manufactured by vendors are On-Board Imager (OBI, Varian Medical Systems, Inc., Palo Alto, CA) and X-ray Volumetric Imager (XVI, Elekta Oncology Systems, Crawley, UK). [Fig. 1-1.] Both, adds two laterally mounted arms, for the X-ray source and flat panel detector on the clinical linear accelerator. This is in addition to the mogavoltage (MV) source and electric portal imager. In OBI, the left arm is an amorphous-silicon (a-Si) flat panel detector while the right arm is kV X-ray source. In XVI, these arms are positioned in opposite way.

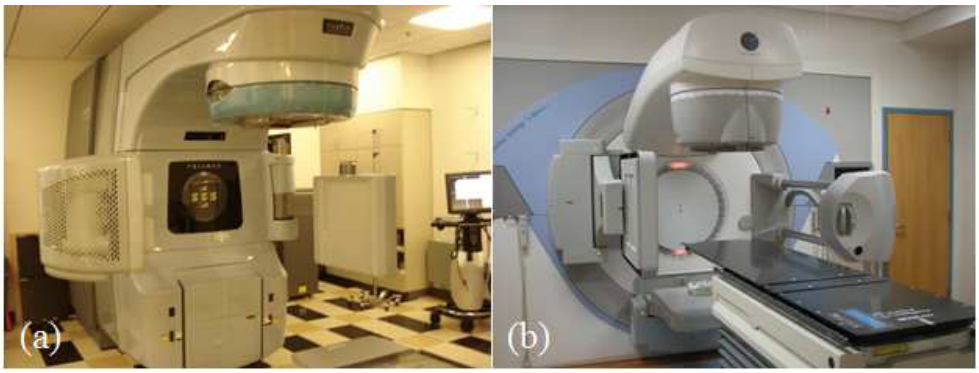

Fig. 1-1. On-Board Imager (OBI, Varian Medical Systems, Inc., Palo Alto, CA) (a) and X-ray Volumetric Imager (XVI, Elekta Oncology Systems, Crawley, UK) (b). Note that position of arms constituting x-ray source and detector are positioned in opposite way.

The two CBCT image acquisition categories are classified according to the dimension of the imaging site. If the imaging site diameter is ≤25 cm, the image falls into the category of *full-fan* scans with *full-fan* beam and full bow-tie filter. If the imaging site diameter is >25 cm, the image is categorized as *half-fan* scans with *half-fan* beam and half bow-tie filter. Two types of filter, the full and half bow-tie filters are added to 1) reduce skin dose, 2) reduce x-ray scatter, 3) improve image quality and 4) reduce the amount of charge trapped in the detector. Subsequently, there are six imaging modes of CBCT, that are named, 1) standard dose head, 2) low dose head, 3) high quality head, 4) pelvis, 5) pelvis spot light and 6) low dose thorax. In each setting, energy, current and scanning time of x-ray are varied to optimize the CBCT image with respect to different sites that are imaged. The reconstructed volume in *full-fan* scan is up to 25 cm diameter in anterior-posterior (AP) and left-right (LR) directions and a maximum of 17 cm long across cranial and caudal (CC) direction. In *half-fan* scans, it is up to 50 cm in diameter across AP and LR directions and maximum of 15 cm across CC direction. Figure 1-2 shows representation of each scan type. In the case of *half-fan* scans, the flat panel detector is shifted laterally by 14.8 to 16 cm depending upon the types of CBCT

machines. In *full-fan* scan mode, the X-ray rotates 200° under the couch to form CBCT image. The X-ray can rotate in one of two possible positions, anti-clockwise or clock-wise. In the mode used for *half-fan* scans, the x-ray rotates 360°, moving in a clockwise direction around the imaging site to form the CBCT image.

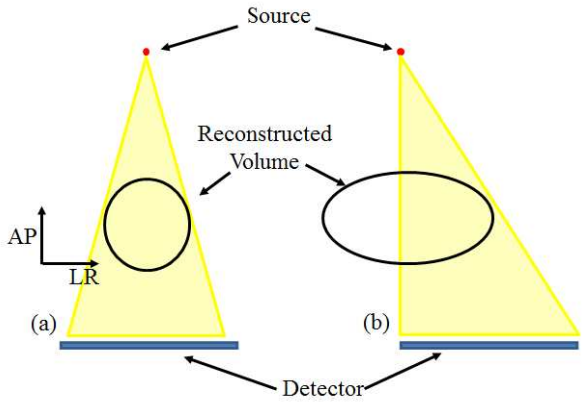

Fig. 1-2. Schematic view of (a) full-fan and (b) half-fan mode CBCT scans.

During the CBCT scan, single exposures are made at certain degree intervals to the patient, providing individual 2D projection images. These images are basically radiographic images of patient measured at different angles. The complete series of images is referred to as the "projection data." In IGRT settings, approximately 364 projections are acquired over 200° in *full-fan* scan mode and 656 projections are acquired over 360° in *half-fan* scan mode to complete "projection data".

1.6 Volumetric imaging modalities using CBCT system

Using the projection data obtained after the preprocessing stage, volumetric image can be reconstructed by synthesizing projection data measured at specified angles. With CBCT system, there are several types of volumetric imaging techniques that can be reconstructed and provide useful information during IGRT procedure. In this section,

four different volumetric imaging modalities that could be reconstructed using projection data acquired from CBCT system are discussed in brief.

A. Three dimensional (3D) CBCT

When all projection data are used to reconstruct single 3D volumetric image, the volumetric image is called 3DCBCT or free breathing 3DCBCT (FB-3DCBCT), which is most popular and widely used method in IGRT. It has prominent role in current radiotherapy settings due to of its wealthy functional role in providing (1) anatomic information, (2) geometric information and (3) CT numbers for possible dose calculation and on-line/off-line re-optimization of plans as well as precise patient positioning.[17, 18]

To reconstruct 3DCBCT, algorithm developed by Feldkamp, Davis and Kress (FDK)[19] is most widely used reconstruction technique. It is an extension of exact 2D reconstruction algorithms for fan-beam projection to the 3D case by properly adapting the weighting factors to the projection data. The FDK algorithm can be divided into three steps: generate weighted projection data where cosine weighting is applied to the preprocessed projections, ramp filter the projection images row-wise, and back-project the filtered projection data into the volume. Once 3DCBCT have been reconstructed, they can be recombined into a single volume for possible IGRT procedure.

B. Digital tomosynthesis (DTS)

Digital tomosynthesis (DTS) is a quasi-3D imaging technique which reconstructs images form a limited angle of cone beam projections typically over $\leq 45°$ scanning angle.[20-22] Figure 1-3 shows the scanning protocol of CBCT system when 3DCBCT and DTS images are acquired. It has advantages over CBCT in terms of lower doses,

short image acquisition times, and less gantry rotation requirements. This modality could be beneficial for imaging organs affected by respiratory motions and for those patient treatments when full gantry rotation is mechanically impossible.

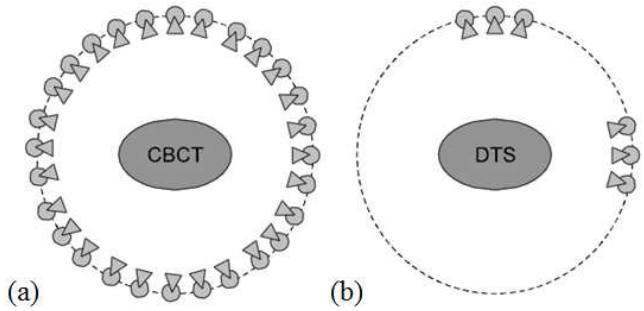

Fig. 1-3. Schematic view of (a) CBCT and (b) DTS scans

C. Four dimensional (4D) CBCT

Image acquisition time of CBCT system is long (≥1 min for thoracic/abdominal sites) due to limited speed of the linear accelerator gantry. Due to such reason, when 3DCBCT is applied to thorax, the image quality can be heavily degraded due to patient respiratory motion. Serious motion-induced artifacts compromise the effectiveness of using CBCT during IGRT. To overcome this problem, four-dimensional (4D) CBCT has been developed to provide respiratory phase-resolved volumetric images.[23, 24] In such an imaging modality, all the X-ray projections are first retrospectively grouped into different respiratory phase bins according to breathing signal tagged on every projection image. A CBCT image for each breathing phase is then reconstructed independently, yielding an image with much less motion-induced artifacts. The capability of 4DCBCT to significantly reduce the motion artifacts and enhance the target localization accuracy has been evaluated, allowing up to 50% reduction in planning target volume (PTV) size.[25]

D. Low-dose CBCT

Because CBCT uses ionizing X-rays to image, there is a legitimate concern about hazardous radiation exposure to patients. Due to this, excessive use of imaging should be prohibited and the benefits-vs-harm ratio should be carefully weighed and debated for each treatment, especially for pediatric patients. Currently, many investigators are developing various low-dose imaging protocol and algorithms using CBCT system.

Recently the concept of low-dose CBCT has been introduced. [26-28] In low-dose CBCT settings, there are rather straight forward ways to reduce the imaging dose by either 1) minimize the number of x-ray projection, 2) reduce the current setting in the x-ray tube, and/or 3) reduce the total exposure time (ms). With the current-standard FDK reconstruction algorithm, however, reducing the projections will cause aliasing artifacts the severity of which depends inversely on the number of projections, and if the current or exposure is reduced, the noise in the image would increase. Both of these properties of the FDK are extremely undesirable, especially if the images are used for guiding precision radiation therapy for cancer eradication. Therefore, improved reconstruction algorithm is needed to handle such problem.

Introduction of compressed sensing (CS) theory [29, 30] has been proved that signals which are noisy and sparsely sampled can be reconstructed with high image quality.[31] Especially, the total variation (TV) method has been particularly useful in CT reconstruction by exploiting the minimal variation in x-ray attenuation across body tissues.[32-37] This theory has become promising solution to low-dose fan-beam CT as well as CBCT reconstruction problem. Consequently, such improved reconstruction

algorithm can potentially reduce the typical CBCT imaging dose by up to an order of magnitude for the use not only in IGRT purpose but also in diagnostic imaging.

1.7 Motivation of thesis

While CBCT for patient positioning has been shown to reduce setup error, there are still a number of issues that needs to be investigated in order to realize the full potential of an on-board imaging device. In theory, the CBCT system can be used to perform sophisticated radiation therapy techniques include adaptive radiation therapy, on-line re-planning, real-time dose estimation and real-time patient monitoring. These methods are all limited by 1) performance of CBCT imagers, 2) the quality of on-board CBCT images with respect to patient dose and respiratory motion, 3) the speed in which CBCT can be reconstructed and 4) the variation of inter-and intra-fractional tumor motion during the treatment. Therefore, it is important to investigate each limitation in separate or in combination, and provide solutions to improve the utilization of CBCT system during IGRT.

1.8 Specific aims

The specific aims of this dissertation are as follows:

1. Develop a fully automated approach to identify and compensate defective pixels that progressively increases with routine use of X-ray imagers in CBCT system.
2. Investigate on fast low-dose CBCT imaging modalities and prove the feasibility of its use for image guidance in radiation therapy.
   2.1. Develop a digital tomosynthesis (DTS) reconstruction framework using limited angle projections data that can be reconstructed almost in real time.

2.2. Develop a novel low-dose CBCT reconstruction algorithm that handles low-dose CBCT reconstruction problem in a highly efficient manner, with speed acceptable for routine use in the clinic.

3. Investigate on respiratory correlated volumetric imaging framework and prove the feasibility of its use for respiratory motion monitoring and image guidance in radiation therapy.

   3.1. Develop a method to reconstruct four dimensional (4D) CBCT and DTS reconstruction using the respiratory signal extracted from inserted fiducial markers in the liver.

   3.2. Develop a novel 4DCBCT reconstruction framework that allows reconstruction of high quality and high phase resolution images.

4. Investigate on inter-and intra-fractional liver motion variation during image guided stereotactic body radiation therapy (SBRT) and discuss its clinical outcomes.

1.9 Dissertation organization

The remainder of dissertation is organized as follows.

Chapter 2 presents a method of identifying defective pixels in X-ray imagers based on wavelet analysis. This includes introduction of wavelet transform, procedure for generating defective pixel map based on wavelet analysis in x-ray imager, how to correct defective pixels and experimental results.

Chapter 3 introduces ultra-fast reconstruction technique for DTS imaging using standard general-purpose graphics processing unit (GPGPU) programming interface. This includes Feldkamp, Davis, and Kress (FDK) based DTS reconstruction algorithm, DTS

image acquisition procedures, GPGPU programming fundamentals and performance analysis of the method.

Chapter 4 proposes novel efficient low-dose CBCT reconstruction algorithm based on gradient projection Barzilai-Borwein (GP-BB) formulation that handles low-dose CBCT reconstruction problem in a highly efficient manner. This includes introduction of low-dose CBCT reconstruction problem using compressed sensing (CS) framework, mathematical formulation of GP-BB algorithm and its implementation on GPGPU programming interface and performance evaluation with other published algorithms.

Chapter 5 presents a method to reconstruct 4D CBCT and DTS reconstruction using the respiratory signal extracted from inserted fiducial markers in the liver. This includes detailed explanation on extraction of fiducial marker positions from cone-beam projection data, generation of breath-induced marker motion signal, validation of the marker extraction algorithm, projection sorting process and results with lung SBRT patients.

Chapter 6 proposes novel 4DCBCT reconstruction algorithm framework called motion-map constrained image reconstruction (MCIR) that allows reconstruction of high quality and high phase resolution 4DCBCT images with no more than the imaging dose as well as projections used in standard CBCT scan. This includes detailed illustration of MCIR algorithm, how to create motion-map of patient, algorithm implementation and performance comparison with other published algorithms using both numerical simulation and patient data.

Chapter 7 presents investigation of breathing induced liver motion during CBCT guided SBRT. This includes the information of patient that we have analyzed in this study, modified marker extraction algorithm of fiducial markers and 3D position tracking algorithm of extracted markers. As a result, we discuss accuracy of marker tracking algorithm, liver motion types and inter-and intra-fractional liver motion variability in detail.

Chapter 8 summarizes the contribution of this work and discusses future research directions.

.

Chapter 2 Identifying defective pixels in X-ray imager using wavelet analysis

2.1 Introduction and background

In recent years, mature electronics and manufacturing methods have led to many approaches for the design and construction of digital detectors for X-ray imaging.[38] Although various configurations of detectors are available, most detectors are mainly composed of two components: X-ray converters, such as scintillators (to provide "indirect" detection of X rays by converting the detected X-ray energy into optical photons) or photoconductors (to provide "direct" detection of X rays by converting the detected X-ray energy into electron-hole pairs), and readout pixel arrays.[39, 40] As an optical-photon readout pixel array, charge-coupled devices (CCDs) have been used for a long time because of their high-quality, low-noise imaging performance.[41] Complementary metal-oxide-semiconductor (CMOS) technologies with their recent advances have become an alternative to CCDs, offering a great cost advantage and high physical performance.[42] Presently, flat-panel imagers based on arrays of hydrogenated amorphous silicon (*a*-Si:H) thin-film transistors in combination with either *a*-Si:H photodiodes (for indirect detection of X rays) or storage capacitors (for direct detection of X rays) are central for digital radiography, especially for cone beam computed tomography (CBCT) imaging applications.[40, 43] All of these x-ray imaging detectors utilize pixel formats; hence they provide the intrinsic two-dimensional (2D) imaging capability.

These pixel array detectors are typically fabricated by the semiconductor manufacturing process. During fabrication, the non-uniform fabrication conditions over the areas of the pixel array, for example, the difference in doping concentrations in individual pixel elements, are unavoidable, and these conditions worsen as the detector size increases.[44] Unpredictable local defects can also occur in individual pixels or partial or complete lines.[45] These defective pixels which are defined as the pixels whose signal levels are abnormal from their neighbors, however, are normally accepted to a certain extent in commercial detectors. It is noted that local imperfections in the X-ray converters, such as scintillators and photoconductors, may also be observed as defective pixels in X-ray images.

Basically these defects are considered as fixed-pattern noise (FPN), which degrades the image quality. Image information is lost in radiography from individual pixels or from partial or complete lines [46], and severe streak and ring artifacts arise in CBCT.[47] Therefore, clinical or industrial detectors have to recognize defective pixels (including line defects) and correct them to ensure optimal detector efficiency and image accuracy. Software processing is usually employed for correction. Above all, the exact and reliable identification of defective pixel locations is primary. However, the defective pixels in a detector may not be stationary in time and space.[46] Routine use of detectors and thus the accumulated radiation damage progressively increase the density of defective pixels.[46, 48] Therefore, the frequent evaluation of defective pixels is the only way to use a detector reliably.[48]

In general, defective pixels are identified with dark (in the absence of X rays) and white (under X-ray irradiation with no object) images. The dark and white images are

also referred to as the offset and flat-field images, respectively. When there is no signal variation over large physical areas of a detector, the simple thresholding method with the global mean and standard deviation of the pixel values may be used to recognize defective pixels because defective pixels usually exhibit intensity values abnormally outside the mean value.

However, most detectors show unwanted, large-scale signal variations over areas, which worsen through the working lifetime of the detectors. Signal variation in the dark and white images is most likely caused by the readout amplifiers connected to the columns of the detector panel. Because the readout amplifiers are usually CMOS circuits, they probably exhibit small gain and offset variations, both column-to-column and across each amplifier chip. The exact nature of the non-uniformity depends on the particular device, but it is typically caused by parasitic capacitances and resistances that can vary as a function of how far a particular column is away from the power supply or the output amplifier. For example, if a column amplifier is connected to the output amplifier by a metal trace, the resistance of that trace will be proportional to its length. On a large device, this dependence can be significant and can affect the transfer gain for the signal coming from the column amplifier. Obviously, a column that is close to the output will have less parasitic resistance than one that is far away. It is noted that the variations in thickness of the X-ray converters can also give rise to variable intensity output in X-ray images.

X-ray equipment can also cause flaws and field variations, such as the heel effect, which is an intensity falloff on the anode side of the X-ray tube in the X-ray projection

image, and which usually contributes as large-scale non-uniformities or low-spatial-frequency components in the Fourier domain of images.

These field variations can be dramatically improved by subtracting an offset (dark) image from the image to be corrected, and then dividing it pixel-to-pixel by an offset-corrected flat-field (white) image.[49] This gain-offset or flat-field calibration is a typical procedure in digital radiography. The flat-field calibration requires many dark and white images to reduce the statistical uncertainties in the pixel values during arithmetic operations. Considering the amount of potential drift of the detector response, the flat-field calibration should be frequently performed. It should be noted that only calibration with updated dark and white images can provide adequate images.[48] Moreover, the polyenergetic X-ray spectrum basically makes flat-field calibration incomplete because the pixel response is dependent on the energy and each pixel response in the image with an object is different with that in the offset-corrected flat-field image due to the beam-hardening effect.[50]

In this study, a simple method of identifying defective pixels based on wavelet analysis is presented. The proposed method is motivated from the fact that the response of defective pixels is impulsive and the wavelet transform can decompose discontinuities and sharp spikes in functions. Therefore, the method is immune to the influence of a global intensity variation, so it does not require flat-field-corrected images with many measurements, but may require a single pair of dark and white images.

2.2 Wavelet analysis for defective pixel detection

Wavelet Defective pixels usually exhibit singular responses, unlike normal pixels in a detector. Therefore, sorting out these impulsive responses from global signal variations is the key in the identification of defective pixels. For this procedure, wavelet analysis is employed because the low-frequency components in an image can be easily identified and isolated by wavelet transformation. Conversely, wavelet transforms well represent functions that have discontinuous and sharp peaks. Moreover, wavelet transforms can accurately deconstruct and reconstruct finite, non-periodic and/or non-stationary signals.

Wavelet transform is a linear combination of atomic decomposition, known as wavelets, especially for non-stationary functions.[51] Functions with discontinuities and functions with sharp spikes usually take much fewer wavelet basis functions than sine-cosine basis functions (e.g. Fourier transforms) to achieve a comparable approximation. Since first introduced in the early 1980s, the wavelet transform has become an important technique in signal or image processing, such as data compression, noise suppression, feature extraction, *etc*.[52]

2D image function $f(x, y)$ of $M \times N$ pixels in size can be expressed as [51]

$$f(x,y) = \frac{1}{\sqrt{MN}} \sum_m \sum_n W_\varphi(j_0, m, n) \varphi_{j_0,m,n}(x,y) + \frac{1}{\sqrt{MN}} \sum_{k=H,V,D} \sum_{j=j_0}^{\infty} \sum_m \sum_n W_\psi^k(j,m,n) \psi_{j,m,n}^k(x,y) \quad (2.1)$$

where j_0 is an arbitrary starting scale and the $W_\varphi(j_0, m, n)$ coefficients define an approximation of $f(x, y)$ at scale j_0. The $W_\psi^k(j, m, n)$ coefficients add horizontal, vertical, and diagonal details for scales $j \geq j_0$ and the superscript k denotes the direction; H, V, and

D represent horizontal, vertical, and diagonal directions, respectively. *m* and *n* designate the sizes of the sub-images and depend on the applied scales. φ and ψ are basis functions, and they are called scaling and wavelet functions, respectively. If we can select the scaling coefficients of an image and modify them, i.e. replace them by zeros, we can obtain an image $\tilde{f}(x, y)$ without global signal variations.

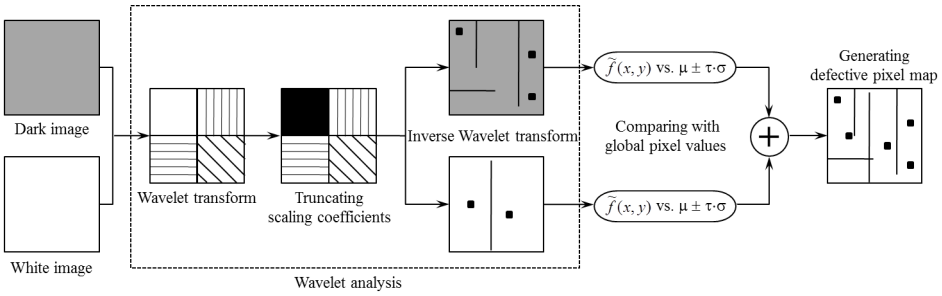

Fig. 2-1. A sketch illustrating the procedure for generating a defective pixel map based on wavelet analysis. Each of the dark and white images is changed into a multi-scale sub-image by wavelet transformations. Among four sub-images, the one describing scaling coefficients, which contains low-frequency band characteristics, is truncated and padded with zeros. The modified image is then turned back by inverse transformation, and it only contains sharp speckles. The abnormal singular signal distribution is checked by comparing it with the local pixel mean and its standard deviation, and finally identified as defective pixels.

The identification method of defective pixels including line defects is schematically illustrated in Fig. 2-1. The wavelet transform is applied to a dark image. The transformed image is then represented as four sub-images. In order to suppress or remove the large-scale signal variations, the sub-image represented by scaling coefficients is truncated. In other words, the pixel values consisting of the sub-image are replaced by zeros. And then, the inverse wavelet transform is applied. The reconstructed image is now a filtered image of low-spatial-frequency components and it clearly shows singularities, such as spikes and discontinuities in the pixel values. We used the Haar function as a wavelet.[51] For ensuring defective pixels, the surrounding pixel values were checked again with the local pixel mean μ, its standard deviation σ, and threshold

level τ (viz. $\mu \pm \tau \cdot \sigma$). This thresholding procedure may suppress misleads of temporal random pixel responses. The pixel locations of the defective pixels detected are mapped to a template. The defective pixel map is completed after repeated procedures on a white image.

In this study, with the determined defective pixel map, digital radiography was corrected by simple adaptive median filtering. The mask size of the median filter was 5 × 5 pixels.

In order to demonstrate the proposed method to identify defective pixels in digital radiography, we implemented the method to an X-ray imaging detector. The detector was composed of photodiode arrays and overlying luminescent phosphor. The phosphor (Min-R^{TM}, Carestream Health, Inc., USA) is mainly made of a terbium-doped gadolinium oxysulfide (Gd_2O_2S:Tb) and it converts into optical photons, whose number is proportional to the absorbed energy of X-rays. The photodiode array made by CMOS process (RadEye^{TM}, Rad-icon Imaging Corp., USA) has a format of 512 × 1024 pixels with a pixel pitch of 48 μm.[53] Since only one narrow side of the CMOS photodiode array incorporates the readout electronics, two CMOS photodiode arrays were tiled side-by-side, and therefore, the actual format was 1024 × 1024 pixels and the field-of-view (FOV) was about 50 × 50 mm^2. X-ray irradiation was performed with a small X-ray tube employing a tungsten target (Series 5000 Apogee, Oxford Instruments, USA). The operation conditions were a target voltage of 45 kV and cathode current of 1.0 mA. For sample images, humanoid hand phantom images were acquired. Due to the FOV of the detector, a part of phantom was imaged.

The detector has been used in our laboratory for a long time (more than three years). Since an FPN (including "ghosts" of high contrast objects) is linearly emphasized to the absorbed dose, the detector shows scabbed dark and white images. Therefore, finding defective pixels from the backgrounds was challenging.

2.3 Results

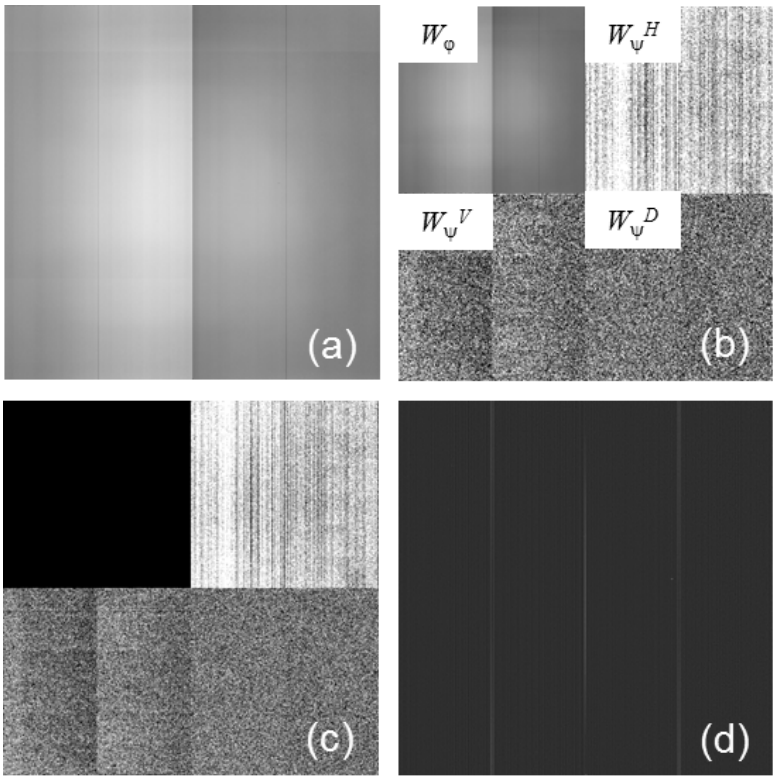

Fig. 2-2. Visual illustration of wavelet analysis to identify defective pixels. (a) A dark image obtained from the CMOS detector. (b) Representation of one-scale decomposition by wavelet transform. (c) One-scale decomposition with selected coefficients deleted. (d) Reconstructed image by inverse wavelet transform.

Wavelet analysis of a dark image obtained from the CMOS detector operated at an integration time of 550 ms is visually illustrated in Fig. 2-2. As shown in Fig. 2-2(a), the 2D display of the dark image shows non-uniform distribution of pixel dark currents and distinct, different responses of the two photodiode arrays. Fig. 2-2(b) represents the

decomposed sub-images by one-scale wavelet transform. Fig. 2-2(d) shows the reconstructed image by the inverse wavelet transform after truncation of the scaling coefficients, as shown in the second quadrant of Fig. 2-2(c). In this image, the global signal variations are removed and only singularities are shown. The dark images before and after wavelet analysis can be more apparently demonstrated by a three-dimensional (3D) display, as shown in Fig. 2-3(a) and (c), respectively. Fig. 2-3(b) is a 3D plot of the white image. The large pits of the central region in the dark and white images are the ghosting resulting from the persistent local irradiation of X-rays during the usage of the detector.

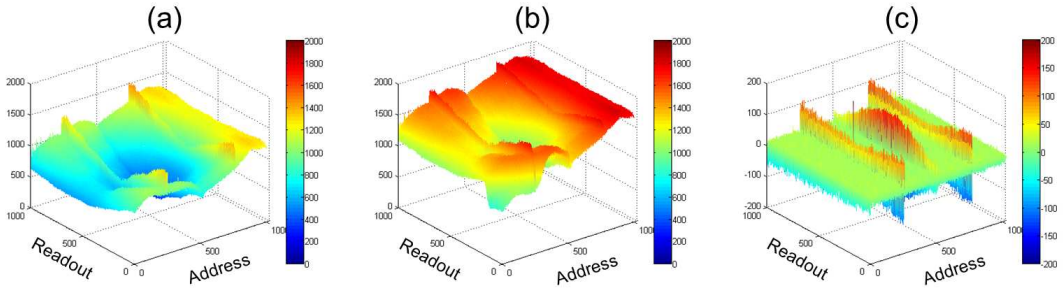

Fig. 2-3. 3D displays of detector signals before and after wavelet transformation. (a) and (b) show signal distributions of the dark and white images, respectively. (c) is the dark image after wavelet analysis.

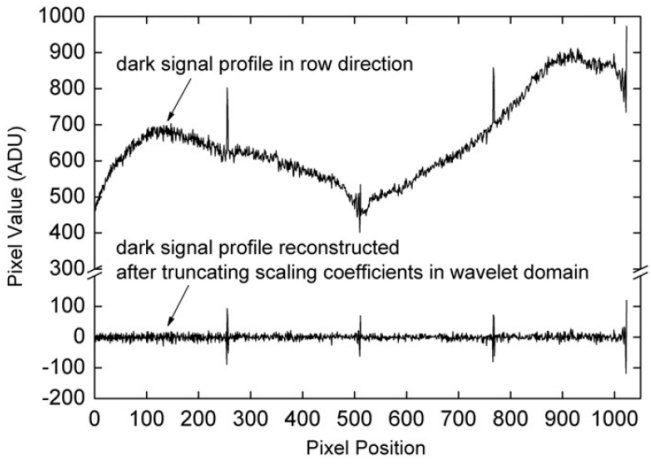

Fig. 2-4. Comparative signal profiles before and after wavelet analysis.

One-dimensional profiles extracted from 2D images in the row (or address) direction before and after wavelet analysis are compared in Fig. 2-4. Truncation of the scaling coefficients in wavelet domain effectively removes the low-spatial-frequency components in an image; hence, singularities are easily identified.

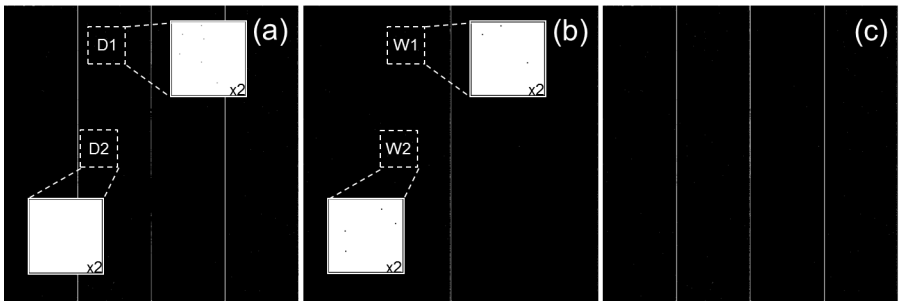

Fig. 2-5. Templates mapping defective-pixel locations. (a) and (b) are the defective pixel maps obtained from the dark and white images, respectively. (c) is the complete defective pixel map by combining (a) and (b). Insets are the enlarged images, displayed in negative, for the regions indicated by the dotted boxes.

Fig. 2-5 shows defective pixel maps generated by wavelet analysis. Fig. 2-5(a) and (b) are the maps for the dark and white images, respectively. The map from the dark image has three defective lines while that from the white image has one defective line. Some of defective lines are composed of more than a single line. The total defective pixel map considering both the dark and white images are shown in Fig. 2-5(c). In order to observe the behavior of pixel defects, arbitrarily selected regions were investigated. For easier visualization, the regions are displayed by negative transformation and the display is enlarged by a factor 2. Regions *D*1 and *W*1 are the same regions of the maps of the dark and white images, respectively. Regions *D*2 and *W*2 also reflect the same regions in the maps of the dark and white images. Comparing *D*1 and *W*1, some of defective pixels share the same position both in the dark or white maps, but some do not because of the small abnormality in the signal intensity in the white image compared with the global mean pixel value. As shown in the selected regions of *D*2 and *W*2, some defective pixels

are very sensitive to X-ray exposure. It should be noted that the defective pixels are clustered in the map obtained from the white image, probably due to the signal leakage of the defective pixel into its neighborhood.

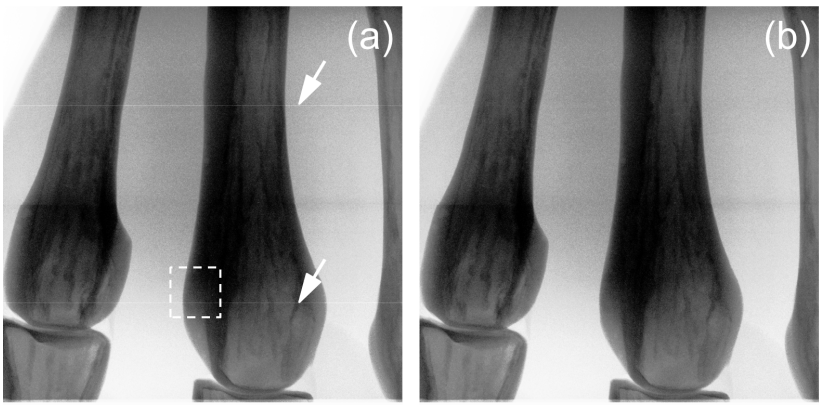

Fig. 2-6. An example of defective-pixel correction in digital radiography with the defective pixel map. (a) An image of hand phantom obtained from the CMOS detector. (b) Defect-corrected image by adaptive median filtering operation based on the defective pixel map.

The defective pixel map that was obtained was used to correct defective pixels on a hand phantom image, as shown in Fig. 2-6. Simple adaptive filtering worked well, as shown in Fig. 2-6(b). The line defects indicated as arrows in Fig. 2-6(a) are not shown in Fig. 2-6(b). The region indicated as a dotted box in Fig. 2-6(a) has been investigated in detail, as shown in Fig. 2-7. The arrows in Fig. 2-7(a) indicate two pixel defects and one line defect. As shown in Fig. 2-7(b), two pixel defects are clearly corrected but a faint line seam is still shown. Fig. 2-7(c) is a difference image between Fig. 2-7(a) and (b).

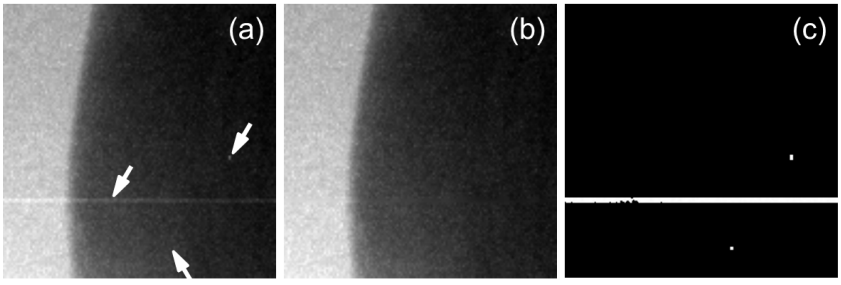

Fig. 2-7. Enlarged images indicated by the dotted box in Fig. 2-6(a). (a) and (b) are the images before and after the defective-pixel correction, respectively. (c) describes the difference between (a) and (b).

2.4 Discussion and conclusion

In the wavelet transforms, we used the Haar function as a wavelet. The Haar function provides an operation similar to the *derivative* when finding directional wavelet coefficients. Therefore, there might be artifacts around the reconstructed singularities. As shown in Fig. 4, the profile after wavelet transformations shows sharp spikes adjacent to the original singular responses in negative values. Threshold checking with the local mean value and standard deviation for the neighboring pixel values would prevent the negative spikes from defective pixels as performed in this study. Other filter functions, which would not cause this kind artifact, as a wavelet are alternatives. Although we partly employed the threshold method, the computational cost is cheap because thresholding is applied to limited regions around singularities identified by wavelet analysis.

There are several techniques for defective pixel correction with various tradeoffs between the effectiveness and complexity of computations. The simplest method is to apply a median filter as demonstrated in this study. A similar method is mean filtering. While median filtering replaces the defective pixel with the median around pixel values, mean filtering uses the average value of the surrounding pixel values. Although mean filtering is more time-consuming than median filtering, the image quality is better because it uses information from more than just one of the neighboring pixels. In mean filtering, however, the neighboring pixels need to be good pixels.

Unlike isolated defective pixels in space, clustered pixel defects are serious because of the lack of information for correction. T. Aach and V. Metzler [54] introduced an iterative deconvolution method in the frequency domain. They modeled a distorted radiography due to defective pixels by a multiplication of the undistorted radiography by

the defective pixel map. Then, defect interpolation would correspond to the deconvolution of the corresponding spectra. Although this method has high computational complexity, it is particularly suited to large defective areas. With respect to line defect interpolation, various interpolation techniques are available.[55]

Defective pixels are an inevitable result of the manufacturing process for large area semiconductor digital detectors. For the reliable use of detectors over their working lifetimes, a complete list of the locations of all the defective pixels (or a defective pixel map) should be prepared, and the defective pixel map needs to be updated by frequent monitoring. In this study, we introduced the generation of a defective pixel map based on wavelet analysis and applied the map to the digital radiography that is used for CBCT imaging. The method does not require gain-and-offset corrected images. Therefore, it is appropriate to periodic monitoring of CBCT imaging systems.

2.5 Acknowledgements

The text of Chapter 2, in part or in full, is a reprint of the material as it appears in the following publication:

Park JC, Lee HK, Song WY, Achterkirchen TG, Kim HK. Defective pixel map creation based on wavelet analysis in digital radiography detectors. Nuclear Instruments and Methethods in Physics Research A. 2011;634:101-5.

The dissertation author was the primary researcher and the co-authors listed in this publication directed and supervised the research which forms the basis for this chapter.

Chapter 3 Fast digital tomosynthesis (DTS) reconstruction using general-purpose graphical processing unit (GPU).

3.1 Introduction

In recent years, the introduction of cone-beam computed tomography (CBCT) system in treatment room settings has enabled implementation of various image guidance and adaptive radiotherapy techniques.[14, 17, 56-58] This was possible due to the wealth of information that can be obtained from three-dimensional (3D) CBCT images obtained immediately prior to treatment, including anatomic information for setup [25, 59-61], and CT numbers for dose calculation [62-64] and on-line/off-line re-optimization of plans. [65-68] All in all, there is minimal doubt that CBCT has prominent role in current and future radiotherapy practices.

In certain clinical settings, however, CBCT may not be the optimal method for localization because the patient dose is significant [69-71] and acquisition times are long. [72-74] In addition, the images may be impossible to acquire for large off-axis patient set-ups, large patients, and/or bulky immobilization devices due to mechanical collisions. This can become quite unacceptable for clinical sites with large inter-fraction variations.

As an alternative to full 3D CBCT imaging, there is growing interest to adopt digital tomosynthesis (DTS) for use in image-guided radiation therapy (IGRT) applications.[20-22, 75] This technique takes advantage of the CBCT scanning geometry and results in pseudo 3D images stacked around the imaging isocenter that are

reconstructed from projections data scanned at limited projection angles (typically 40-60°). The reconstructed images generally contain enough anatomic information for IGRT applications in clinic [76-80], but due to its limited scan angles, the resolutions are limited in directions that are not orthogonal to the scanning geometry [81](i.e., due to pseudo 3D volume).

Current interest in DTS is due to its many advantages over full 3D CBCT, including 1) patient dose reduction (> 3 times) [81, 82], 2) scan time reduction (> 4 times) for faster set-up to beam-on work flow [76, 79, 83-86], 3) faster image reconstruction due to less projections data (> 4 times)[81], and 4) limited scan angle allows more flexibility in scanning geometries and patient set-ups.[79] In addition to these advantages, and despite the reduced image quality and resolution, numerous publications have shown that DTS contains enough image quality and anatomic information for many IGRT applications including head-and-neck [78, 82, 83, 87], lung [82, 88], liver [82, 89-91], prostate [84, 86], and breast [79, 80] radiotherapy. In particular, the faster scan time can be of major benefit for clinical sites (or patients) that demonstrate large intra-fractional motion drifts since the influence of this effect on treatment quality will be minimized.

At current, however, there is no commercial system that allows DTS reconstruction for clinical IGRT applications, although multiple systems are available for 3D CBCT reconstruction. The current commercial 3D CBCT reconstructions can be accomplished in ~10-15 seconds after image acquisition. This is possible because the reconstruction starts as soon as the first X-ray projection is acquired. Therefore, it is anticipated that 3D DTS reconstruction would take < 10 seconds at most if it is to be commercially implemented. However, a faster reconstruction is still desirable if more

sophisticated image processing (such as noise, scatter reduction, etc) and real-time applications [92] are to be realized. To accommodate this need, we have investigated the data-parallelization approach using graphics processing unit (GPU). In fact, there has been increasing number of studies utilizing the computational power of GPU to accelerate classically heavy and "parallel" computational tasks in radiation therapy including image reconstruction, deformable image registration, dose calculation, treatment plan (re-) optimization, and most importantly here, DTS reconstruction. [93-99]

General-purpose GPU (GPGPU) computing with the Compute Unified Device Architecture (CUDA, NVIDIA Corporation, Santa Clara, CA) technology is an innovative combination of computing features that enables programmers to use general C language to assign computational tasks to GPU (or *device*) as *kernels* from CPU (or *host*). Kernels are executed through a predetermined number of parallel *threads*, similar to multi-threaded programming on traditional CPUs, that can perform a large number of similar computations at once (depending on the number of processing cores in GPU card). Therefore, in contrast to multi-core CPUs, where only a few threads execute at each time, CUDA technology can process thousands of threads simultaneously enabling much faster capacity of information flow.

In this study, we present ultra-fast GPU-based DTS reconstruction scheme using the recently developed CUDA programming environment. To the best of our knowledge, Yan *et al*. [99] has been the only group to investigate the use of GPU hardware for accelerating DTS reconstruction for RT applications. They used OpenGL application programming interface (API) to program and assign computational tasks to the graphics hardware (GPU model not stated, however). With this approach, they were able to

achieve ~40 seconds to reconstruct 255 slices. [99] In this paper, we will present much faster, non-graphics programming strategy using CUDA, encoded with the general C programming, which takes at maximum 2.5 seconds to complete 256 slices, virtually eliminating the time allocation for reconstruction.

3.2 FDK-based DTS reconstruction

There are many reconstruction algorithms for DTS imaging.[22, 75] For cone-beam geometry, however, the well-known FDK algorithm proposed by Feldkamp, Davis, and Kress [19], is the algorithm of choice due to its simplicity and efficiency. Briefly, in FDK, the anatomical pixel information at (*x,z*) plane, at an arbitrary depth *y*, denoted by $f(x, z/y)$, can be calculated from the following equation [19]:

$$f(x,z/y)=\frac{1}{N_o}\int_{\beta=\min\beta}^{\max\beta}\frac{d^2}{(d\quad s)^2}\int_{-\infty}^{+\infty}\frac{d}{\sqrt{d^2+p^2+\xi^2}}\times R(\beta,p,\xi)h(\frac{d\ \ t}{d\quad s}\quad p)W(p)dpd\beta \qquad (3.1)$$

where N_o refers to the total number of projections, *ß* refers to the angle of each projection, *d* refers to source-to-isocenter distance, *s* refers to voxel-to-detector distance, *p* and ξ are the detector axes perpendicular and parallel to the axis of rotation, respectively, $R(\beta, p, \xi)$ corresponds to cone beam projection data, $h(\cdot)$ refers to convolution filter, and $W(p)$ refers to "half-fan" weighting function for stitching two opposite projections into a single large one (used in “half-fan” mode only) [100]. Figure 3-1 illustrates the reconstruction geometry. From this equation, it is clear that FDK algorithm is composed of two major calculation-intense steps, including 1) integral term $\int_{-\infty}^{+\infty}\ldots dp$ corresponds to the *preprocessing* stage that performs convolution filtering of all projections data, and 2)

integral term $\int_{\beta=\min\beta}^{\max\beta} \ldots d\beta$ corresponds to the *back projection* of the preprocessed projections data, from all angles of measurement, to build the final 3D DTS image volume. It is this *back projection* step that requires the largest computation time, and as shown in this work, this is where GPU gains significant speed-up compared with CPU-based calculations.

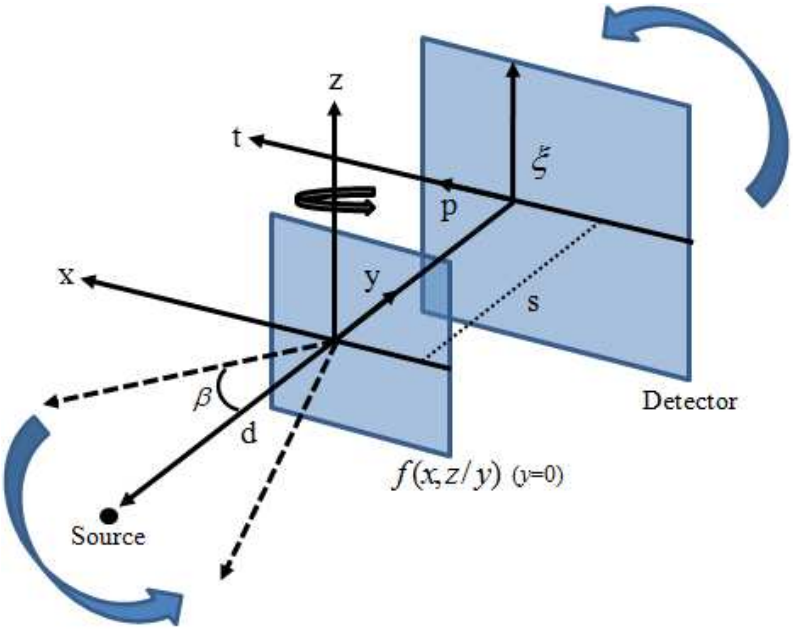

Fig. 3-1. The cone-beam-based DTS reconstruction geometry.

3.3 Imaging device and DTS image acquisition

The patient CBCT data evaluated in this study were acquired using the On-Board Imager (OBI v1.4) integrated with the Varian Trilogy unit (Varian Medical Systems, Palo Alto, CA). This system consists of a kV X-ray source (KVS) with a flat panel *a*Si detector (KVD) mounted orthogonal to the gantry axis using a robotic arm (Exact™), sharing approximately the same rotation center with the treatment unit. The flat panel detector consists of 1024×768 pixels with pixel size of 0.388×0.388 mm. The source-to-

detector distance (SID) is approximately 150 cm, with maximum gantry rotation speed of 6 degrees-per-second.

There are two main scanning modes with OBI, namely 1) *full-fan,* and 2) *half-fan*. In the *full-fan* mode, the detector is centrally placed on the beam axis during scan resulting in field-of-view (FOV) of 24-cm diameter. In this mode, only ~200-degree scanning is necessary to reconstruct a full 3D CBCT volume. In the *half-fan* mode, the detector is shifted laterally by 14.8 cm to increase the FOV to a maximum of 50-cm diameter (normally set to 45-cm in clinic). Since the detector is shifted during scan, each projection image requires 180-degree opposite image pair to obtain the larger projection image used for reconstruction [100] (see Figure 3-2). Therefore, this mode requires ~360-degree scanning to reconstruct a full 3D CBCT volume.

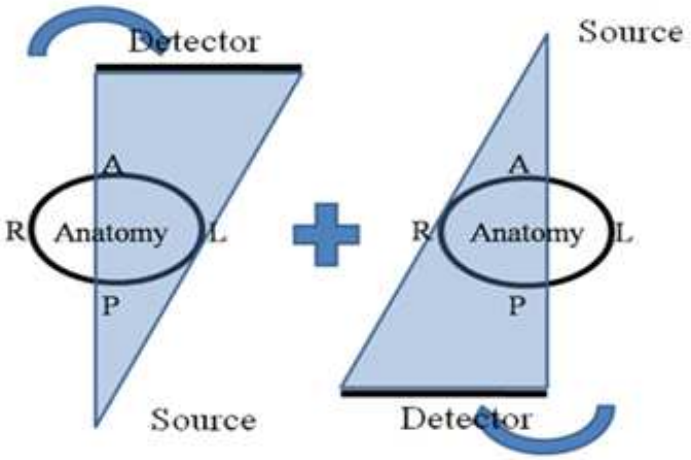

Fig. 3-2. The *half-fan* scanning geometry of the Varian OBI system. The two smaller laterally-shifted projections with 180-degrees apart can be combined to obtain one larger projection to reconstruct a larger FOV images.

Since there is no “DTS” mode available in the current OBI version (v.1.4), the DTS images were reconstructed using subset of projections data extracted from both the *full-fan* and *half-fan* scans obtained in clinic. For the *full-fan* scans, the projections from

157.5°-202.5° (45°-scan) were used to reconstruct coronal DTS slices, whereas for the *half-fan* scans, the projections from both 157.5°-202.5° and 337.5°-22.5° (2×45°-scan) were used to reconstruct larger FOV coronal DTS slices. For this study, we chose 45°-scan angle that contained ~80 projections for the *full-fan* and ~160 projections with 2×45°-scan angle for the *half-fan* mode, each with 1024×768 pixels with 32-bit precision. The reconstruction volume was set to 512×512×(16, 32, 64, 128, or 256) resolution with 1-mm slice thickness, in order to evaluate the reconstruction time dependence on reconstruction volume. In both the CPU and GPU implementations, the "stitching and weighting" of the opposite-angle projections from the *half-fan* scans are performed as part of the *preprocessing* step in the FDK algorithm. Both "stitching" and "weighting" are necessary to merge the opposite half-fan projections and to avoid cupping artifact due to the projections overlap in the middle.[100] Therefore, the algorithms are fully automated and only require uploading of raw projections data, whether acquired in the *full-fan* or *half-fan* mode. It also needs to be stated here that, if clinically implemented, the DTS imaging should ideally be acquired in the *full-fan* mode since the *half-fan* mode is 1) more prone to potential motion artifacts during longer scans, unless larger FOV is absolutely necessary, 2) the physical scan time is longer, and 3) the similar mechanical restraints issues exist as in full CBCT scanning.

3.4 CUDA-enabled GPU programming

In this study, we have used the latest released NVIDIA GTX 295 GPU card (NVIDIA Corporation, Santa Clara, CA) for speeding-up DTS image reconstructions. This model consists of 480 processing cores (2×240 dual chip) with 1,242 MHz

processing clock speed and 1,792 MB memory space, which is more than enough to store a typical DTS volume images (~ 256 MB). In terms of hardware, we used Intel Core™ i7 CPU with 2.68 GHz clock speed, 12.0 GB DDR3 RAM, on a 64-bit Vista OS.

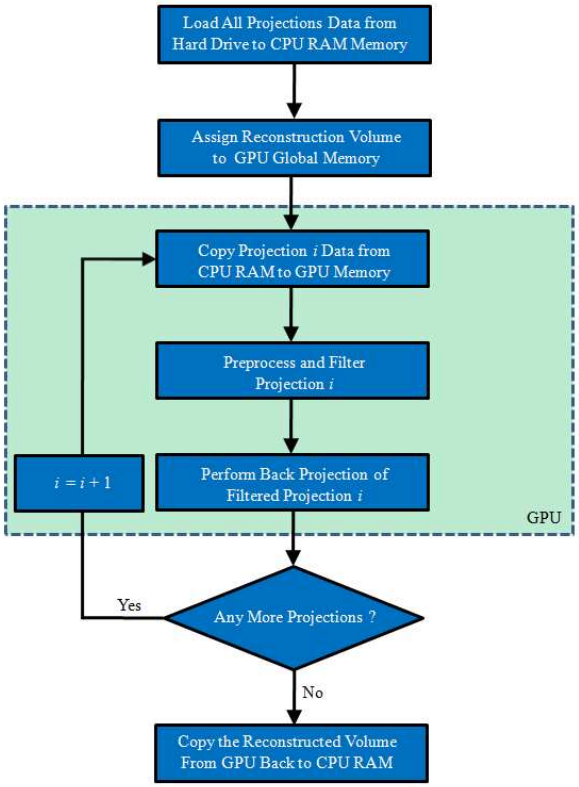

Fig. 3-3. The GPU-based DTS reconstruction work flow.

The general work flow of DTS volume reconstruction is illustrated in Figure 3-3. The program begins by loading all of the X-ray projections data (~3 MB/projection, 1024×768 with 32-bit precision) onto the CPU RAM after image acquisition (~ 240 and 480 MB of RAM needed for *full-fan* and *half-fan* modes, respectively), then each projection image is sent to the GPU for *preprocessing* and *back projection* (shaded in light green) computations, until all projections are used to build the pseudo 3D DTS image volume. This reconstruction volume is stored in the GPU global memory at all

times. For convolution filtering of the *preprocessing* step, we have accelerated the Fourier transform calculations by utilizing the CUFFT (or CUDA FFT) library provided through CUDA. For the *back projection* step, which is the most time consuming part for CPU, we have parallelized the tasks as threads in GPU to gain massive speed-up. The *preprocessing* step, for the GPU-based implementation, includes 1) uploading of the projections data from CPU RAM to GPU memory and 2) the convolution filtering.

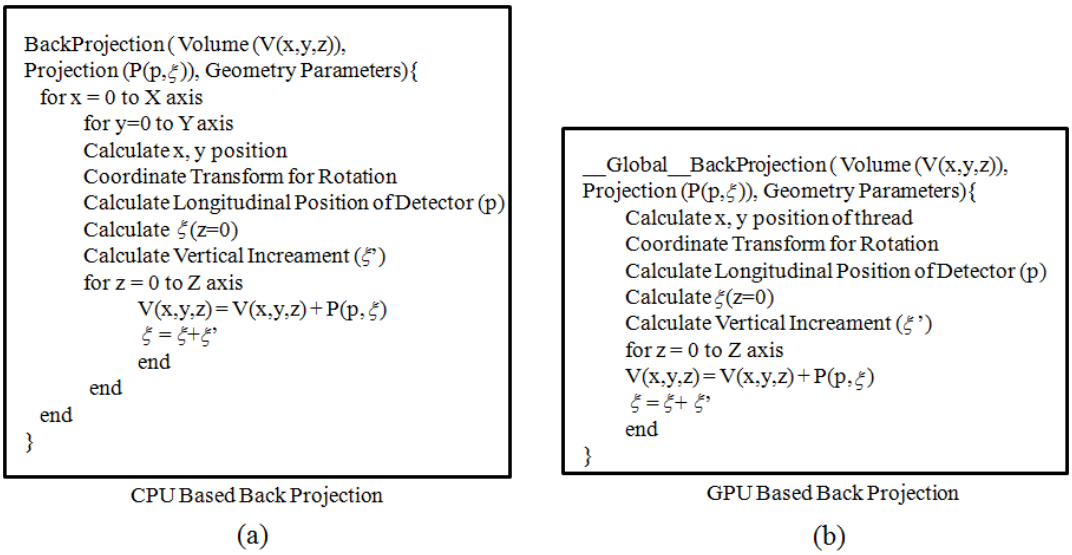

Fig. 3-4. The pseudo code illustrating how (a) the CPU-based and (b) GPU-based DTS reconstructions were programmed.

Figure 3-4 is a pseudo code that illustrates how this was implemented. In short, the back-projection volume reconstruction per 512×number-of-slices (X and Y axis) can be parallelized into a single simultaneous calculation (ie, no loops) using GPU threads, and therefore (512×number-of-slices)×512 volume calculation would be computed as 512 loops (Z axis) of 512×number-of-slices calculations. This means that if number-of-slices = 256, then a single parallel execution of 512×256=131,072 calculations is performed for each loop, for 512 times, to reconstruct the entire image volume.

The reasons that “512×number-of-slices” (×512 loops) calculation are parallelized and not “512×512” (×number-of-slices loops) instead are two folds. 1) For X and Y axis (Figure 1), coordinate transform are function of gantry angles at which projections are taken, and hence, coordinate transform calculation needs to be performed for each pixel in the X-Y plane, whereas Z axis is independent of this, and hence performing Z axis last would minimize the total calculation time. 2) In addition, since “512×number-of-slices” (or X and Y axis) are performed as a single-step massive parallel calculation, increasing the number-of-slices would not increase the calculation time. That is, whether 512×16 or 512×256 volume calculations are chosen, it would still be a single-step massive parallel calculation.

To gain further speed-up, after completing the *preprocessing* of each projections data, before *back projection*, we have re-copied each projections data that was stored in the global memory (not cached, but writable) of GPU to the texture memory (cached, but not writable within each core) of GPU since no further manipulation of the projections data are needed. This way, data-read speed is faster, stable, and most importantly, the interpolation for pixel value calculations on predefined pixel grid size (512×512) is automated by the texture memory hardware during the *back projection* stage. If not, a separate bi-linear interpolation has to be performed for each back projection process, which delays the reconstruction (as is done in CPU-based implementation). This difference in interpolation calculation between the CPU- and GPU-based methods causes slight variation in pixel values reconstructed using each technique as will be shown in Section 3.6. For the CPU-based method, all computational tasks, as illustrated in Figure 3-4, were performed using the CPU hardware described above.

3.5 Patient cases and performance analysis

The performance of the GPU implementation was tested on twenty-five patient cases of various clinical sites (5 lung, 5 liver, 10 prostate, and 5 head-and-neck cases) scanned either with the *full-fan* or *half-fan* vendor-established standard mode on the OBI v.1.4. For lung and liver, the standard "Pelvis" *half-fan* protocol was used. For prostate, both the "Pelvis" *half-fan* and "Pelvis spot light" *full-fan* protocols were used. For head-and-neck cases, all of the head protocols supplied by OBI were used, namely "Low dose head", "Standard dose head", and "High quality head" *full-fan* mode. These various protocols are chosen for evaluation due to their frequent use in clinic for various treatment applications, due to their image quality differences, as well as the volume and site being scanned.

For each clinical case reconstructed using the CPU- and GPU-based methods, the overall times taken as well as each stage of reconstruction were recorded for comparison, using the internal clock measurement function provided by both CPU (clock function in C) and GPU (cut-timer function in CUDA). In addition, the times taken for the reconstruction volume of 512×512×(16, 32, 64, 128, and 256 slices), with 1-mm slice thickness, were recorded.

For image similarity/difference measurements, the difference maps between the two image volumes, the average, and standard deviations in absolute pixel-value differences were computed, along with line profiles. In addition, as part of the comprehensive image comparisons, the contrast-to-noise (CNR) ratio was also computed for both CPU- and GPU-based techniques, using the CatPhan 600 phantom scan (The Phantom Laboratory Inc., Salem, NY). The formula used was:

$$CNR = \frac{2 \times (S_a - S_b)^2}{\sigma_a^3 + \sigma_b^2} \tag{3.2}$$

where S_a and S_b correspond to mean-intensity of regions **a** (inside an insert) and **b** (background), and σ_a and σ_b correspond to standard deviation of regions **a** and **b**.

3.6 Results

A. Image quality comparison

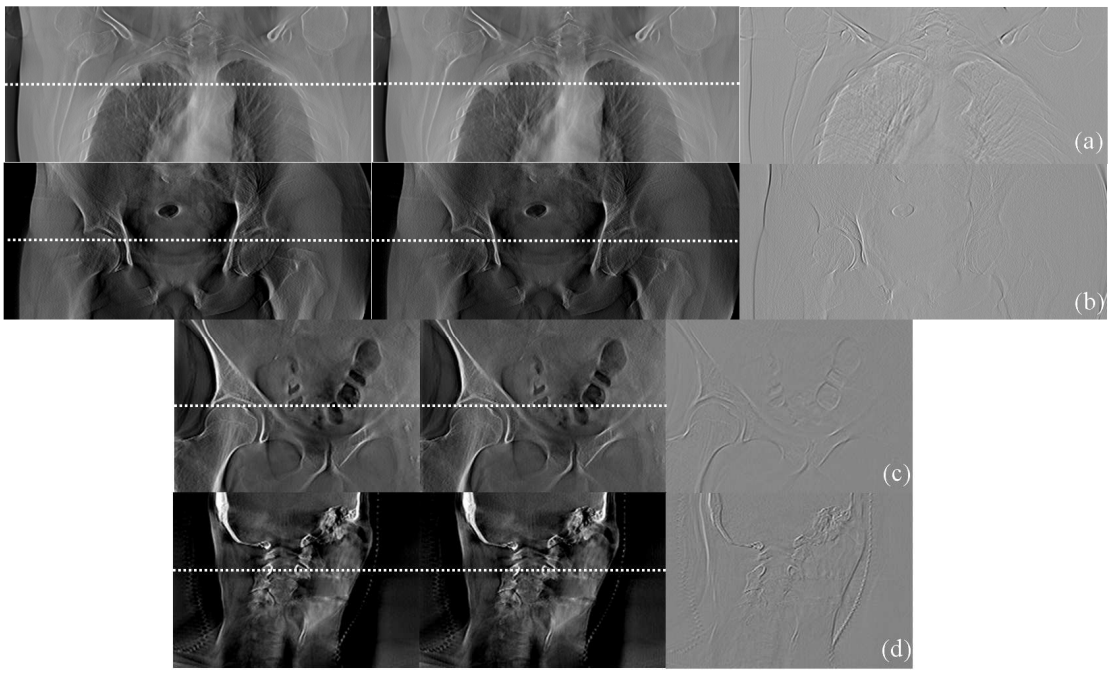

Fig. 3-5. The CPU-based (left), the GPU-based (middle) DTS reconstructions, and the difference map (right) images of (a) lung case scanned with “Pelvis” protocol, (b) prostate case scanned with “Pelvis” protocol, (c) prostate case scanned with “Pelvis spot light” protocol, and (d) head-and-neck case scanned with “Standard dose head” protocol.

Figure 3-5 shows the final reconstructed DTS images using the CPU- and GPU-based implementations, as well as the difference maps, for selected clinical cases. The images shown were reconstructed with 512×512×256 resolution, with 1×1×1mm^3 pixel size. As can be seen, there are virtually no differences between the two types of

implementations on image quality. The minimal difference that is seen is due to the differences in pixel interpolation methods used, as described in Section 3.4.

Table. 3-1. The average absolute difference in pixel values and its standard deviation (SD) calculated using 512×512×256 reconstruction volume between the CPU- and GPU-based implementations, for each clinical case examined.

Patient	Site	Scan Technique	Scan Mode	Avg. Abs. Diff.	SD	Avg. Pixel Value
1	Lung	Pelvis	Half-fan	0.068	0.17	2.77
2	Lung	Pelvis	Half-fan	0.069	0.17	2.28
3	Lung	Pelvis	Half-fan	0.068	0.17	2.32
4	Lung	Pelvis	Half-fan	0.068	0.17	2.59
5	Lung	Pelvis	Half-fan	0.069	0.17	2.74
6	Liver	Pelvis	Half-fan	0.138	0.39	2.61
7	Liver	Pelvis	Half-fan	0.137	0.38	2.52
8	Liver	Pelvis	Half-fan	0.092	0.23	2.27
9	Liver	Pelvis	Half-fan	0.072	0.16	2.81
10	Liver	Pelvis	Half-fan	0.091	0.19	2.92
11	Prostate	Pelvis	Half-fan	0.146	0.41	2.31
12	Prostate	Pelvis	Half-fan	0.148	0.42	2.56
13	Prostate	Pelvis	Half-fan	0.154	0.43	2.72
14	Prostate	Pelvis	Half-fan	0.145	0.43	2.71
15	Prostate	Pelvis	Half-fan	0.098	0.29	2.54
16	Prostate	Pelvis Spot Light	Full-fan	0.045	0.14	2.11
17	Prostate	Pelvis Spot Light	Full-fan	0.045	0.14	2.89
18	Prostate	Pelvis Spot Light	Full-fan	0.032	0.12	2.99
19	Prostate	Pelvis Spot Light	Full-fan	0.039	0.12	2.05
20	Prostate	Pelvis Spot Light	Full-fan	0.037	0.12	1.89
21	Head and Neck	Low Dose Head	Full-fan	0.077	0.30	3.32
22	Head and Neck	Low Dose Head	Full-fan	0.070	0.27	3.69
23	Head and Neck	Standard Dose Head	Full-fan	0.058	0.21	3.75
24	Head and Neck	High Quality Head	Full-fan	0.056	0.24	3.75
25	Head and Neck	High Quality Head	Full-fan	0.052	0.28	3.98

Figure 3-6 shows the selected 2D profile comparisons between the CPU- and GPU-based implementations (from white dashed lines in Figure 3-5). Besides the residual differences due to different interpolation techniques, the profiles are virtually identical. Table 3-1 lists the overall average *absolute* pixel differences and standard deviations (SD) calculated on the 3D volume (512×512×256) for all twenty-five patient cases evaluated. As the table shows, the average *absolute* and SD are negligibly small (<3%) compared to the average pixel values. In addition, the CNR calculations with the CatPhan

phantom images were generally <3% different between the CPU- and GPU-based techniques.

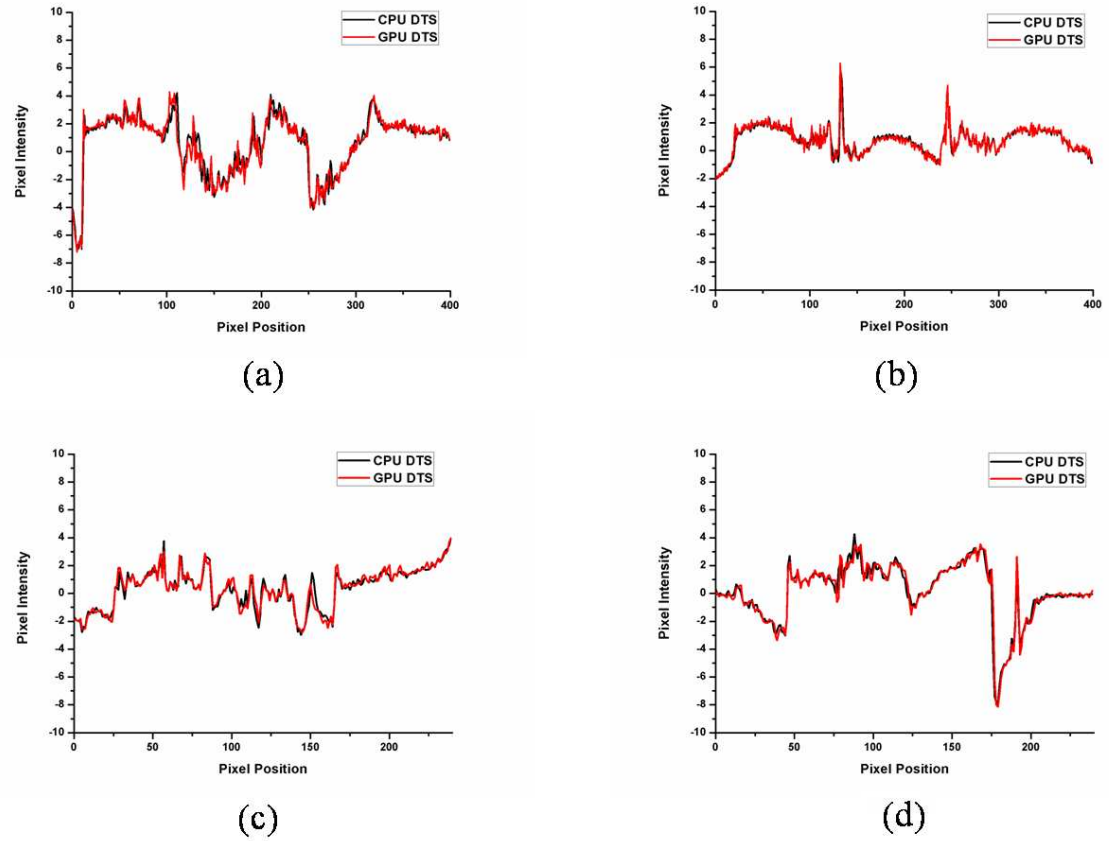

Fig. 3-6. Two-dimensional profiles comparing the CPU- and GPU-based DTS reconstructions, corresponding to the white dashed lines in Figure 5, for (a) lung case scanned with "Pelvis" protocol, (b) prostate case scanned with "Pelvis" protocol, (c) prostate case scanned with "Pelvis spot light" protocol, and (d) head-and-neck case scanned with "Standard dose head" protocol.

B. Speed-up performance of GPU

Table 3-2 lists the break down of average time taken for each step in the overall DTS reconstruction process. FDK step consists of both the *preprocessing* and *back projection* steps. As can be seen, there's significant speed-up in the FDK process with the GPU-based implementation. There is significant speed-up in the *preprocessing* step (> 16 times in the *full-fan*), but the greatest speed-up occurs in the *back projection* step where a

factor of greater than 168 times is seen in the *full-fan* mode. Overall, there is 87.0 and 79.4 times speed-up in the *full-fan* and *half-fan* modes, respectively, for FDK reconstruction. As one can also infer from Table 3-2, on average, the GPU implementation can process > 13 projections-per-second (pps) and > 18 pps for the *full-fan* and *half-fan* modes, respectively. It was also found that time variation from reconstruction to reconstruction is very consistent and less than 20 milli-seconds. This variation comes from multiple sources including 1) clock speed variation, 2) electronic noise in GPU hardware, and 3) variation in image display load (remember, GPU was used to display the monitor while computing reconstruction). However, the time variation of <20ms is negligible compared with the reconstruction time of 1.5-2.5 seconds (<1.5% variation).

Table. 3-2. Break down of the average times taken to perform each stage of the FDK-based DTS reconstruction process. The reconstruction to reconstruction time variation was consistently within 20 milli-seconds or less.

Full-fan DTS (512×512×256)

	Projection loading from disk to RAM	Preprocessing	Back projection	FDK	Total
CPU (Sec)	4.53	10.92	97.81	108.78	113.27
GPU (Sec)	4.53	0.67	0.58	1.25	5.78
Speed-up (×)	1.00	16.3	168.6	87.0	19.6

Half-fan DTS (512×512×256)

	Projection loading from disk to RAM	Preprocessing	Back projection	FDK	Total
CPU (Sec)	6.39	15.95	179.92	195.88	202.27
GPU (Sec)	6.39	1.33	1.14	2.47	8.86
Speed-up (×)	1.00	12.0	157.8	79.4	22.8

Projection loading step copies the projections data stored in the hard disk to the CPU RAM, and as can be seen in the table, this can take few seconds also. However, this

step can be completely eliminated at the clinical implementation stage since one can theoretically upload the projections data onto the CPU RAM as the images are acquired in real-time. Therefore, it can be concluded that, as of this study, DTS reconstruction takes at most 2.5 seconds to reconstruct 512×512×256 image volume, thereby virtually eliminating the time allocation for reconstruction during DTS-based IGRT.

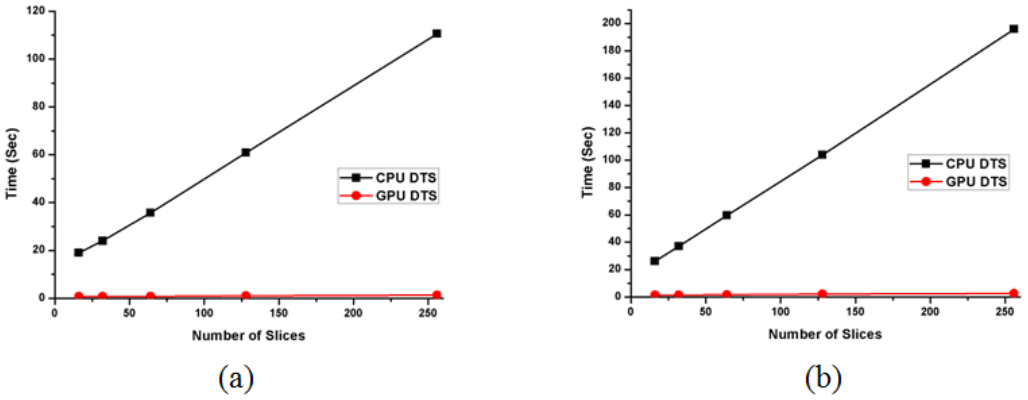

Fig. 3-7. Relationship of times taken for the 3D DTS (512×512×#) volume reconstruction as a function of number of slices for (a) the *full-fan*, and (b) the *half-fan* acquisitions.

Figure 3-7 illustrates the relationship of time taken for DTS volume reconstruction as a function of number of slices, for both the CPU- and GPU-based implementations. On increasing the number of slices from 16 to 256, the time-to-reconstruct increases drastically for the CPU-based implementation where from 19.0 to 110.6 seconds and 26.1 to 195.9 seconds increase were observed for the *full-fan* and *half-fan* modes, respectively. In comparison, only minimal increases are observed for the GPU-based implementation where from 0.73 to 1.27 seconds and 1.42 to 2.47 seconds increase were observed for the *full-fan* and *half-fan* modes, respectively. The increase in times is due mainly to the fact that during the *back projection* step, more pixel scoring is needed as the slices are increased. As was illustrated in Figure 3-4, for the CPU-based

implementation, this means the Y loop is increased and hence the increase in time. For the GPU-based implementation, however, this means that only the number of *block* assignments need to be increased (there is no Y loop) for multi-threaded processing on GPU, therefore the minimal impact on calculation time. The differences in time slopes therefore are due mainly to the multi-threaded and non-parallel-processing approaches in the GPU- and CPU-based calculations, respectively. In addition, increasing the number of slices do not affect the *preprocessing* step, in either case, due to the need for convolution filtering of all projections independently before any back projection takes place for image volume reconstruction.

3.7 Discussion and Conclusion

In this study, we have developed ultra-fast DTS image reconstruction algorithm using CUDA-enabled GPU programming. To the best of our knowledge, CUDA-based DTS programming using OBI projections has never been attempted for RT applications. The times taken for FDK volume reconstruction of 512×512×256 were less than 1.3 and 2.5 seconds for the *full-fan* and *half-fan* modes, respectively. Increasing the number of reconstructed slices had negligible impact on the overall time. In addition, these ultra-fast reconstruction times did not have negative impact on the integrity of the reconstructed images as there were negligible visual and pixel-value discrepancies between the CPU- and GPU-based implementations. With the cost of the latest GPU card being minor (around $500-US) compared to its positive impact on IGRT workflow, as shown in this work and others [93-99], our community should take full advantage of this latest gadget for all heavy computational tasks in RT that are suitable for parallel processing.

As mentioned earlier, Yan *et al*. [99] has been the only group to investigate the speed-up performance of GPU hardware for DTS reconstruction, albeit using the OpenGL API. In their work, they have down-sampled the original projection images (which we didn't do) of size 1024x768 to 512x384 resulting in total reconstruction time of ~40 seconds. On testing the same data size (by down-sampling), we achieved 0.65 seconds to reconstruct 512x512x256 volume. This is about 66 times faster than their results. However, this comparison is confounded by the fact that we used different graphics card (ours is much newer hardware and theirs was not specified in the paper) and hence may not be a fair comparison between OpenGL and CUDA. Therefore, with this work, it is not possible to conclude the superiority of one programming environment over the other.

We have used 45°-scan angle with ~80 projections for the *full-fan* and 2×45°-scan angle with ~160 projections for the *half-fan* mode, each projection with 1024×768 pixels and 32-bit precision (3.072 MB/projection), as the set input condition for our DTS reconstructions. However, depending on the clinical situation, one may need to use greater scan angle (or less) for better image quality, practicality, and quantitative information. We have found that the times taken for the GPU-based reconstruction technique proposed here approximately scales linearly with the number of projections (or scan angles) used. According to our tests, for 90°-scan angle with ~160 projections for the *full-fan* and 2×90°-scan angle with ~320 projections for the *half-fan* mode, it took 2.6 and 5.0 seconds, respectively. Therefore, even with the 90°-scan angle, which is considered generally too large for DTS applications in RT, the reconstruction times are still quite fast and in the realm for on-line use.

In our GPU-based FDK implementation, we have chosen to upload each projections data onto the global memory of GPU one-by-one for processing (see Figure 3-3). The reason for this approach, instead of uploading all projections data at once, was to be able to adapt to the realistic clinical situation where the projections data are acquired in the same one-by-one manner, and hence, our implementation allows the processing of each projection data as soon as they become available, in a streamlined process. As one can infer from Table 3-2, on average, our implementation can process > 13 projections-per-second (pps) and > 18 pps for the *full-fan* and *half-fan* modes, respectively, which includes from loading the projections from hard disk to CPU RAM to completely downloading the reconstructed volume from GPU global memory to CPU RAM. Since OBI nominally acquires 11 pps (with 1 gantry-revolution-per-minute), our GPU-based implementation is more than sufficient to handle the incoming projections data as they are acquired and reconstruct the entire volume immediately after completing the scan. This, of course, applies irrespective of the scan-angle range, including the full 3D CBCT. Therefore, theoretically at least, the wait time for image reconstruction (whether it is 3D DTS or 3D CBCT) can be completely eliminated using our approach.

Such a stream-lined approach using GPU, could also be of tremendous help in the stationary-gantry tomosynthesis array for radiotherapy (STAR) system, where multi-source carbon nanotubes (CNT) are attached to the gantry head, immediately below the multileaf collimators (MLC), for stationary DTS imaging for on-line image guidance. Since this system is intended for multiple DTS imaging within a single treatment session, there could be a benefit in utilizing our proposed GPU-based reconstruction strategy.

In this study, we have investigated DTS reconstruction using both the *full-fan* and *half-fan* modes. However, use of the *half-fan* mode should be discouraged as this would 1) increase the scan time, 2) increase the likelihood of patient pose change between opposite angle scans resulting in motion artifacts, 3) eliminate the possibility of single-breath-hold DTS scans, and 4) increase the patient dose. In addition, most IGRT application suffices with viewing/registering the target and its nearby structures [39,42,44,46] making larger FOV (in *half-fan* mode), in general, a non-necessity.

For image registration of the reconstructed DTS volume (called treatment-DTS) for image guidance, one cannot use the planning CT volume as the reference, but a separate reference DTS volume (called reference-DTS) needs to be constructed.[76, 86, 101] This is because the information presented in pseudo-3D DTS images is different from the full 3D CT images. To reconstruct reference-DTS volume, one needs to first construct digitally reconstructed radiographs (DRR) in cone-beam geometry, using ray-tracing technology [92, 102], simulating virtual OBI projections, each with the same gantry angle as the actual projections to be taken. Once the DRR projections are constructed, it is matter of using the same FDK algorithm, used in this study, to reconstruct the reference-DTS volume. Figure 3-8 shows an example treatment- and reference-DTS slice for a head-and-neck patient case examined in this study. With the current implementation on GPU, it takes ~140 milli-seconds-per-DRR calculation with 1024×768 pixel resolution. Therefore, to reconstruct reference-DTS (DRR calculation + FDK) from 80 DRR projections for a *full-fan* mode, it takes about 12.5 seconds. Since time constraints on calculating reference-DTS volume is not as strict as the treatment-DTS, this achievement is reasonable for routine use in clinic. With the reference- and

treatment-DTS calculators fully developed, we plan to evaluate the effectiveness of DTS-guided IGRT on various clinical sites and develop adaptive protocols.

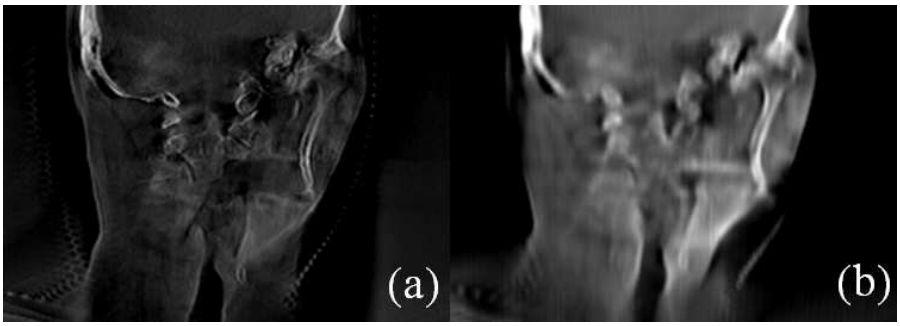

Fig. 3-8. The DTS images reconstructed using (a) the OBI projections (treatment-DTS) and (b) the DRR projections constructed from the planning CT images (reference-DTS).

The current maximum gantry rotation speed is set to 6 degrees/second (i.e., 1 rpm). This means that, for a 45°-scan angle, it would take 7.5 seconds to complete image acquisitions for a *full-fan* scan. If the reconstruction is performed immediately after, then it would take < 9 seconds from acquisition to volume reconstruction. With rapid automatic-to-manual image registration (< 30 seconds), corresponding couch shift (< 10 seconds), beam loading (< 10 seconds), and beam delivery using the latest volumetric modulated arc therapy (VMAT) [103] technology, which can deliver a single treatment fraction in generally less than 2 minutes [103, 104], it is quite possible to treat a patient from DTS scan to completion of radiation delivery in under 3 minutes. With intra-fraction motions and drifts being a major concern as the radiation is being delivered, this new work flow would ensure that patient pose is (more likely) maintained during the entire treatment fraction. In addition, of course, patient throughput will be naturally increased, an advantage that requires no further elaboration.

In this study, an ultra-fast reconstruction technique for DTS based on the FDK algorithm using CUDA-based GPU programming is proposed. The performance of

proposed algorithm was tested on twenty-five patient cases (5 lung, 5 liver, 10 prostate, and 5 head-and-neck) scanned either with a full-fan or half-fan mode on the OBI CBCT system. The GPU-based implementation achieved, at most, 1.3 and 2.5 seconds to complete full reconstruction of 512×512×256 volume, for the full-fan and half-fan modes, respectively. This resulted in speed improvement of > 87 times compared with the central processing unit (CPU)-based implementation, with visually identical images and negligible pixel-value discrepancy. With this achievement, we have shown that time allocation for DTS image reconstruction is virtually eliminated and that clinical implementation of this approach has become quite appealing. In addition, with the speed achievement, further image processing and real-time applications that may have been prohibited prior due to time restrictions can now be tempered with.

3.8 Acknowledgements

The text of Chapter 3, in part or in full, is a reprint of the material as it appears in the following publication:

Park JC, Park SH, Kim JS, Han Y, Cho MK, Kim HK, Liu Z, Jiang, SB, Song B, Song WY. Ultra-fast digital tomosynthesis reconstruction using general-purpose GPU programming for image-guided radiation therapy. Technology in cancer research & treatment 2011;10:295-306.

The dissertation author was the primary researcher and the co-authors listed in this publication directed and supervised the research which forms the basis for this chapter.

Chapter 4 Fast low-dose CBCT reconstruction using Barzilai-Borwein formulation

4.1 Introduction

In recent years, the introduction of cone-beam computed tomography (CBCT) in radiation therapy has enabled a precise, on-line positioning (and on-line/off-line re-planning) of patients[14, 18]. This is possible due to the wealth of information contained in the three-dimensional (3D)-CBCT images including 1) anatomic information[14, 18], 2) geometric information[58, 105], and 3) CT numbers for possible dose calculations for treatment verifications and plan re-optimizations[62, 106].

Because CBCT uses ionizing X-rays to image, however, there is a legitimate concern of hazardous radiation exposure to patients[69]. Due to this, the excessive use should be prohibited and the benefits-vs-harm ratio should be carefully weighed and debated for each treatment, especially for pediatric patients. This concern has now become an issue of central importance in North America, not only in radiation oncology, but in broader radiology community (e.g., Image Wisely™ and Image Gently™ campaigns).

There are rather straightforward ways to reduce the imaging dose for CBCT, that is, either 1) minimize the number of X-ray projections, 2) reduce the current setting in the X-ray tube (mA), and/or 3) reduce the total exposure time (ms). With the current-standard FDK reconstruction algorithm[19], however, reducing the projections would cause aliasing artifact (for example, see Figures 6 and 7) the severity of which depends

inversely on the number of projections, and if the mA and/or ms is reduced, the noise in the image would increase. Both of these properties of the FDK are extremely undesirable, especially if the images are used for guiding precision radiation therapy for cancer eradication.

In recent years, the exciting advances in compressed sensing theory has shown that sparse signals (at least in some known transform domain) can be reconstructed from much smaller number of samples than the Nyquist frequency would mandate[29, 30, 33, 37, 107-114]. In layman's terms, this means that nearly ideal images can be reconstructed even if only a few projections are available. This in turn, means that the imaging dose can be safely reduced without compromising the image quality. Past works have shown that, for CT-type reconstructions (both fan- and cone-beam), the total variation (TV) formulation has been particularly useful in exploiting the prior knowledge of minimal variation in the X-ray attenuation characteristics across human body[33, 37, 107, 108, 110-112, 114]. However, a practical implementation of this method still remains a challenge. The main problem is the iterative nature of solving the TV-based compressed sensing formulation, which generally requires multiple iterations of forward and backward projections of large datasets in clinically feasible time frame (e.g., <1 min). Solving this rather cumbersome problem would require multiple innovations encompassing 1) computationally efficient parallel-programming with proper hardware and 2) mathematical formulation of an efficient search algorithm for fast-solution-convergence. The former issue has been resolved successfully with the use of graphics processing units (GPU)[32, 93, 95, 115, 116]. This approach reduced the computational time from several hours to few minutes [32, 115]. In this paper, the main motivation of

our work is to propose a solution to the latter issue in order to achieve a clinically realistic reconstruction time(s) on the GPU hardware with an equivalently realistic image quality for on-line image-guided radiation therapy (IGRT).

In this work, we propose a gradient projection algorithm that handles the TV-norm regularized least squares problem, based on the Barzilai-Borwein (BB) formulation[117, 118], in such an efficient manner that we get a clinically reasonable patient image in ~12-30 iterations for a total reconstruction time of ~34-78 seconds using a single GPU card (NVIDIA GTX 295, Santa Clara, CA). Comparison of our novel approach with the FDK and other published compressed sensing techniques are presented in detail with numerical and physical phantoms, and a head-and-neck clinical patient data.

4.2 Low-dose CBCT reconstruction algorithm

The main problem is to solve the constrained convex optimization problem of the form:

$$\min_{x} f(\boldsymbol{x}) = \|\boldsymbol{A}\boldsymbol{x} - \boldsymbol{b}\|_2^2 + \lambda TV(\boldsymbol{x}) \quad s.t.\ \boldsymbol{x} \geq 0 \tag{4.1}$$

where $\boldsymbol{x}$ = unknown CBCT volume image, $\boldsymbol{A}$ = Radon transform operator, $\boldsymbol{b}$ = measured projections data, λ = regularization constant, and TV = Total Variation (TV) regularization term. In this paper, the matrices are denoted as a boldface-uppercase letters and the vectors are denoted as a boldface-lowercase letters. Note that, in Equation 1, the three-dimensional (3D) CBCT volume, $\boldsymbol{x}(i,j,k)$, is vectorized as a (1xN) dimensional matrix, $\boldsymbol{x}(l)$. Thus, we will use the two volume representations, $\boldsymbol{x}(i,j,k)$ and $\boldsymbol{x}(l)$, interchangeably in this chapter. The TV term we used in this study is defined as:

$$TV\left(x(i,j,k)\right) = \sqrt{\begin{matrix}[x(i+1,j,k) & x(i,j,k)]^2 + \\ [x(i,j+1,k) & x(i,j,k)]^2 + \\ [x(i,j,k+1) & x(i,j,k)]^2\end{matrix}} \tag{4.2}$$

In its form, the first term in Equation 4.1, i.e., the fidelity term, enforces fidelity of $\boldsymbol{x}$ with the measured projections data and the second term, i.e., the regularization term, promotes sparsity inherent in the X-ray attenuation characteristics of the human body.

4.3 Gradient projection Barzilai-Borwein formulation

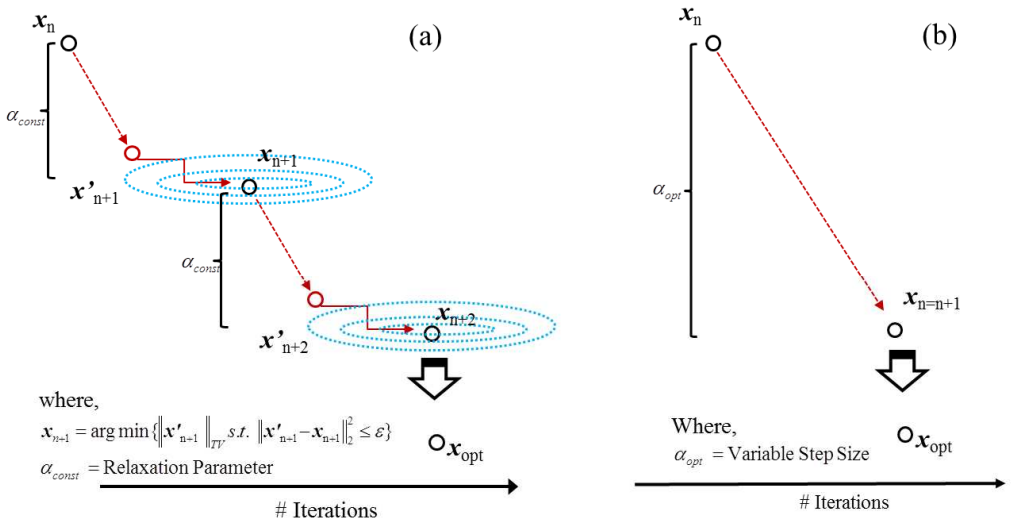

Fig. 4-1. Illustrations of (a) forward-backward splitting-type optimization, and (b) our one-step proposed approach to solve the TV-based constrained convex optimization problem in Equation 4.1.

Algorithms of significant acceptance and popularity in solving Equation 4.1, so far, have mostly been based on separating the two terms and optimizing them individually in an alternating manner, i.e., the forward-backward splitting technique[32, 33, 107, 108, 110, 114, 115]. Figure 4-1a illustrates this approach. At iteration *n*, as commonly used in the gradient descent algorithms, a fixed small step size α_{const} is chosen

to reduce the fidelity term to obtain an intermediate solution $\boldsymbol{x}_{n+1}'$. The (n+1)-th solution $\boldsymbol{x}_{n+1}$ which has the minimal total variation is then searched around the $\boldsymbol{x}_{n+1}'$ to complete an iteration. This procedure is repeated until a desired solution $\boldsymbol{x}_{opt}$ is achieved. As we will show in this work, however, that this approach may not result in a fast convergence due to this two-step approach. Intuitively, an algorithm that optimally reaches $\boldsymbol{x}_{n+1}$ in a single step, at each iteration, using a variable step size (α_{opt}) would be more efficient computationally and faster in convergence (see Figure 4-1b). This is our intuition and is exactly what is proposed here.

We propose to use a gradient projection algorithm that iteratively seeks a solution to Equation 4.1 in the direction of the projected gradient while enforcing a non-negativity of the found solution. Let g_n be the gradient of $f(\boldsymbol{x}_n)$ defined as:

$$\boldsymbol{g}_n = \boldsymbol{A}^T\left(\boldsymbol{A}\boldsymbol{x}_n - \boldsymbol{b}\right) + \lambda\nabla\, \boldsymbol{TV}\left(\boldsymbol{x}_n\right) \tag{4.3}$$

where ^{T} is the transpose operator of the Radon transform matrix $\boldsymbol{A}$, which is physically interpreted as a back-projection operation on $\boldsymbol{x}$. We then solve Equation 4.1 iteratively using the gradient projection method:

$$\boldsymbol{x}_{n+1} = \left[\boldsymbol{x}_n - \alpha_n \boldsymbol{p}_n\right]^+ \quad where \;\; [\;]^+ = max[\;,0] \tag{4.4}$$

where

$$p_n(\boldsymbol{l}) = \begin{matrix} g_n(\boldsymbol{l}) & if\ g_n(\boldsymbol{l}) \le 0 \;\; or\; x_n(\boldsymbol{l}) > 0 \\ 0 & otherwise \end{matrix} \tag{4.5}$$

Here, α_n denotes the step size at iteration n, l denotes the voxel position index, and $\boldsymbol{p}_n$ denotes the projected gradient of the function $f(\boldsymbol{x})$ at $\boldsymbol{x}_n$.

The speed of convergence would be highly dependent on choosing a proper "step-size" α_n in Equation 4.4, at each iteration. Remember, the less the number of iterations

used to find the optimal solution $\boldsymbol{x}^*$, the less the number of times one needs to calculate the $\boldsymbol{A}$ and $\boldsymbol{A}^T$, which are computationally very expensive.

There are few approaches in choosing an appropriate α_n including 1) a fixed, small α_n throughout, and 2) a variable α_n obtained through a back-tracking line-search method that satisfies a certain condition for ensuring convergence. For example, the well-known Armijo condition[119] enforces not only a monotonic decrease in the objective function but also a sufficient decrease of the objective function in each iteration for guaranteeing the convergence. The first, "fixed step-size" method is simple to implement yet finding an appropriate α_n is not trivial as there's a tradeoff between convergence speed and image quality. The second, "line-search" method is popular and guarantees a monotonic convergence but incurs a relatively high computational burden as the back-tracking line-search is an iterative process in itself, which is analogically similar to that illustrated in Figure 4-1a, i.e., iteration within iteration.

In this work, we propose a third and alternative method using an approximate second-order solver, proposed by Barzilai and Borwein (BB)[117, 118], where the objective function may not be monotonically decreasing as in the back-tracking "line-search" method, but much faster convergence is achieved. Unlike most traditional approaches that ensure convergence to an optimal solution by imposing a rather conservative condition of monotonic decrease of the objective function at each and every iteration, the BB method relaxes this constant decrease requirement in order to achieve even faster convergence in the long run [117, 120]. Specifically, the conventional approaches calculate each step-size based on the current gradient of the cost function. As a result, a monotonic convergence is guaranteed throughout the iterative process.

However, in the BB approach, the step-size is chosen based on both the current gradient and the previous gradient which could result in a non-monotonic convergence. Utilization of this additional information, i.e., the past gradient, results in a faster convergence although the monotonic convergence behavior is not guaranteed. Basically, it calculates each step with the formulation (compare with Equation 4.4):

$$\boldsymbol{x}_{n+1} = \left[\boldsymbol{x}_n - \boldsymbol{H}_n^{-1}\boldsymbol{p}_n\right]^+ \tag{4.6}$$

where H_n is an approximation to the true Hessian of $f(\boldsymbol{x})$ at $\boldsymbol{x}_n$ (i.e., approximate second-order solver). To calculate $\boldsymbol{H}_n^{-1}$, the BB formulation makes a simple approximation to the Hessian by setting $\boldsymbol{H}_n = \eta^{(n)}\boldsymbol{I}$, where $\boldsymbol{I}$ denotes an identity matrix and $\eta^{(n)}$ is chosen to approximate the true Hessian over the most recent two iteration steps as:

$$\boldsymbol{p}_n - \boldsymbol{p}_{n-1} \approx \eta^{(n)}\left[\boldsymbol{x}_n - \boldsymbol{x}_{n-1}\right] \tag{4.7}$$

where $\eta^{(n)}$ is calculated at each iteration that satisfies Equation 4.7. In practical implementation, the optimal $\eta^{(n)}$ is solved in the least squares sense by:

$$\eta^{(n)} = \frac{\left[\boldsymbol{x}_n - \boldsymbol{x}_{n-1}\right]^T\left[\boldsymbol{p}_n - \boldsymbol{p}_{n-1}\right]}{\left\|\boldsymbol{x}_n - \boldsymbol{x}_{n-1}\right\|_2^2} \tag{4.8}$$

Once $\eta^{(n)}$ is calculated, the Equation 4.6 is updated by:

$$\boldsymbol{x}_{n+1} = \left[\boldsymbol{x}_n - (\eta^{(n)})^{-1}\boldsymbol{p}_n\right]^+ \tag{4.9}$$

For $n = 0$, since $\boldsymbol{x}_{n-1}$ and $\boldsymbol{p}_{n-1}$ in Equation 4.8 are not known, we initialize $(\eta^{(n=0)})^{-1}$ as:

$$\left(\eta^{(0)}\right)^{-1} = \frac{\left\|\boldsymbol{g}^{(n)}\right\|_2^2}{\left\|\boldsymbol{A}\boldsymbol{g}^{(n)}\right\|_2^2} \tag{4.10}$$

which is the closed form solution of the optimal step size in the quadratic fidelity term in Equation 4.1[119].

The advantage of this technique is that, first, at each iteration, one needs to only carry over $\boldsymbol{x}_{n-1}$ and $\boldsymbol{p}_{n-1}$ to calculate $\eta^{(n)}$, which must be calculated in the previous step anyway. Thus, unlike, for example, the GP-BL method where the step size is calculated via an iterative procedure (step 3 in Figure 2-2c, more on this later), there are no *extra* calculations/iterations that need to be performed to compute α_n which affects the speed of the optimization much favorably. Second, as found in the original BB publication[117], the convergence of Equation 4.6 should be faster than the standard first-order methods such as the back-tracking line-search discussed above, and as we'll show in this work. And, finally, since the entire $f(\boldsymbol{x})$ is minimized simultaneously in Equation 4.1 and not alternatively as in the other works discussed above; e.g., Figure 4-1a, the overall complexity of the implementation is simplified while still guaranteeing an optimal solution.

4.4 Algorithm implementation

In our implementation of this Gradient-Projection-Barzilai-Borwein (GP-BB) method, to speed up the algorithm further, the following has been adopted:

A. For $n = 0$, we initialize $\boldsymbol{x}_0$ = FDK. This result in a faster convergence compared with setting $\boldsymbol{x}_0 = 0$.
B. Two-resolution-level optimization. That is, we first set $\boldsymbol{x}$ to 256×256×70 volume, optimize, then resample to 512×512×70 volume for a second-level optimization. The resolution at level one and two are 0.97×0.97×2.0-mm and 0.49×0.49×2.0-mm, respectively.
C. The entire code is structured and implemented in C with the CUDA programming

environment (NVIDIA, Santa Clara, CA) to utilize the massive parallel computational capability of the GPU hardware. We used a single GTX 295 card (~$500^{US}) that consists of 480 processing cores with 1.24 GHz clock speed and 1,792 MB memory. In terms of CPU, we used Intel Core™ i7 with 2.68 GHz clock speed, 12.0 GB DDR3 RAM, on a 64-bit Window 7 OS.

For our application, three major computational tasks were parallelized in the CUDA environment: 1) the forward projection $\boldsymbol{A}$, 2) the back projection $\boldsymbol{A}^T$, and 3) the vector operations to calculate $\eta^{(n)}$, $\boldsymbol{Ax}$-$\boldsymbol{b}$, $TV(..)$, etc. For the forward projection operations, we have set each detector pixel as a GPU thread and summed the image voxels that happen to lie in the path from the cone-beam source to the corresponding pixel. Since this summation of voxels, in the ray path, can be independently computed for each detector pixel, this feature has been utilized in the GPU coding as a parallel computations [116]. For the back projection operations, we have instead set the each image voxel as a GPU thread. Similar strategies were implemented on the vector operations as well.

4.5 Performance evaluation and experimental setup

To evaluate the performance of our GP-BB algorithm, we have compared it with three other algorithms, the two of which are published. First, the adaptive-steepest-descent-projections-onto-convex-set (ASD-POCS) method proposed by Sidky and Pan [33] (described in Figure 4-1a) was implemented. Second, the soft-threshold filtering approach (STF) proposed by Yu and Wang [114] was implemented. This algorithm is essentially similar to the ASD-POCS except that an approximate solution is proposed

over iteratively calculating the second step, shown in Figure 4-1a (i.e., minimizing the total variation step), to reduce the computational burden. Third and finally, we have implemented a first-order Gradient-Projection-Backtracking-Linesearch (GP-BL) algorithm that attempts to simultaneously minimize the both terms in Equation 4.1 in a single step as opposed to the forward-backward splitting technique in ASD-POCS and STF. This single step approach is similar to the GP-BB except that an acceptable α_n in Equation 4.4 is searched without the approximate second-order Hessian information as explored in the GP-BB method. Essentially, at each iteration in Equation 4.4, α_n is found through the back-tracking line-search along the direction of the current gradient.

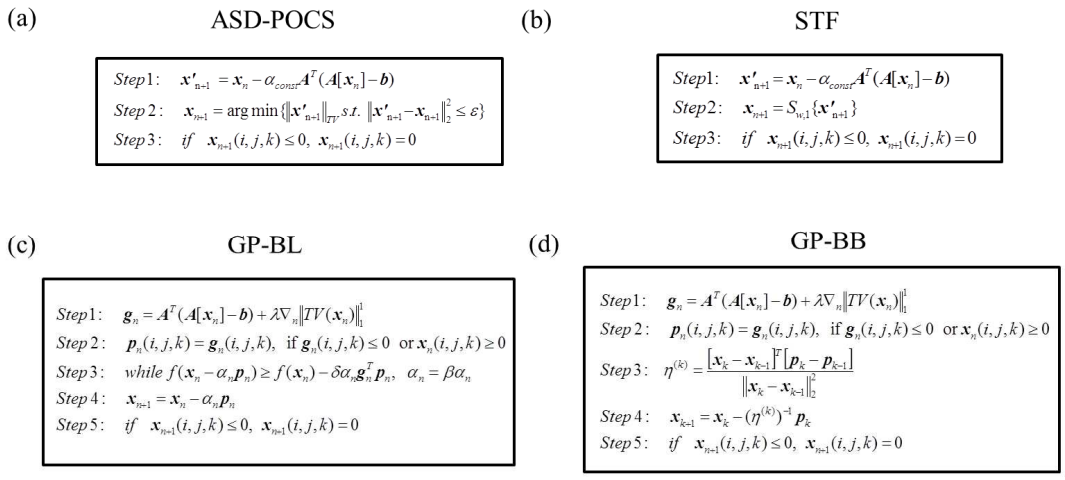

Fig. 4-2. Illustration of the computational processes required at each iteration for the four algorithms: (a) ASD-POCS, (b) STF, (c) GP-BL, and (d) GP-BB.

Computational processes required at each iterative process for each of these algorithms are illustrated in Figure 4-2. First, the ASD-POCS iteration is shown in Figure 2a. The algorithm starts by finding the intermediate solution $\boldsymbol{x}_{n+1}$' through a SART-type approach with a constant step-size where a promotion of the data fidelity term only is

considered (step 1). The TV-norm is then minimized around this $\boldsymbol{x}_{n+1}'$ through an iterative, convex optimization process for which we employed a commonly used steepest descent approach in this paper (step 3). Therefore, at each iterative step of the ASD-POCS algorithm, an additional iterative process is required (step 3). Second, the STF approach proposed by Yu and Wang [114] is illustrated in Figure 4-2b. As shown on the figure, the algorithm starts exactly same as the ASD-POCS for step 1. However, instead of using an iterative, convex optimization procedure to minimize the TV around the intermediate solution $\boldsymbol{x}_{n+1}'$, the algorithm employs a batch, non-iterative, soft-threshold filtering algorithm to remove the extra iterative step, and hence reduces the computational time. The soft-threshold filtering procedure is denoted by $S_{w,1}(\boldsymbol{x}_{\boldsymbol{n+1}}')$ in step 2 on Figure 4-2b. It is a regularization function that updates the $\boldsymbol{x}_{n+1}'$, as a function of TV($\boldsymbol{x}_{n+1}'$), using a closed form heuristic formula. Interested readers are encouraged to read Yu and Wang [114] for details. Third, the GP-BL algorithm proposed here, alternatively to the GP-BB, is illustrated in Figure 4-2c. It starts by calculating the gradient of the cost function consisting of the data fidelity and the regularization terms (step 1), followed by a projection of the gradient (step 2). At step 3, a back-tracking line-search is performed by evaluating the objective function with a decreasing step size α_n until a certain condition is satisfied to ensure convergence. For that we employed the well-known Armijo condition stated by the inequality in step 3 which not only enables a monotonic decrease in the objective function but also satisfies a sufficient decrease criterion for convergence to the optimal solution. In this study, we set the constants δ and β to 0.02 and 0.7, respectively. Once the step size α_n is obtained, a gradient descent

step is conducted while enforcing the non-negative constraint (step 4). Finally, the proposed GP-BB algorithm is illustrated in Figure 4-2d. Referring to the figure, steps 1 and 2 are the same as those in the GP-BL algorithm. However, as we have illustrated our algorithm mathematically, the iterative back-tracking line-search in Figure 4-2c is replaced by a much simpler, non-iterative vector operations for the computation of $\eta^{(n)}$ (step 3). Therefore, favorably compared with the GP-BL approach, finding the step size is performed without the extra iterative calculation of the back-tracking line-search. The gradient descent step is then conducted $\alpha_n = (\eta^{(n)})^{-1}$ using (step 4). It should be noted here though that there have been very recent studies reporting the effectiveness of the BB-based approaches for CT reconstruction. These efforts could complement our work in developing the most mature form of the BB-based CT/CBCT reconstruction techniques.

The Shepp-Logan numerical phantom, the CatPhan 600 physical phantom (The Phantom Laboratory, Salem, NY), and a clinically-treated head-and-neck patient acquired from the TrueBeam™ system (Varian Medical Systems, Palo Alto, CA) were used for comparison purposes. For the TrueBeam™ scans, a total of 364 projections were acquired in a 200-degree rotation, in a full-fan mode. The imager has 1024×768 pixels with 0.388×0.388-mm resolution. This was down-sampled to 512×384 pixels with 0.776×0.776-mm for the reconstructions. Evenly spaced angles were sub-sampled and used for varying the number of projections for the image reconstruction.

4.6 Results

Figure 4-3 shows the reconstructed 2D images of the Shepp-Logan phantom using the four algorithms described earlier. A total of 40 projections in fan-beam geometry were used for the reconstructions. As can be seen, the Gradient Projection (GP)-type algorithms outperforms the forward-backward splitting-type algorithms in terms of image quality and speed of convergence. At about 50 and 30 iterations, the GP-BL and GP-BB algorithms show convergence, respectively, whereas the ASD-POCS and STF algorithms clearly still needs further convergence at 50 iterations. Visually, the GP-BB shows the fastest convergence and this is quantitatively demonstrated in Figures 4-4 and 4-5. In Figure 4-4, the line profile comparison is shown after 30 iterations, for example. It is clear from this figure that the level of agreement to the ground truth goes in the order of GP-BB > GP-BL > STF & ASD-POCS. This finding holds true at all levels of iterations, as illustrated in Figure 4-5. Here, the relative error is defined as the mean-squared percent error from the ground truth pixel values:

$$Reletive\,Error\,(\%) = \frac{\sum_{i,j,k} (\boldsymbol{x}_{i,j,k} - \boldsymbol{x}_{i,j,k}^{GroundTruth})^2}{\sum_{i,j,k} (\boldsymbol{x}_{i,j,k}^{GroundTruth})^2} \times 100 \tag{4.11}$$

where $x_{i,j,k}$ corresponds to the voxel values in the reconstructed volume x and $x^{GroundTruth}$ refers to the ground-truth values of the Shepp-Logan phantom used. As can be seen from the figure, all three algorithms other than the GP-BB continue to decrease at 50 iterations, whereas the GP-BB algorithm reaches saturation at ~25-30 iterations. One thing to note is that, due to the non-monotonic feature of the BB algorithm discussed in section II, the relative error does not decrease in a smooth manner due to the inherent properties of calculating the step size without conducting a line-search at each iterative step.

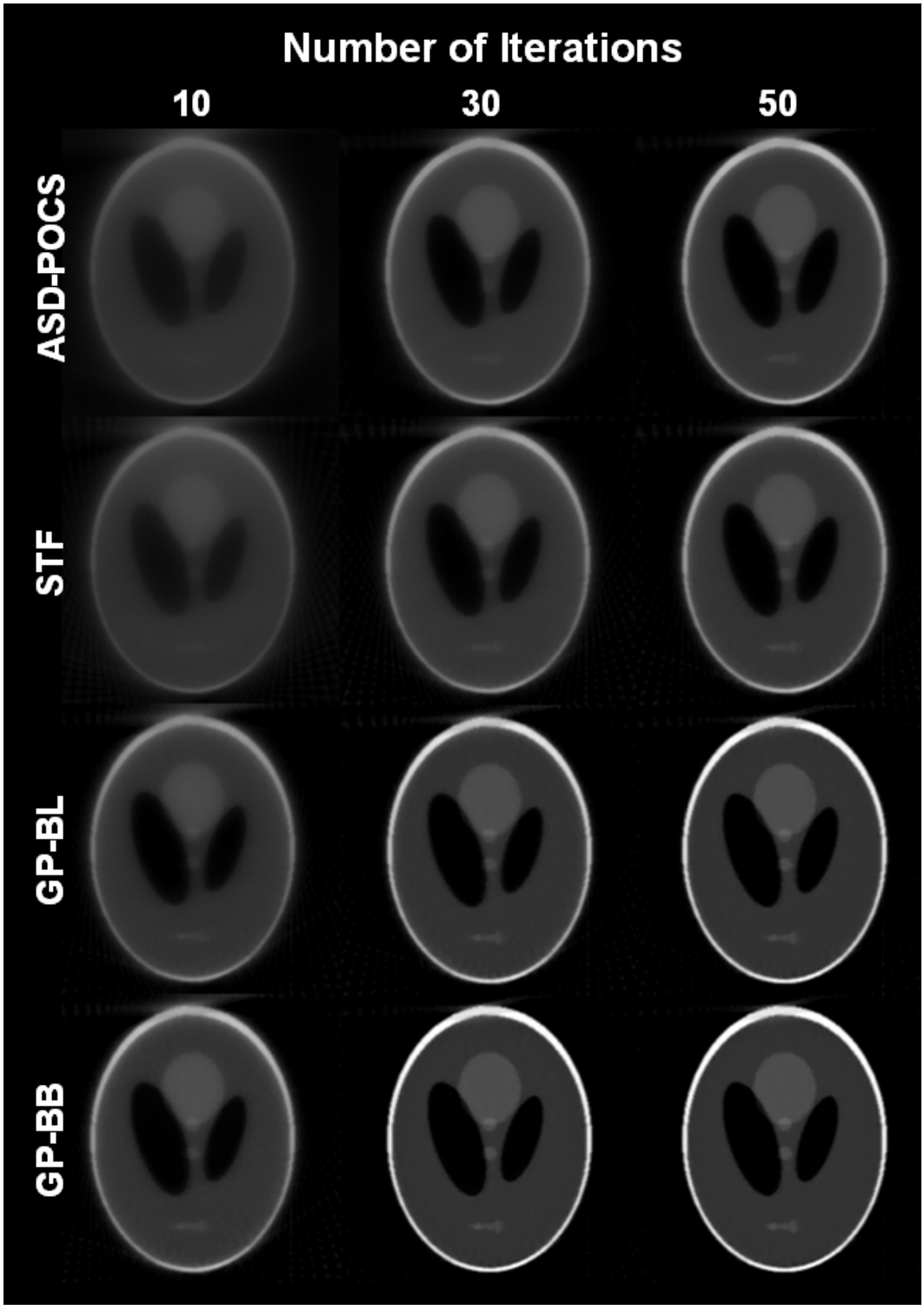

Fig. 4-3. The reconstructed images of the Shepp-Logan phantom, using the respective four algorithms, as a function of 10, 30, and 50 iterations. A total of 40 projections in fan-beam geometry were used for the reconstructions.

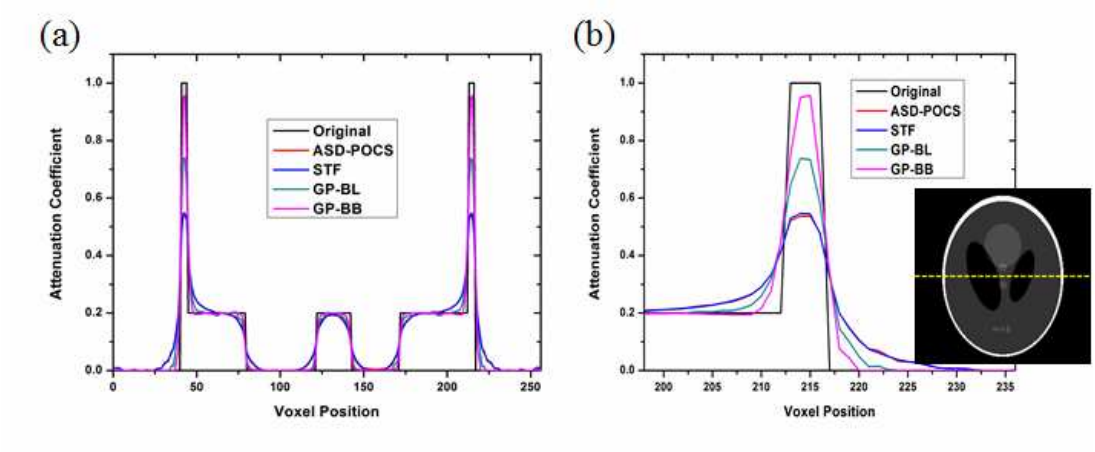

Fig. 4-4. Line profiles of the respective four algorithms with the (a) full line across the Shepp-Logan phantom, and (b) magnified view of the right one-third. The figure inset shows where the line profiles were generated.

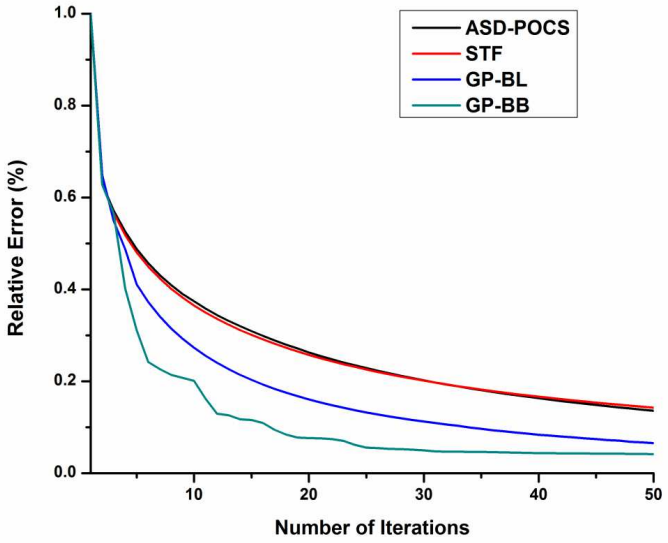

Fig. 4-5. Mean-squared relative percent error as a function of the number of iterations, for the respective four algorithms. The Shepp-Logan numerical phantom was used as the gold standard.

In order to show the computational efficiency of each algorithm, we have measured the computational time performances of the four algorithms implemented on the same GPU card (see Table 4-1). To conduct a fair comparison, we kept all experimental conditions the same for all algorithms. That is, the number of iterations was

set to 50, the reconstruction volume was set to 256×256×64, the number of projections used was 42, the detector size was 512×384, the unknown CBCT volume image was all initialized to zero (i.e., $\boldsymbol{x}^{(0)} = \mathbf{0}$), and the multi-resolution optimization was not used. It is found that the GP-BL algorithm takes the longest time to compute due to the high computational cost of conducting the back-tracking line-search, at each iteration. It can also be observed that those algorithms that have iterations within iterations, i.e., ASD-POCS and GP-BL, the standard deviation is also large compared to the other two algorithms that do not have a second iteration loop. The GP-BB and STF algorithms have a consistent computational time and, moreover, their convergence is noticeably faster than the other two algorithms. It should be noted, though, that our implementations of the ASD-POCS and STF may not have been exactly reproduced as the ones originally proposed and implemented. Although we attempted to make the fairest comparison by best implementing the original ideas of the algorithms using the published information, it is difficult to reproduce the same exact performance due to a difference in the experimental setup and data used. As a result, we acknowledge that our evaluations of these algorithms may not represent their best possible implementation and thus performance and image quality.

Table. 4-1. Time measurement profile of each algorithm processed for 50 iterations.

	ASD-POCS	STF	GP-BL	GP-BB
Total Computational Time (Sec)	60.47	22.77	66.37	24.56
Average Computational Time/Iteration (Sec)	1.20	0.45	1.32	0.49
Standard Deviation	0.36	0.03	0.18	0.04

In addition to the comparisons with the compressed-sensing-type algorithms, we've also compared the GP-BB against the conventional and commercially-used, filtered backprojection-type algorithm proposed by Feldkamp, Davis, and Kress (FDK, 1984)[8]. Figure 4-6 show the 3D volumes reconstructed with the two algorithms, using some or all of the 364 projections acquired from the TrueBeam™ CBCT system. Reconstruction times are labeled on the figure. As can be seen, even with the dose reduction to $1/9^{th}$ (=40/364 projections), Figure 4-6b shows a reasonable image quality achieved by the GP-BB algorithm comparable to that of the FDK reconstructed image using all of 364 projections (Figure 4-6c) with less noise, while completing this in under 12.6 seconds. Needless to say, the image quality of Figure 4-6b is better with minimal aliasing artifacts compared with that of Figure 4-6a, which is FDK reconstructed volume using the same 40 projections. To note, this achievement of 12.6 seconds is about an order of magnitude faster than that of the latest report on the GPU-accelerated forward-backward splitting-type algorithms, discussed in Figure 1a[32, 115].

Figure 4-7 shows a matrix view of the various image qualities achieved, using the GP-BB algorithm, as functions of both the number-of-projections and the number-of-iterations, for the head-and-neck example patient. The window and level were kept the same for all images. The first row show the images reconstructed with the FDK for comparison. It is observed that as the number-of-projections increases, the image quality increases in both the FDK and GP-BB algorithms, and as the number-of-iterations increases in GP-BB, the image quality increases too. It is also observed that, in GP-BB, the qualitative increase in image quality is relatively more significant from 90 to 120 projections than from 120 to 180 projections. This also means that the FDK-initialized

GP-BB algorithm always does better than just the FDK alone, for any number-of-iterations per given number-of-projections.

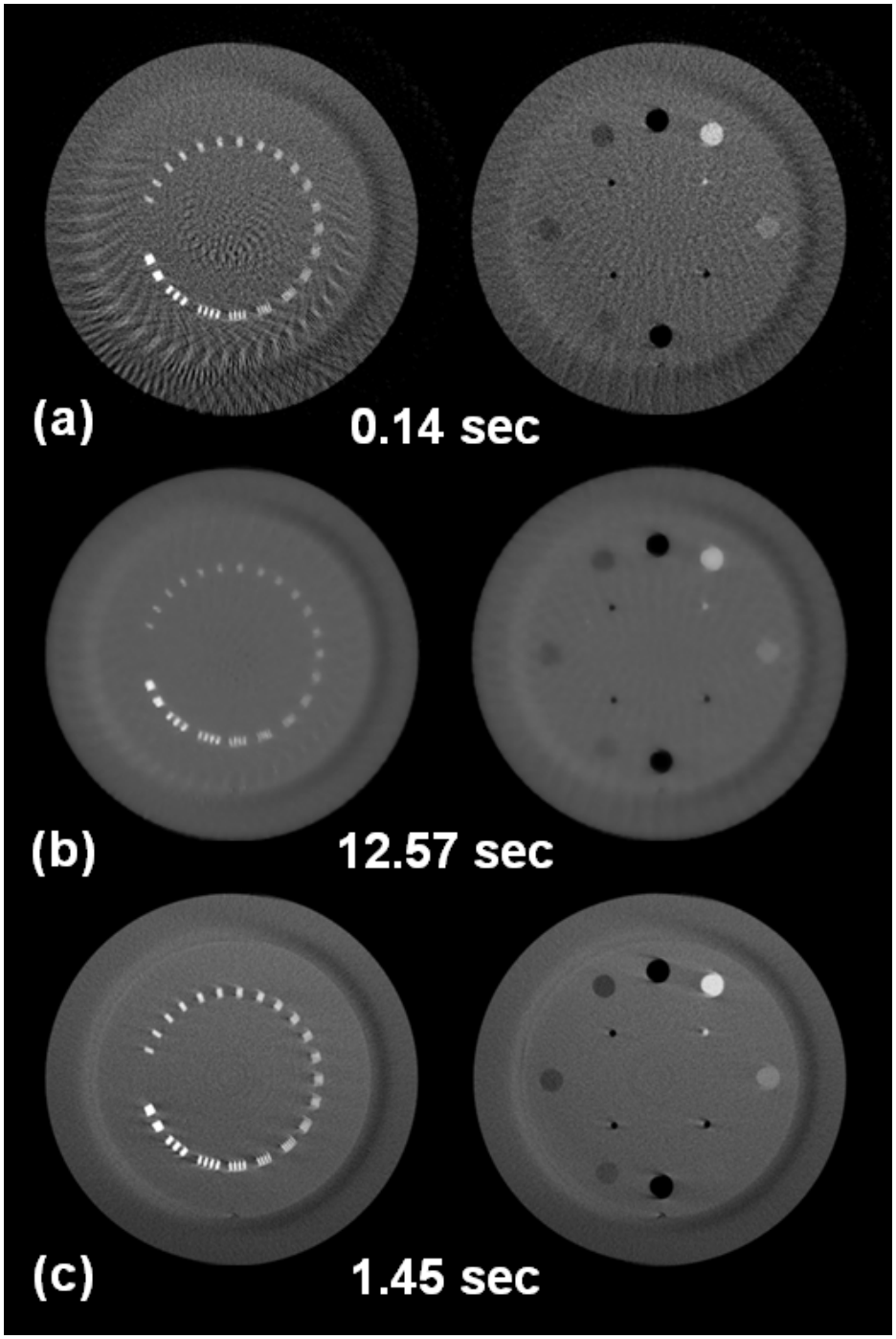

Fig. 4-6. Spatial and contrast resolution slices of the reconstructed CatPhan 600 phantom using (a) FDK with 40 projections, (b) GP-BB with 40 projections in 12 iterations, and (c) FDK with 364 projections. The reconstruction times are listed on the figure.

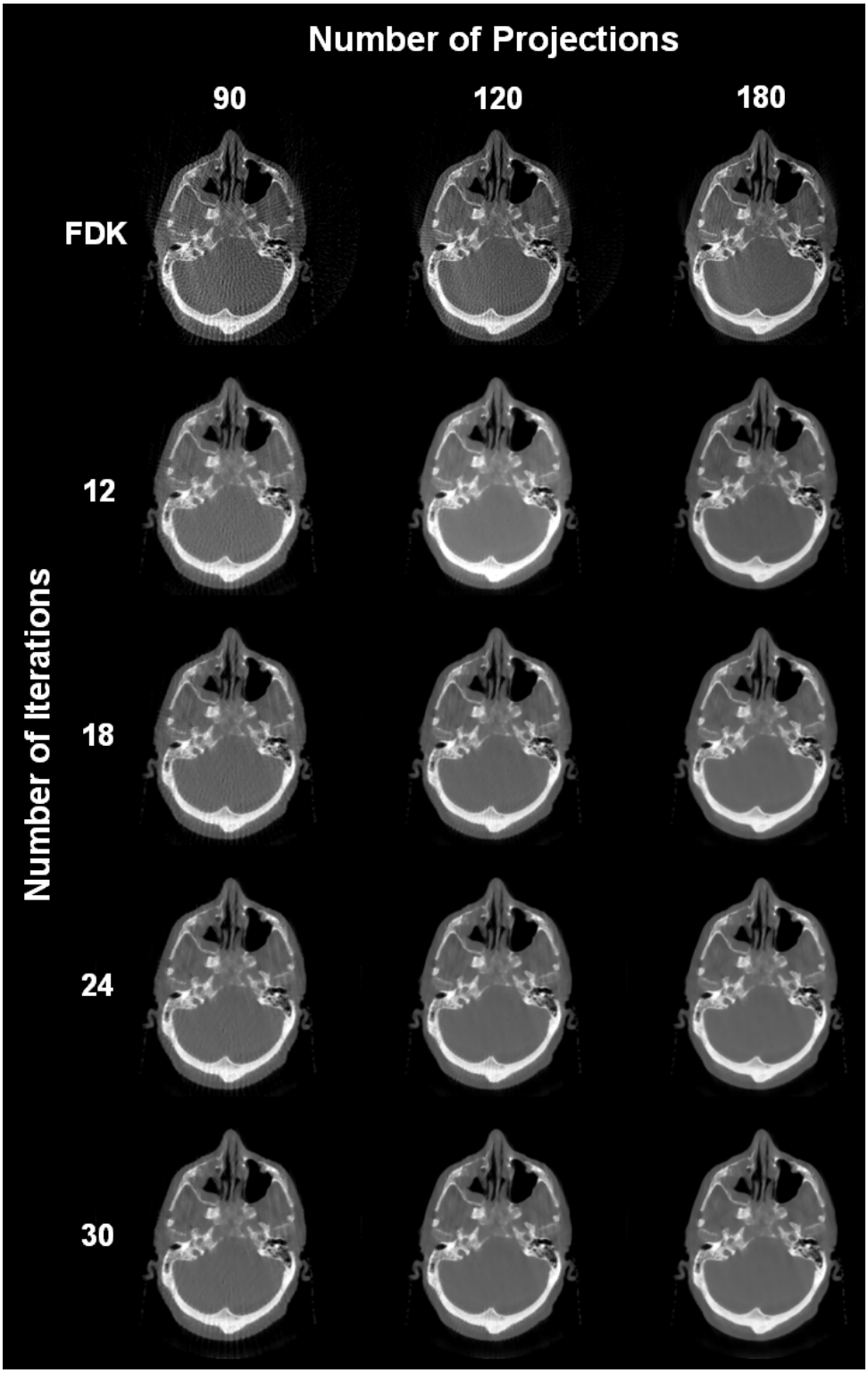

Fig. 4-7. A matrix view of the various image qualities achieved, using the GP-BB algorithm, as functions of number-of-projections and number-of-iterations, for the head-and-neck example patient. The window and level were kept the same for all images.

Table. 4-2. List of the reconstruction times recorded for various projections and iterations tested.

Time [sec]	**# of projections (views) used**				
# of iterations	**60**	**90**	**120**	**180**	**364**
FDK	**0.27**	**0.34**	**0.50**	**0.75**	**1.45**
6	**9.891**	**14.48**	**19.25**	**28.35**	**58.11**
12	**17.58**	**25.57**	**33.77**	**49.94**	**101.83**
18	**24.88**	**36.55**	**48.21**	**71.92**	**146.51**
24	**32.92**	**47.62**	**62.86**	**92.86**	**188.37**
30	**39.91**	**58.87**	**77.99**	**116.55**	**234.51**

Table 4-2 shows a comprehensive list of the reconstruction times recorded for various combinations of input condition, encompassing that of the examples shown in Figure 4-7. From this list and Figure 4-7, we can deduce that, although subjective, visually a “reasonable” image quality for clinical use can be obtained in the range of ~12-30 iterations with ~120-180 projections. The range of reconstruction times would be between ~34-117 seconds, that is, all are within ~2 minutes or less. In terms of dose reduction, this would be on the order of ~1/3-1/2 depending on the projections used (i.e., 120/364 or 180/364 projections, respectively).

Figure 4-8 displays, side-by-side, the GP-BB-reconstructed images using 120 projections (Figures 4-8b-e) in closer comparison with the FDK-reconstructed image using 364 projections (Figure 4-8a; currently in-use in clinic). The images using only the 120 projections are displayed here, as opposed to images using 180 projections, since our interest is in generating a reasonable quality images with a minimally necessary radiation

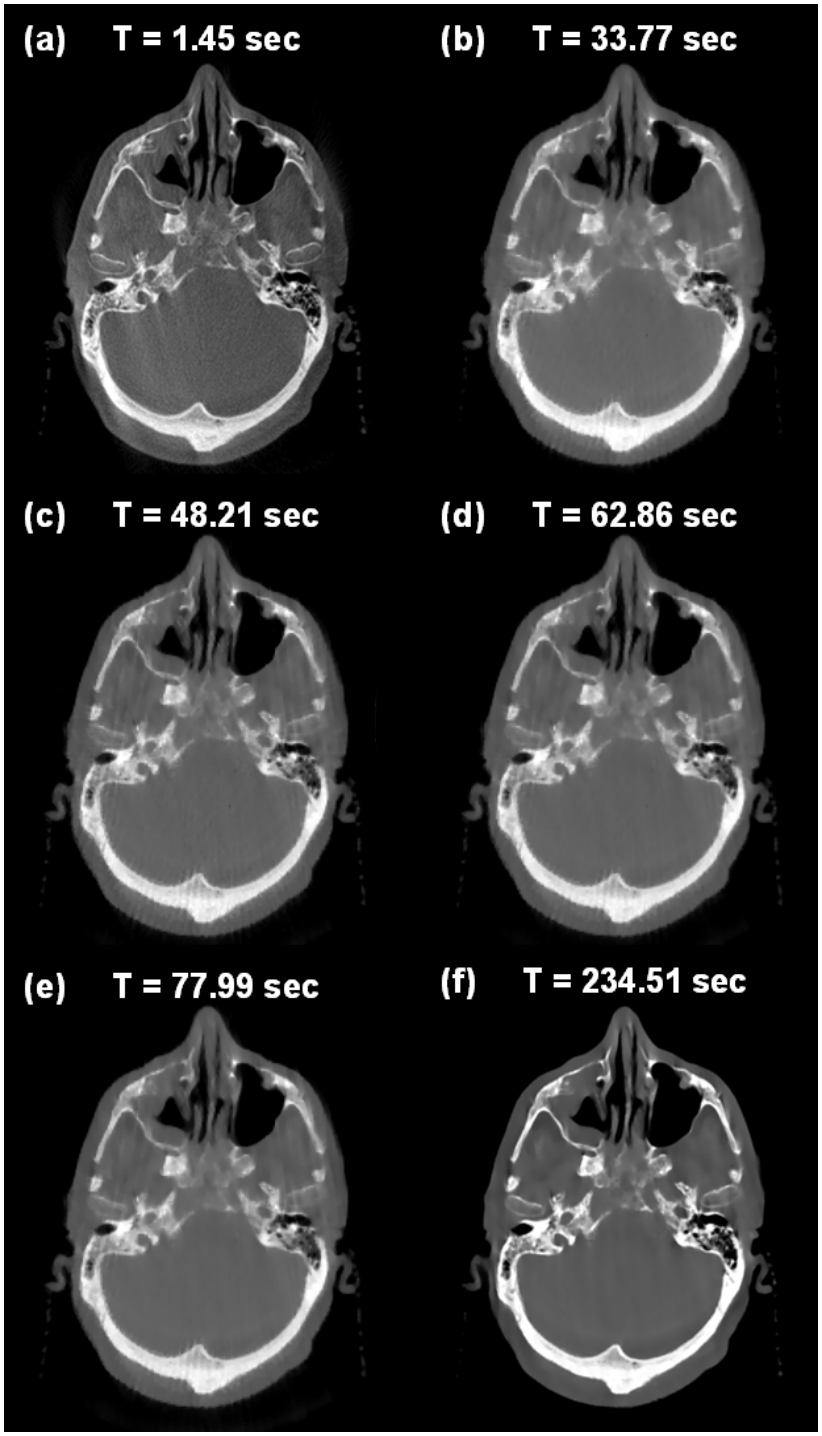

Fig. 4-8. Selected images from Figure 6; (a) FDK using 364 projections, (b) GP-BB with 12 iterations using 120 projections, (c) GP-BB with 18 iterations using 120 projections, (d) GP-BB with 24 iterations using 120 projections, and (f) GP-BB with 30 iterations using 364 projections. The reconstruction times are listed on the figure.

dose. Also, as mentioned, there's a relatively more benefit in terms of image quality going from 90 to 120 than from 120 to 180 projections (Figure 4-7), i.e., diminishing increase in image quality for a given increase in dose. The GP-BB-reconstructed image using 364 projections is also displayed (Figure 4-8f) to show the limiting image quality that can be achieved with the GP-BB algorithm. First of all, the upper-limit GP-BB image using 364 projections is a visually better quality image than that of the FDK (i.e., less noise, streaking artifacts around bones, etc.), which reaffirms our results in Figure 4-7 that, given equal dose, the GP-BB always does better. But, more importantly, the image qualities of the 120-projection-images are comparable to the FDK image, and, with a reasonable reconstruction times of ~34-78 seconds. Of course, the necessary image quality for clinical use is quite subjective and requires further (clinical) testing to determine for each site, which is of our future research, it is still encouraging that a "visually" similar quality images can be obtained in one-third the dose, in a "reasonable" time frame. To the best of our knowledge, this computational speed achieved using the GP-BB algorithm is the fastest compressed sensing-type optimization that have been proposed for the CBCT reconstruction to date [32, 33, 37, 110, 113-115].

4.7 Discussion

A. Algorithm performance

The translation of compressed sensing-based CBCT reconstruction algorithms onto radiation therapy clinical settings has been difficult due to the fact that its mathematical formulation needs to be solved numerically rather than analytically, thus requiring a prohibiting time to solve. A single, complete iteration involves at least one

forward and one backward projection calculations, which are computationally expensive. Although significant amount of computational time can be spared by parallelizing the task with GPU programming [95, 116, 121-123], still, the majority of time (e.g., >80%) spent in the reconstruction is on calculating the forward and backward projections. Therefore, for an algorithm/technique to be efficient, it must 1) require a minimal number of forward and backward projection calculations per iteration, and 2) converge in a minimal number of total iterations.

Besides the well-known forward-backward splitting technique that we compared in this work, there are other compressed sensing-based methods with a focus on achieving faster convergence than previously reported [37, 124] that base on the Nestrov's first order method. However, on reviewing their works, it was observed that although the convergence rate (determining the number of iterations needed to reach a desired solution) outperforms the comparing counterparts, the algorithms require multiple forward and backward projection calculations at each iteration[37] or an extra iterative procedure to calculate the additional unknown parameters, leading to an increased reconstruction times. The non-convex prior image constrained compressed sensing (NCPICCS) algorithm reported by Ramirez-Giraldo, *et al.*[124] also suffers from the similar complexities where an extra-calculation of forward and backward projection is required to calculate each step size. The GP-BB algorithm, on the other hand, requires 1) only one forward and one backward projection calculations per iteration, which is the least number required for solving any iterative reconstruction techniques, and 2) a simple gradient step size calculation (i.e., Equation 4-8) that needs only the prior and current values of the gradient and the image volume, which occupy <300MB of memory, thus

facilitating easy incorporation onto a single GPU card memory (1.7GB storage). In our implementation, calculating the step size takes a negligible time, so the great majority of the time is spent on the forward and backward projection calculations (e.g., >98% of time). This demonstrates that the GP-BB algorithm requires only a minimal computational load needed to reach a solution

B. Dose reduction

It needs to be stated that, if reconstruction time is of no issue and thus enough iterations are allowed, all of the compressed sensing-type algorithms evaluated in this study will eventually reach an optimal solution as anticipated from Figure 5. That means, if an equal number of projections are used with each algorithm, then the achieved image quality at the end will be identical and hence no benefit, in terms of dose and/or image quality, will be observed for any one algorithm. However, we do not have an infinite time to spare, especially in an on-line IGRT environment, and hence an algorithm that can produce the most optimal image under a reasonable time and with a least amount of projections (i.e., dose), is favored. Our proposed GP-BB algorithm relatively fits well in this respect. In the Catphan phantom experiment, the GP-BB produced a reasonable image with a highly under-sampled projections (40/364≅89% dose reduction; see Figure 6), in ~12.6 seconds. However, for a clinical patient case, about 120 projections or more were needed to generate a reasonable quality images, taking a respectable ~34-78 seconds. This achievement still represents a significant dose reduction of ≅67%, but any further dose reduction (i.e., less number of projections) is generally not recommended due to a fast degradation of the image quality, although the reconstruction times will further decrease. This has also been the observation of earlier works as well [32, 112,

115]. The possible reason for needing more projections in patients than in phantoms is that the internal anatomy of humans are relatively less sparse, and thus require more data to properly represent it. In addition, since the sparseness is organ-patient specific, much research is needed to determine the appropriate number of projections needed, and hence the achievable dose reduction, for each organ and patient. The appropriate mAs setting, per projection, would be another parameter that needs to be studied as well. Utilizing prior information such as the planning CT would be a one good way to decide what dose reduction is possible/appropriate for each case.

C. Regularization parameter

Regularization parameter λ, in Equation 4-1, is one of the most influential parameters affecting the image quality. It was our experience that the higher this value, the blurrier and smoother the images, and the smaller it is, the sharper and noisier the images, in opposite. This is due to the fact that λ is the weighting factor for the TV-norm regularization term in Equation 4-1. Thus if λ is high, then more weight is given in the GP-BB optimization to minimize the variation across the image and hence the blurrier but smoother the look. Oppositely, if λ is low, then more weight is given to the fidelity term in Equation 4-1 and hence the high frequency information will survive, thus preserving the noise and streaks. For example, we observed some irregular ripples in a uniform phantom region, in Figure 4-4, when a small is applied, demonstrating the importance of a proper/optimal λ selection.

Recently, there have been considerable interests in optimizing the λ value in a regularization-type optimization problems[26, 125]. Although the purpose of these works is for different applications, we anticipate that similar strategies can also be applied to the

TV-based CBCT reconstruction problem as well. But, for now, since there is no global standard in λ value(s)[112] for CBCT reconstructions, the selection of λ was subjectively picked by painstakingly repeating a large range of values. From this experience, we learned that for fewer projections, a relatively high λ is needed to suppress the overwhelming noise and streaks, while for more projections, a relatively low λ is sufficient. Specifically, with 100 or less projections, we set λ = 0.0075, and for >100 projections, we set λ = 0.0025, for the head-and-neck patient case. Obviously, more research is needed in finding an optimal λ values for various situations, and that this value is likely not only number-of-projections dependent, but will also be patient and site dependent as well. For best clinical practice, an automated selection of λ based on a prior knowledge, whatever that may be (including a planning CT), will help facilitate the clinical translation of this technology into a busy on-line radiation therapy environment.

4.8 Acknowledgements

The text of Chapter 4, in part or in full, is a reprint of the material as it appears in the following publication:

Park JC, Song B, Kim JS, Park SH, Kim HK, Liu Z, Suh T, Song WY. Fast compressed sensing-based CBCT reconstruction using Barzilai-Borwein formulation for application to on-line IGRT. Medical physics 2012;39:1207-17..

The dissertation author was the primary researcher and the co-authors listed in this publication directed and supervised the research which forms the basis for this chapter.

Chapter 5 Fiducial marker motion based four dimensional (4D) CBCT and DTS

5.1 Introduction

The introduction of cone-beam computed tomography (CBCT) system in treatment settings has allowed implementation of various image guidance techniques for precise target localization [14, 18, 21, 60, 126]. With the help of CBCT system, the utilization of respiratory correlated four dimensional imaging schemes such as 4D CBCT and 4D digital tomosynthesis (DTS) for image guidance have become recently possible, and thereby it is possible to verify mobile internal organs and tumor target volume prior to the radiotherapy treatment [89, 127-129]. In fact, clinical adaptation of four dimensional CBCT for patient's lung stereotactic body radiation therapy (SBRT) treatment has started to be carried out very recently [130-132].

Besides the lung tumor cases, respiration induced intrafractional target motion is also particular concern in abdominal cancers such as liver [133, 134] and thereby verification process of its motion is necessary. However, since features of liver is not clearly visible in CBCT, it is difficult to assess and verify the breath induced motion prior to the treatment. Quite recently, fiducial markers inserted to or near tumor have been utilized for on-line imaging guidance using CBCT to improve precision of SBRT [135, 136] and thereby, opened the accessibility to asses movement of target tumor through four dimensional image guidance techniques.

On sorting the motion phases of cone-beam projection data for generating 4D reconstructed images, 5 types of acquiring patients' breath induced signal have previously

been demonstrated : using external gating system such as 1) thoracic belt containing a pressure sensor [137], 2) infrared reflector camera system [137, 138], 3) optical patient body surface measurement, and 4) gated acquisition of projection data [139], and direct method using 5) analysis on projection data [24]. Methods using external gating system and gated acquisition of projection data can be problematic since it could increase the complexity during patient setup and possible occurrence of error between signal and target motion [140, 141]. Method of analyzing projection data as an alternative, is suitable on calculating breathing phase, however, signal do not describe true diaphragm displacement [24] and therefore only phase wise sorting is achievable.

In this chapter, we will demonstrate the use of fiducial markers imaged at cone-beam projections to generate breath induced motion signal of liver for reconstructing 4D DTS as well as CBCT images. This method is advantageous to above types since the motion signal is extracted directly from markers inserted at internal organ near or at the tumor. In addition, measuring amplitude displacement of motion could be also achievable, which makes amplitude wise as well as phase wise sorting can be done selectively.

5.2 Imaging condition and patient data

A The projection data of liver cancer patient was acquired using On-Board Imager (OBI) CBCT system (Varian Medical Systems, Inc., Palo Alto, CA) which consists of a-Si flat panel detector and kV X-ray source mounted on a Varian 21EX Clinac. The flat panel detector consists of 1024×768 pixels with pixel size 0.388×0.388 mm per each.

The measured source to detector distance (SID) was approximately 150 cm with gantry rotation speed of 6 degrees per second which takes about 1 min for full gantry rotation.

Images were scanned with “Standard dose 150 cm bow tie” mode, where 651 projections data were acquired over 364° with 120 kVp, 80 mA and 25 ms for each projection. The FOV of both cases were 50×50 cm. Both projections were acquired with an aluminum bowtie filter placed directly under X-ray tube to compensate the large area projection geometry.

5.3 Extraction of fiducial marker position from CBCT imager

On extracting fiducial marker positions from each projection data of OBI, we have implemented feature extraction algorithm of marker which its shape and size is priory known. Since the fiducial markers are made up of gold, the contrast of fiducial marker is clearly distinctive in the projection data. The feature extraction algorithm consists of 5 steps: 1) sub-sample the region of interest (ROI) where fiducial markers are imaged in the projection data, 2) apply edge enhancement filter (canny edge operator) to highlight the feature of fiducial markers on the region which is extracted, 3) undergo fast Fourier transform (FFT) of highlighted region, multiply with the FFT signal of priory obtained ideal fiducial marker image, and then apply inverse FFT (convolution with ideal fiducial marker), 4) apply certain threshold value to the image to extract regions of fiducial markers, and finally 5) find the center of mass of each fiducial markers which are extracted from the image.

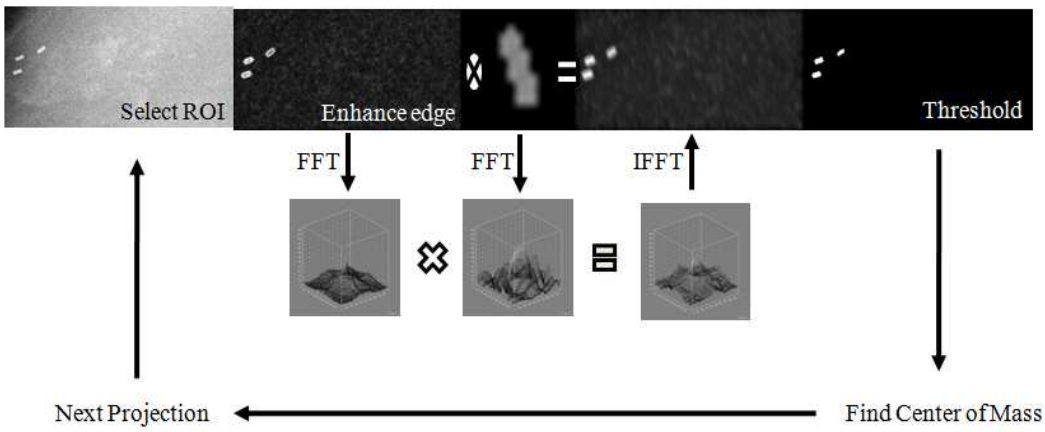

Fig. 5-1. General work flow of fiducial marker extraction algorithm.

The general work flow of fiducial marker extraction algorithm is illustrated in Figure 5-1. The reason for sub-sampling ROI where fiducial markers are present in the projection data at first step is due to the fact that the size of region where fiducial markers are distributed is small compare to the size of projection data and therefore, it is inefficient, less accurate and time consuming to find the markers by processing the feature extraction algorithm on whole projection image. If we could find the ROI where fiducial markers are present and process the feature extraction algorithm only on that sub-sampled region, it would be much accurate, efficient and faster. The ROI where fiducial markers are imaged in the projection data can be found by assigning a volume surrounding the fiducial markers in planning CT data, and forward projecting the assigned volume through CBCT projecting condition. Then the region of area in each projection data where forward projected volume intersects would be the ROI where fiducial markers are imaged. In the 2nd step, the edge enhancement filter applied on the sub-sampled image to optimally visualize the marker edges and feature of fiducial markers. As a edge enhancement filter, well known "canny edge operator" was used to enhance the edges. The canny edge operator uses a filter based on the first derivative of a

Gaussian filter kernel to reduce the noise of the image initially, followed by finding the intensity gradient of the image which corresponds to the edges. Thereby, only the edge of the feature can be enhanced without increasing noise component present in the image. The edge enhanced image where feature of fiducial marker is clearly visible, is then convolved with the priory obtained ideal fiducial marker image in order to boost up the pixel values of fiducial marker region. The convolution process was done with the use of FFT by simply multiplying Fourier transformed components of edge enhanced image and ideal fiducial marker image. Through multiplying the frequency component of ideal fiducial marker, pixel values which correspond to feature of fiducial marker in the image can be increased and become distinguishable from other regions. Finally, this region can be separated by applying threshold on the image and position of each fiducial marker can be extracted by calculating center of mass on each fiducial region.

In this study, we have implemented fiducial marker position extracting algorithm on MATLAB program. The volume surrounding the fiducial markers in planning CT was set as 5 cm^3 cube centered at -15 cm, 0, 0 from center of x, y and z axis respectively. The threshold was assigned as 80% value to the maximum pixel value of processing image after the convolution step, and center of mass on each fiducial marker was calculated by the use of CENTROID function provided by MATLAB.

5.4 Generation of breath induced marker motion signal

The breath induced marker motion signal can be generated by compiling the extracted position of fiducial markers for every cone-beam projections. However, certain angular region exists during patient scanning where fiducial markers are missing at the

projection data due to limited field of view (FOV) coverage of OBI at "half-fan" scanning mode geometry. Therefore, it is necessary to 1) select a signal from fiducial markers which has the least missing margin and 2) extract additional reference of breath induced signal to analyze and predict the angular margin where fiducial markers are missing in order to complete full breathing signal during patient scanning.

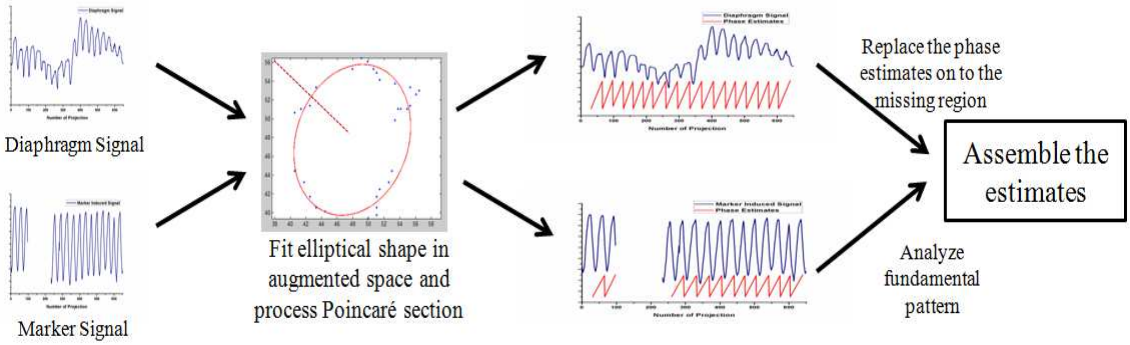

Fig. 5-2. Signal ‘‘profiling’’ of diaphragm and marker motion to predict signal at missing scan angular region.

In this study, we have predicted motion signal through ‘‘profiling’’ the diaphragm motion and marker motion signal. Ruan et al. [142] have introduced a real-time approach to systematically estimate baseline, frequency variation and fundamental pattern change of respiratory signal and predict the motion signal based on these observations. Prediction method through signal ‘profiling’ can be done in three stages : 1) phase estimation of missing region through tracking the fitted elliptical shape in augmented state space and Poincaré sectioning principle with diaphragm motion signal, 2) estimation of fundamental pattern through unwarping the actual marker motion signal at each state of phases. 3) assembling the estimates on to displacement signal space. The diaphragm motion signal was acquired from analyzing of projection data[24] (See Figure 5-2). As specified earlier, the motion signal from analyzing of projection data signal do not

describe true diaphragm displacement however, can be used as estimate of phase since phase pattern of respiratory motion is clearly distinguishable. The estimate of fundamental pattern at particular phase can be derived from mean average of existing marker motion signals at same phase by assuming that motion pattern of marker is stable.

Note that the purpose of replacing the missing signal was to complete the breath induced signal during patient scanning, and thereby preserving the overall quality of reconstructed images. Since information of fiducial markers are missing in projection data at the replacing margin, the image quality of region surrounding fiducial markers will never be affected no matter how much the replacement signal contains error with the actual motion.

5.5 Amplitude wise and phase wise sorting

The breath induced signal from extraction fiducial marker motion was then analyzed to process the phase wise sorting and amplitude wise sorting of acquired projection data. Through dividing the signal by separate respiratory periods, we have divided the projection data into four phases: peak-exhale phase, mid-inhale phase, peak-inhale phase, mid-exhale phase and four amplitudes: low amp, mid-low amp, mid-high amp and high amp. The reason for assigning less number of phases than 4DCT number of phases is due to insufficient number (~651) of projection data for a patient was available to be divided and reproduce tolerable image quality after the reconstruction.

In this study, 87.5% to 12.5% of phase length was assigned as peak-exhale phase, 12.5% to 37.5% of phase length as mid-inhale phase, 37.5% to 62.5% of phase length as peak-inhale phase and, 62.5% to 87.5% of phase length was assigned as mid-exhale

phase in terms of phase wise sorting. Similarly for amplitude wise sorting, 87.5% to 12.5% of signal height was assigned as low amp, 12.5% to 37.5% of signal height as mid-low amp, 37.5% to 62.5% of signal height as mid-high amp and, 62.5% to 87.5% of signal height was assigned as high amp.

5.6 4D CBCT and DTS reconstruction

For 4D CBCT, the reconstruction was done with well known FeldKamp (FDK) algorithm [19] which performs backprojection after filtration of projection data to reconstruct each sorted phase. The FDK algorithm was modified in order to suit the "half-fan" mode of cone-beam projection geometry. The resolution of voxel grid was set as 512 × 512 × 64 with a resolution of approximately 1.0 mm (LR) × 1.0 mm(AP)×2.5mm(CC).

On-board DTS are reconstructed by using subset of projection data which was acquired for CBCT using a FDK-type algorithm since the OBI system implemented for clinical use cannot support the imaging sequence of DTS. The theory of reconstructing DTS is almost the same as CBCT, except that DTS is created under limited angle projections whereas CBCT is reconstructed over all angle projections [21, 22, 99]. For reconstructing 4D DTS, projection data can be used from subsets of 4D projection datasets for reconstructing 4D CBCT. The total scan angle from "half-fan" mode was assigned as +90° ± 22.5° and -90° ± 22.5° from the rotation center. The resolution of voxel grid for 4D DTS was set as 512×512×64 with a resolution of approximately 1.0 mm (LR)×2.5 mm(AP)×1.0mm(CC). In terms of software, we have used C language for reconstruction process.

5.7 Results

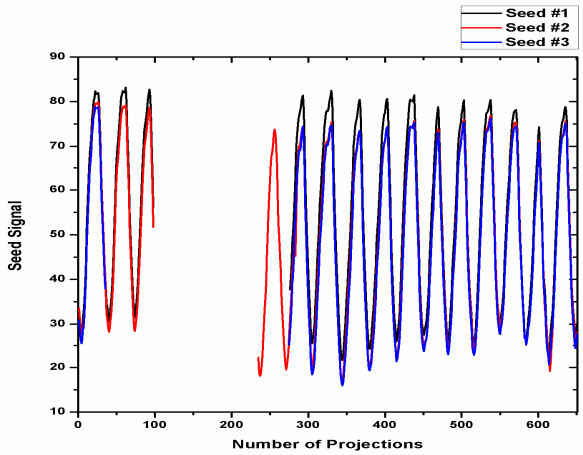

Fig. 5-3. Breath induced marker motion of three fiducial markers implanted on the patient.

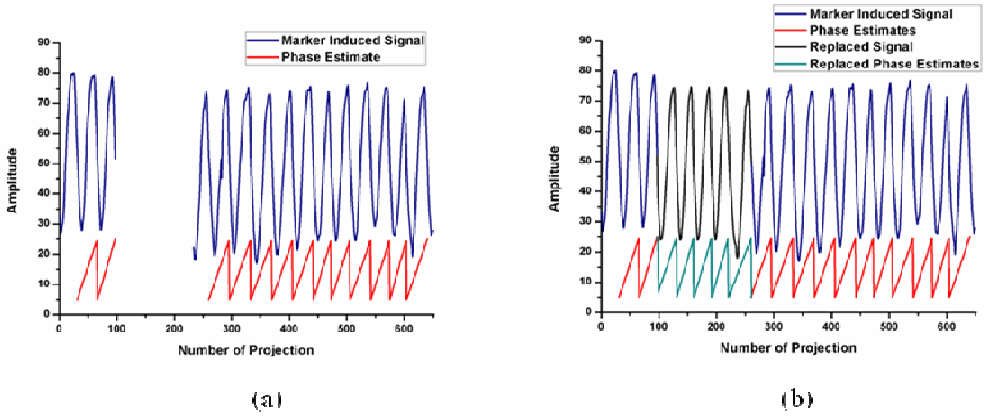

Fig. 5-4. Marker motion signal and its corresponding phase estimate through signal ‘‘profiling’’ prior (a) and after (b) the prediction.

Figure 5-3 shows the breath induced marker motion of three fiducial markers implanted on the patient. It is shown that no.2 fiducial marker has the least missing margin where marker starts to disappear from 99th projections to 234th projections which corresponds to approximately 67.5° degree. Figure 5-4 shows the marker motion signal and its corresponding phase estimate through signal ‘‘profiling’’ prior (a) and after (b) the prediction. It is clear that the joint of phase estimates between measured and predicted

region is smooth without major discontinuity. Moreover, it can be observed that the fundamental shape of marker motion signal has been restored after the prediction which makes overall signal likely natural. Figure 5-5 shows amplitude wise and phase wise reconstructed image of 4D CBCT (a) and DTS (b) at every state and corresponding 3D image. In comparison, motional artifact of fiducial marker (white arrow) is less in amplitude wise than phase wise reconstructed images due to lesser amount of residual motion at each state of sorting process.

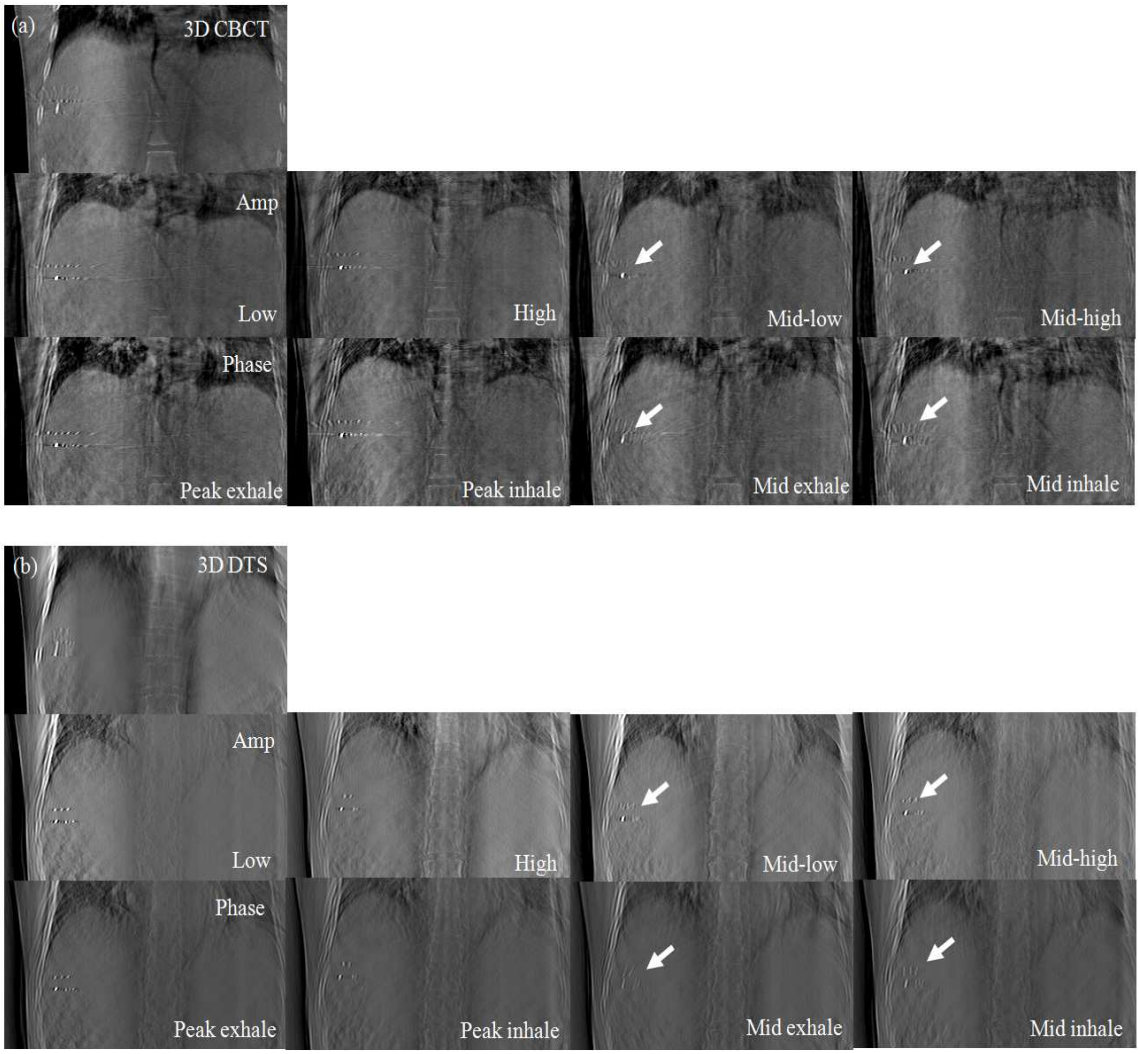

Fig. 5-5. Amplitude wise and phase wise reconstructed image of 4D CBCT (a) and DTS (b) at every state and corresponding 3D image.

5.8 Discussion and conclusion

In this study, we have demonstrated the use of fiducial markers imaged at CBCT projections to generate breath induced motion signal of liver to generate 4D DTS as well as CBCT images. The result showed that amplitude wise sorting showed less motional artifact than phase wise sorting. To the best of our knowledge, the motion of transcutaneously inserted metal markers has never been attempted for 4D sorting applications. Proposed method is advantageous compared to other methods in ways that 1) it does not require external gating system and 2) amplitude as well as phases wise sorting is selectively achievable.

Problem arises on certain angular region (18.5% of total scan) during patient scan where fiducial markers are missing at the projection data due to limited field of view (FOV) coverage of OBI at "half-fan" scanning mode geometry. However, we have shown that this missing region can be replaced by predicting the motion signal through ‘‘profiling’’ the diaphragm motion and marker motion signal. Besides using diaphragm signal to predict the period of missing region, the marker motion signal itself can be used as to predict the approximate length of the period. If the periodic variation of the signal is low, then average of periodic length can be used as the periodic length of missing region. Else wise, we can apply adaptive learning technique [142] to assign higher weights on recent observations to missing region if periodic patter of motion signal is substantially varying. This adaptive learning technique can also be applied to predict fundamental pattern change if the amplitude of signal is unstable. In this study, such variation was not observed and thereby simple mean of observations were used as predicted signal. These predictions may contain error with the actual signal, however, as specified in section 5.4.,

such replacement will not be problematic since information of fiducial markers are missing at the projection data in that angular region. Therefore, image quality of the region surrounding fiducial markers will never be affected no matter how much the predicted signal contains error after reconstruction process. Moreover, such problem can be handled if the patient is fully scanned with "spotlight mode" like as in prostate cancer.

All in all, we have shown the feasibility of motion tracking as well as 4D reconstruction of CBCT and DTS of liver through transcutaneously inserted metal markers and can be directed towards utilizing the technique for on-line image-guided adaptive radiotherapy.

5.9 Acknowledgements

The text of Chapter 5, in part or in full, is a reprint of the material as it appears in the following publication:

Park JC, Park SH, Kim JH, Yoon SM, Kim SS, Kim JS, Liu Z, Watkins WT, Song WY. Four-dimensional cone-beam computed tomography and digital tomosynthesis reconstructions using respiratory signals extracted from transcutaneously inserted metal markers for liver SBRT. Medical physics 2011;38:1028-36.

The dissertation author was the primary researcher and the co-authors listed in this publication directed and supervised the research which forms the basis for this chapter.

Chapter 6 Motion constrained image reconstruction (MCIR) for 4DCBCT reconstruction

6.1 Introduction

Image guided radiation therapy (IGRT) utilizing external imaging devices to verify position setup errors of patient just before/during treatment beam delivery is widely used in current radiation therapy setting [17, 143]. In particular, cone-beam computed tomography (CBCT) mounted on linear accelerators are most widely used imaging device in IGRT, due to its wealthy functional role in providing patient's (1) anatomic information [14, 18], (2) geometric information [58, 105] and (3) CT numbers for possible dose calculation and on-line/off-line re-optimization of plans. [62, 106] With aid of CBCT, implementation of various image guidance and adaptive radiotherapy techniques to enhance precision of treatment delivery become possible. [59-61, 126] Consequently, there is minimal doubt that CBCT has prominent role in current radiotherapy settings.

Image acquisition time of CBCT is long (≥1 min for thoracic/abdominal sites) due to limited speed of the linear accelerator gantry. [72-74] In addition, there are challenges in verifying the trajectory of mobile tumors caused by breathing. For example, when CBCT is applied to thorax, the image quality can be heavily degraded due to patient respiratory motion. Serious motion-induced artifacts compromise the effectiveness of using CBCT during IGRT. [144]

To overcome this problem, four-dimensional CBCT (4DCBCT) has been developed to provide respiratory phase-resolved volumetric images. [24, 137, 145-147]

In such an imaging modality, all the X-ray projections are first retrospectively grouped into different respiratory phase bins according to breathing signal tagged on every projection image. A CBCT image for each breathing phase is then reconstructed independently, yielding an image with much less motion-induced artifacts. The capability of 4DCBCT to significantly reduce the motion artifacts and enhance the target localization accuracy has been evaluated, allowing up to 50% reduction in planning target volume (PTV) size. [25, 148]

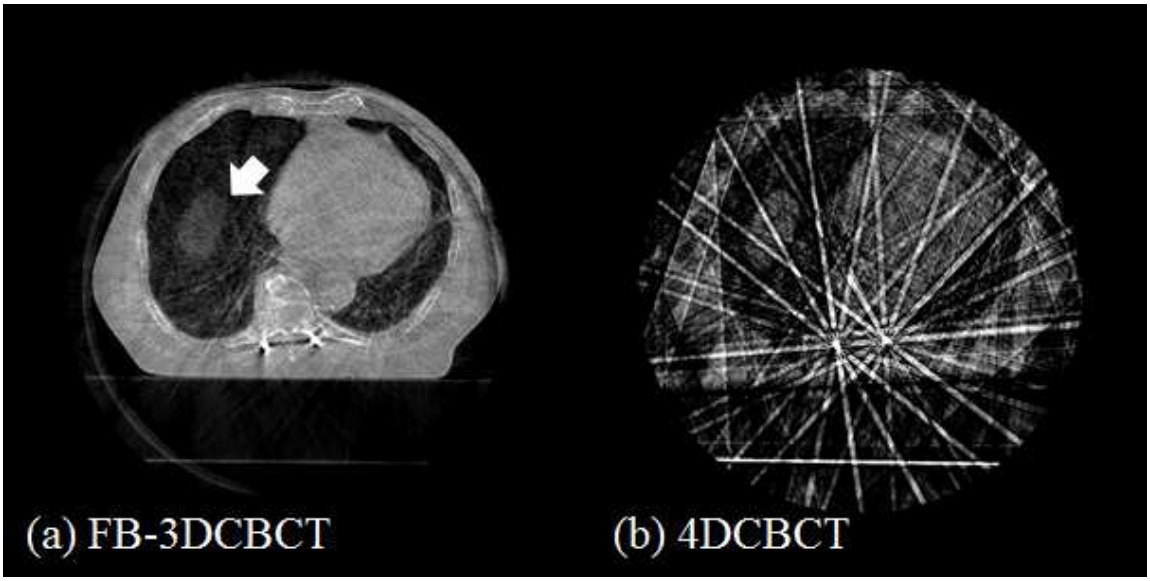

Fig. 6-1. Axial view of free-breathing 3DCBCT (FB-3DCBCT) (a) where all 647 X-ray projection data are used to reconstruct without considering breathing motion and 4DCBCT (b) where peak-inhale respiratory phase are grouped retrospectively, and only its corresponding phase (29 from 647 projections) are used to reconstruct the image. In FBCBCT, the diaphragm is blurred due to motion artifact (white arrow), and in 4DCBCT, severe streaking artifact exists due to inadequate number of projections to reconstruct the volumetric image.

Although 4DCBCT is capable of improving the motion artifacts and target localization accuracy, it poses another challenge for reconstruction. In fact, unless oversampling of X-ray projections are taken (which unavoidably increase the imaging dose by multiple folds[24, 25, 148]), the phase binning approach leads to insufficient number of X-ray projections in each respiratory phase bin and thus causes severe

streaking artifacts, when a standard 3DCBCT scanning protocol and reconstruction algorithm (FDK [19]) is applied (See Figure 6-1). This is also known as the under sampling artifact where the number of projections is insufficient to reconstruct a reasonable quality CBCT images.

In the past, many attempts have been made towards removing or relieving this problem. For example, scanning protocols of multiple gantry rotations and slow gantry rotations have been proposed to considerably increase the number of projections per phase. [146, 147, 149] In either case, reducing the mAs to avoid increasing the imaging dose to patients inevitably degrades image quality.

Advanced reconstruction techniques have also been proposed. For example, motion estimation and correction methods have been incorporated into the reconstruction.[150] It has also been proposed to split the reconstruction region according to a volume of interest and treat the reconstructions separately.[151] Meanwhile, a number of research efforts have been made on post-processing of the 4DCBCT images. For instance, a prior image-based approach [152] has been developed by first reconstructing a blurred CBCT image with all projections and then using it to estimate and remove the streaking artifacts. It has also been investigated to enhance the CBCT image by first deforming images at all phases into a single one and superimposing them together.[153, 154] The efficacy of these approaches, however, largely depends on the accuracy of the algorithms involved, such as deformable image registration algorithms. One of the most advanced approaches to date is the prior image constrained compressed sensing (PICCS) algorithm which can reconstruct high quality 4DCBCT without compromising imaging dose.[139] It first reconstructs a prior image by using all

projections and then reconstructs each phase image by regularizing both the total variation of the image itself and the total variation of the difference from the prior image.[108, 155, 156] Due to its high quality imaging performance and relative simplicity of the algorithm, PICCS has been evaluated in many different applications. [108, 155, 156]

In this study, we propose a novel 4DCBCT reconstruction algorithm called Motion-Map Constrained Image Reconstruction (MCIR) that utilizes a motion-map to achieve high-quality images from a highly under-sampled projection data. The MCIR algorithm allows 1) reconstruction of high quality 4DCBCT phase images with no more than the imaging dose used in a standard 3DCBCT scan, and 2) high phase resolution 4DCBCT sets with up to 20 phases using a typical patient's free-breathing 3DCBCT (FB-3DCBCT) scan. Comparison of our novel approach with the standard FDK and PICCS algorithms are presented in detail with numerical moving phantoms, and lung clinical patient data.

6.2 Review of 4DCBCT reconstruction

The common concept of CBCT reconstruction of all types (e.g. 3DCBCT and 4DCBCT) is to essentially solve the problem of finding unknown X-ray attenuation coefficients of image voxels from X-ray projections data measured from various gantry angles. In 4DCBCT, the first step in reconstruction is to group the X-ray projections into various respiratory phase bins (e.g. 10 phases) according to breathing phase tagged to each projection image. In the next step, a set of 3DCBCT for each breathing phase is then reconstructed from the sorted projections to constitute a 4DCBCT. One thing to note here

is that when a particular 4DCBCT phase image is reconstructed, substantial amount of projection data that are not within the phase window is discarded after the sorting process. Under such circumstance, projection data that are left to solve the unknown 4DCBCT phase voxels are then often insufficient to allow high quality image reconstruction. The main contribution of the proposed MCIR algorithm is to address this issue by intelligently differentiating the moving voxels in the volumetric image from the stationary ones.

6.3 MCIR algorithm

The key intuition of the MCIR algorithm lies in the observation that when a patient exhibits respiratory motion, not all parts of the patient's anatomy are in motion. Figure 6-2 illustrates this point. Tissues that are inside the lungs (e.g. tumor) move significantly, whereas outside are nearly stationary (e.g. bones, muscles, etc.). Suppose we can distinguish voxels between ones that are moving and stationary via what we call a "motion-map", then a series of 4DCBCT images can be reconstructed by updating FB-3DCBCT only those voxels that are moving according to a corresponding phase, and keeping voxels constant for those voxels that are stationary.

Fig. 6-2. 4DCT image of lung cancer patient at (a) peak inhale 0% phase and (b) exhale 50% phase. Using the dotted white line as reference, the lung tumor inside the right lobe exhibits significant up/down motion, while the bones and surrounding muscle tissues are relatively stationary.

The main advantage of such approach is that since the number of *mobile* voxels to be reconstructed in each phase is less than the total voxels in 3D image, the overall

unknowns in each phase is now smaller. Therefore, there are more projection data to reconstruct a higher quality phase images than if such information wasn't utilized.

In this chapter, the matrices are denoted as a boldface-uppercase letters and the vectors are denoted as a boldface-lowercase letters. In the MCIR algorithm, we represent the unknown 4DCBCT phase volume as:

$$\boldsymbol{x}_{phase} = \boldsymbol{x}_{3D} + \boldsymbol{U}^{1/2}\boldsymbol{k}_{phase} \tag{6.1}$$

where $\boldsymbol{x}_{phase}$ = unknown 4DCBCT phase volume, $\boldsymbol{x}_{3D}$ = a priori reconstructed FB-3DCBCT volume (using any conventional algorithm including FDK[19] and SART[157]), $\boldsymbol{U}$ = diagonal motion-map matrix and $\boldsymbol{k}_{phase}$ = phase-specific update vector.

Equation (6.1) demonstrates that our approach is to start from the FD-3DCBCT image and then identify the phase specific motion information by referring to the motion-map matrix $\boldsymbol{U}$. The diagonal motion-map matrix $\boldsymbol{U}$, which represents the weighting factors associated with all voxels is defined mathematically as follows:

$$\boldsymbol{U} = diag\{a_1, a_2, a_3, ...a_M\} \quad \text{where, } M = \text{volume dimension, and } a_i = [0,1] \tag{6.2}$$

Here, a_i corresponds to the *i-th* diagonal element of motion-map matrix $\boldsymbol{U}$, where the value ranges between 0 to 1 and a_i would be close to 1 when the voxel value varies largely with respiratory motion and close to 0 when voxel value varies minimally with breathing. The main reason for adding square root term on $\boldsymbol{U}$ in Equation (6.1) is to simplify the updating equation for solving $\boldsymbol{x}_{phase}$, which we will show shortly.

Remember that in 4DCBCT reconstruction, projection data that are available for each phase is limited in number due to the sorting process. Therefore, it is important to select reconstruction model that appropriately handles such circumstance to give you an adequate image. Recent studies have shown that compressed sensing type of CBCT

reconstruction based on total variation formulation has shown that efficient reconstruction can be performed with limited number of projections.[33, 107, 108, 110, 158, 159] Thus, utilizing this theory, keeping 4DCBCT volume $\boldsymbol{x}_{phase}$ as unknown, the mathematical model for the MCIR algorithm is setup to solve the constrained convex optimization of the form:

$$\min_{\boldsymbol{x}_{phase}} f(\boldsymbol{x}_{phase}) = \left\| \boldsymbol{A}_{phase}\boldsymbol{x}_{phase} - \boldsymbol{b}_{phase} \right\|_2^2 + \lambda TV(\boldsymbol{x}_{phase}) \quad s.t. \quad \boldsymbol{x}_{phase} \geq 0 \tag{6.3}$$

where $\boldsymbol{A}_{phase}$ = Radon transform operator at a specific phase, $\boldsymbol{b}_{phase}$ = phase sorted projection data, λ = regularization constant, and $TV(\cdot)$ = Total Variation (TV) regularization term. The TV term we used in this study is defined as:

$$TV\left(\boldsymbol{x}(i,j,k)\right) = \sqrt{\begin{aligned}&[\boldsymbol{x}(i+1,j,k) - \boldsymbol{x}(i,j,k)]^2 + \\ &[\boldsymbol{x}(i,j+1,k) - \boldsymbol{x}(i,j,k)]^2 + \\ &[\boldsymbol{x}(i,j,k+1) - \boldsymbol{x}(i,j,k)]^2\end{aligned}} \tag{6.4}$$

where i, j and k corresponds to Left-Right (LR), Anterior-Posterior (AP) and Cranial-Caudal (CC) coordinates in 3D volume space, respectively. Here, elements of vector x are indexed by 3D coordinates for notational simplicity. In this form, the first term in Equation (6.3) is the fidelity term, which enforces fidelity of $\boldsymbol{x}_{phase}$ with the sorted projection data. The second term (the regularization term) promotes sparsity inherent in the X-ray attenuation characteristics of the human body.

In Equation (6.1), we have defined the 4DCBCT phase volume $\boldsymbol{x}_{phase}$ as a combination of FB-3DCBCT with the phase-specific update vector $\boldsymbol{k}_{phase}$ that is weighted by the motion-map matrix $\boldsymbol{U}$. The FB-3DCBCT, $\boldsymbol{x}_{3D}$, can be easily computed using all available projections. Assuming that we already know the value of motion-map matrix $\boldsymbol{U}$,

which we will discuss in section 6.4, we can calculate to solve Equation (6.3). This is done by substituting Equation (6.1) into (6.3) and calculating the gradient of the right hand side of Equation (6.3) with respect to $\boldsymbol{k}_{phase}$, which then becomes:

$$\boldsymbol{x}_{phase}^{n+1} = \boldsymbol{x}_{phase}^{n} + \alpha \boldsymbol{U}[2\boldsymbol{A}_{phase}^{\boldsymbol{T}}(\boldsymbol{A}_{phase}\boldsymbol{x}_{phase}^{n} - \boldsymbol{b}_{phase}) + \lambda\nabla\,(TV(\boldsymbol{x}_{phase}^{n}))] \tag{6.5}$$

where n = number of iterations, α = gradient step size, $\boldsymbol{A}^{T}_{phase}$ = back-projection matrix of sorted ∇ projections and = gradient operator. Note here that by modeling $\boldsymbol{x}_{phase}$ with square root term of $\boldsymbol{U}$ (Equation (6.1)), the updating equation simplifies to multiplying $\boldsymbol{U}$, instead of its square.

In Equation (6.5), we can notice that the gradient (second term) of Equation (6.3) with respect to $\boldsymbol{k}_{phase}$ becomes the product of motion-map matrix $\boldsymbol{U}$ with the original gradient of TV based CBCT reconstruction algorithm[159] (i.e. gradient of Equation (6.3) with respect to $\boldsymbol{x}_{phase}$). As a result, the update energy will mainly be imparted on the voxels with the associated weight factor a_i closer to 1 while spending little energy to update the voxels with values close to 0. Those voxels having weight a_i=0 in $\boldsymbol{U}$ will preserve the voxel value in the FD-3DCBCT, $\boldsymbol{x}_{3D.}$

6.4 Motion-map calculation

In the previous section, we have mathematically formulated the updating equation of MCIR algorithm (Equation (6.5)) to minimize the cost function given by Equation (6.3). As you can imagine, calculating the motion-map $\boldsymbol{U}$ is a critical step in implementing Equation (6.5). The effectiveness of the MCIR algorithm is largely dependent upon how well the motion-map represents the mobile anatomy.

There can be a number of ways to calculate the motion-map of a patient. One intuitive way is to utilize a planning 4DCT dataset via calculation of deformable motion vectors. However, this approach may not be very useful since the patient posture must be very close, if not identical, between the 4DCT and at the time of treatment. In addition, considerable motion-to-motion variation on daily basis [160] as well as with registration uncertainty [161] exists which may hamper the precision of the motion-map.

In this study, we have developed a novel and effective method that obtains the motion-map directly from the projection data obtained at the time of the CBCT scan. In this way, no external prior-knowledge information is needed to obtain the motion map. The idea behind this concept is that when the FB-3DCBCT is reconstructed, the regions that are subject to varying degrees of respiratory motion would contain larger data inconsistency (i.e. motion artifact) compared to the regions that are stationary. Intuitively, if we can incorporate such information and reconstruct with an effective strategy, a precise motion-map matrix $\boldsymbol{U}$ can be calculated. This is our intuition, which led to the following.

To calculate the motion-map matrix $\boldsymbol{U}$, first, the FB-3DCBCT is reconstructed using all of the projections. For this, any reconstruction method can be used (e.g. FDK[19] or compressed sensing type algorithms). In this study, we have used the FDK approach for its computational efficiency compared to other iterative reconstruction techniques. Second, for each phase, the FB-3DCBCT is updated with the phase-wise sorted projection data while minimizing 1-norm difference from the reconstructed FB-3DCBCT as a regularization term. Third, sub-motion-error vector for each phase denoted by $\boldsymbol{u}_{phase}$ is calculated by taking the difference between the updated FB-3DCBCT with the

original FB-3DCBCT. Mathematically, the sub-motion-error vector can be represented as:

$$\boldsymbol{u}_{phase} = \boldsymbol{x}_{3D} - \boldsymbol{x}^{*}_{Phase} \tag{6.6}$$

where

$$\boldsymbol{x}^{*}_{Phase} = \arg\min\{\left\|\boldsymbol{A}\boldsymbol{x}_{Phase} - \boldsymbol{b}_{phase}\right\|_2^2 + \eta\left\|\boldsymbol{x}_{3D} - \boldsymbol{x}_{Phase}\right\|_1\} \quad s.t. \quad \boldsymbol{x}_{Phase} \geq 0 \tag{6.7}$$

Here, $\boldsymbol{x}_{phase}$ = updated FB-3DCBCT with phase-wise sorted projection data with 1-norm constraint, $\boldsymbol{x}_{3D}$ = a priori reconstructed FB-3DCBCT volume, and η = regularization constant for 1-norm term. In Equation (6.7), we can notice that the original FB-3DCBCT, $\boldsymbol{x}_{3D}$, is being updated with phase information, $\boldsymbol{x}^{*}_{Phase}$, while promoting sparsity in the difference between the original FB-3DCBCT and the updated value, $\boldsymbol{x}_{Phase}$. In this way, we can rigorously update the original FB-3DCBCT with phase information in the sections that contain motion-induced data inconsistency while keeping the consistent regions with values from the original FB-3DCBCT. Then, by taking the difference between FB-3DCBCT and $\boldsymbol{x}^{*}_{Phase}$, sub-motion-error vector can be calculated representing motion-errors corresponding to each phase. Finally, when sub-motion-error vector has been calculated for all phases, we can calculate a normalized motion-map matrix $\boldsymbol{U} = diag\{a_1, a_2, \ldots, a_M\}$ defined as:

$$a_i = \sum_{phase=1}^{N}\left|u_{phase}(i)\right| / \max_i\{\sum_{phase=1}^{N}\left|u_{phase}(i)\right|\} \tag{6.8}$$

where N = total number of phase bins that are sorted. Figure 6-3 illustrates the process of obtaining $\boldsymbol{U}$ in the MCIR algorithm. It can be seen that a large portion of $\boldsymbol{U}$ exhibits very low values (closer to 0) except the regions that contain motion.

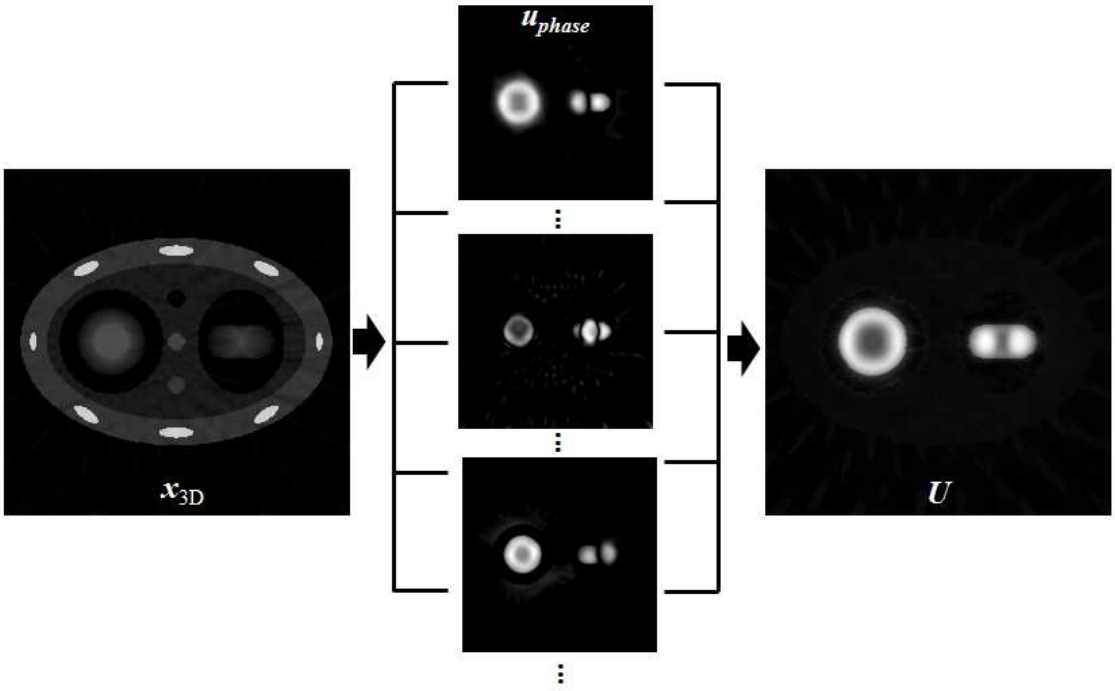

Fig. 6-3. Illustration of generating a motion-map, U. First, $\boldsymbol{x}_{\text{FB-3DCBCT}}$ is reconstructed using a conventional algorithm (e.g., FDK). Second, sub-motion-error vector for each phase ($\boldsymbol{u}_{phase}$) is calculated by taking the difference between updated FB-3DCBCT with FB-3DCBCT. Finally, motion-map matrix $\boldsymbol{U}$ is calculated by normalizing absolute sum of sub-motion-error vector $\boldsymbol{u}_{phase}$ at all phases. As can be seen, image U exhibits very low values (dark ~0), except near the diaphragm and lung (white ~1).

Solving Equation (6.7) for all phases could be time-consuming. It turns out that approximately solving the problems with only a few iterations provides enough information for generating the desired motion-map. As a result, the motion-map can be generated with much less computations compared to the computation required for reconstructing the phase-specific images, indicating that the overall overhead for generating the motion-map is small.

6.5 Practical implementation of MCIR

After the motion-map $\boldsymbol{U}$ is generated, Equation (6.5) has all of the necessary data to iteratively search for the best solution, for each 4DCBCT phase, with the original FB-

3DCBCT as the starting volume. The MCIR algorithm pseudo code is shown in Figure 6-4. The process is as follows. First, FB-3DCBCT is reconstructed with the FDK algorithm using all X-ray projections that were obtained. Second, FB-3DCBCT is updated with phase-wise sorted projections such that regions containing the motion induced data inconsistency are updated with the phase information while enforcing consistency on motion-free regions with the original values from the FB-3DCBCT. The updated volume is subtracted with the original FB-3DCBCT to generate sub-motion-error vector, $\boldsymbol{u}$, at each phase. Third, the absolute values of the sub-motion-error matrices are element-wise added and normalized to the maximum values to obtain the motion-map matrix $\boldsymbol{U}$. Finally, for all phases, the MCIR is performed by initializing all voxels as the original FB-3DCBCT and updating the values according to Equation (6.5), at each iterative step.

Step 1: Input Projection data $\boldsymbol{b}_{All\,phase}$
Step 2: Process FDK with $\boldsymbol{b}_{All\,phase}$ and set $\boldsymbol{x}_{3D} = \boldsymbol{x}_{FDK}$
Step 3: For each phase calculate sub-motion-error matrix $\boldsymbol{u}_{phase}$
  Step 3-1: Set $\boldsymbol{x}^{0}_{phase} = \boldsymbol{x}_{3D}$ and select $\boldsymbol{b}_{phase}$
  Step 3-2: Iterate $\boldsymbol{x}^{n+1}_{phase} = \boldsymbol{x}^{n}_{phase} + \alpha[2\boldsymbol{A}^{T}_{phase}(\boldsymbol{A}_{phase}\boldsymbol{x}^{n}_{phase} - \boldsymbol{b}_{phase}) + \eta sign(\boldsymbol{x}_{3D} - \boldsymbol{x}^{n}_{phase})]$
  Step 3-3: Calculate $\boldsymbol{u}_{phase} = \boldsymbol{x}^{*}_{phase} - \boldsymbol{x}_{3D}$
Step 4: Set $\boldsymbol{U}$ according to Equation (6.7)
Step 5: For each phase process MCIR
  Step 5-1: Set $\boldsymbol{x}^{0}_{phase} = \boldsymbol{x}_{3D}$ and select $\boldsymbol{b}_{phase}$
  Step 5-2: Iterate $\boldsymbol{x}^{n+1}_{phase} = \boldsymbol{x}^{n}_{phase} + \alpha\boldsymbol{U}[2\boldsymbol{A}^{T}_{phase}(\boldsymbol{A}_{phase}\boldsymbol{x}^{n}_{phase} - \boldsymbol{b}_{phase}) + \lambda\nabla TV(\boldsymbol{x}^{n}_{phase})]$

Fig. 6-4. The flow of MCIR algorithm for 4DCBCT reconstruction at each phase. Note here that the second term of the equation in step 3-2 is first-order gradient of Equation (6.7).

As can be noticed, the MCIR algorithm is an iterative process, which is computationally heavy, taking hours of CPU time to reach the solution. Efficiently solving this would require (1) parallel programming with proper hardware, and (2) deriving a mathematical formulation to achieve fast-solution-convergence. To handle the

former issue, we have parallelized our code with the graphics processing unit (GPU) in the CUDA C/C++ programming environment. In this way, major computational tasks such as (1) forward projection, (2) back projection, and (3) vector as well as filter operations can be efficiently parallelized [32, 115, 162]. For the latter issue, we have used our recently published gradient projection algorithm based on the Barziliai-Borwein (GP-BB) formulation that can handle compressed sensing type of CBCT reconstruction based on total variation formulation in extremely efficient manner. [118, 159]

6.6 Numerical simulations and patient data

To evaluate the performance of our proposed MCIR algorithm, we have tested on both numerical phantom and lung cancer patients, with the X-ray projections obtained from the TrueBeam™ system (Varian Medical Systems, Palo Alto, CA). The results were then compared with the (1) clinical FD-3DCBCT reconstructed from the OBI™ (FDK), (2) 4DCBCT reconstructed with FDK, and (3) 4DCBCT reconstructed using PICCS, a best known 4DCBCT algorithm to date. For the numerical phantom study, we have used a dynamic chest phantom similar to those used in previous 4DCBCT related studies.[152, 163] It is a numerical phantom that emulates respiratory motion with two circular objects deforming expand-shrink and moving left-right. (See Figure 6-5) We first set the breathing period to 5 seconds with a cosine function and acquired 600 simulated projections over one minute of full gantry rotation. We then divided and sorted the projections into even 40 phases. This means, on average 15 projections were used to reconstruct each phase.

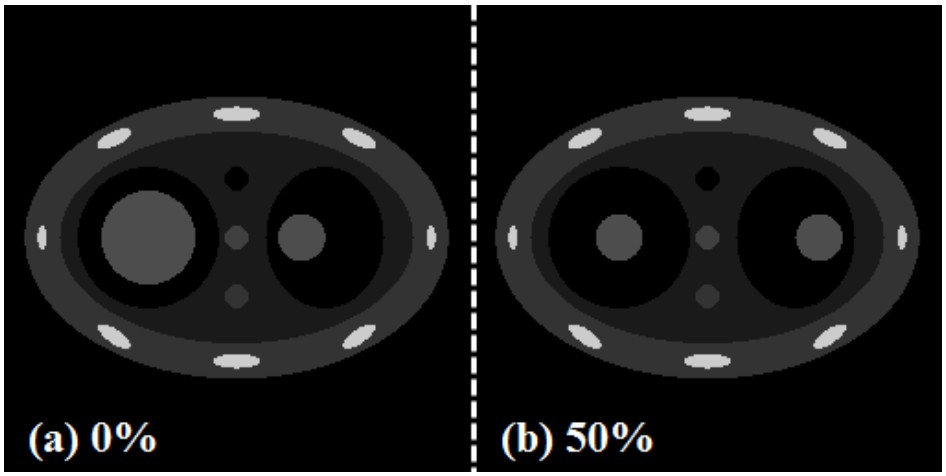

Fig. 6-5. Physical moving phantom at peak inhale 0% and exhale 50% used in our numerical simulation. Two circular objects located left and right parts are set to deform expand-shrink and move left-right.

For the clinical lung cancer patient case, a total of 674 projections were acquired over one minute gantry rotation, in a half-fan scanning geometry, representing a typical FB-3DCBCT clinical scan. The imager has 1024 × 768 pixels with 0.388 × 0.388 mm^2 resolution. This was down-sampled to 512 × 384 pixels with 0.776 × 0.776 mm^2 for the reconstructions. During the acquisition, each projection data was tagged with the phase information from the RPM^{TM} system. Using this information, we divided and sorted the projections into 20 phases. On average, about 34 projections were assigned to each phase. The 4DCBCT volumes were reconstructed with 512 × 512 × 70 voxels at the resolution level of 0.97 × 0.97 × 2.0 mm^3.

6.7 Results

Figure 6-6 shows a numerical 4D phantom simulation results including the ground truth images at two phases 0 and 50%, 4DCBCT reconstructed using FDK, 4DCBCT reconstructed using CS, 4DCBCT reconstructed using PICCS, and 4DCBCT reconstructed using our MCIR algorithm. In order to ensure that the images for all

iterative algorithms (CS, PICCS, and MCIR) to reach as close to its convergence, we have run 1000 iterations for all with the same GP-BB step-size approach. [118, 164] Since the MCIR algorithm starts with a FB-3DCBCT as an initial input, we have kept all initial input as FB-3DCBCT for the CS and PICCS algorithms as well. As is expected, severe streaking artifacts appear in the 4DCBCT reconstructed using the FDK algorithm (Fig.6-6 (b), (g)). Visually, many of the structures in the medial aspect of the phantom are nearly indistinguishable. 4DCBCT using the CS algorithm (Fig.6-6 (c), (h)) significantly mitigates such artifact, as expected. However, it is still evident that anatomical structures are blurred due to some patching artifact (i.e., dark-gray streaks). As for PICCS and MCIR, there are noticeable improvements in image quality from the CS (Fig.6-6 (d), (i)) (e.g, reduced patching artifact). Visually, the image quality seems nearly equivalent to each other. By taking a closer look, however, we see that the boundary of the moving balls in either side of the phantom is slightly sharper in the MCIR algorithm. Figure 6-7 show measured line profiles across the left ball in the phantom, for a 50% phase image. The line profile of the MCIR algorithm follows closest to the ground truth (see expanded view in the subset). In digging deeper, we have calculated the root mean square error (RMSE) for all 40 phase images, which is illustrated in Figure 6-8. Here, the RMSE is defined as the root of mean-squared percent error from the ground truth pixel values:

$$\mathrm{RMSE}(\%)=\sqrt{\frac{\sum_{i,j,k}(\boldsymbol{x}_{i,j,k}-\boldsymbol{x}_{i,j,k}^{GroundTruth})^2}{\sum_{i,j,k}(\boldsymbol{x}_{i,j,k}^{GroundTruth})^2}}\times 100 \tag{6.9}$$

where, $\boldsymbol{x}_{i,j,k}$ correspond to the voxel values in the reconstructed volume $\boldsymbol{x}$ and $\boldsymbol{x}^{GroundTruth}$ refers to the ground truth values of the numerical chest phantom that we used in this

study. It is clear from the figure that the level of agreement to the ground truth is in the order of MCIR > PICCS > CS > FDK, for all phases. The FDK algorithm had the largest RMSE of 42.6±6.5% ranging from 33.7%-61.2%. The CS algorithm performed much better than FDK, which had RMSE of 0.87±0.13% ranging from 0.65%-1.14%. The RMSE for PICCS varied from 0.47%-0.78% with an average of 0.58%±0.08%. Finally, the MCIR algorithm showed the best performance with 0.44% ± 0.04% ranged from 0.37%-0.52%. This finding holds true at all levels of iterations as well, as shown in Figure 6-9, where RMSE was calculated at each iterative step. As can be seen from the figure, the MCIR algorithm needs less than 100 iterations to achieve RMSE < 1% from the ground truth, whereas the CS or PICCS need many more iterations to reach that level. This is mainly due to the fact that, unlike other algorithms, the update energy is mainly focused on the *mobile* voxels in our MCIR algorithm. This suggests that the MCIR algorithm outperforms the CS and PICCS, in terms of image quality but, the speed of algorithm to reach the optimum solution is also faster.

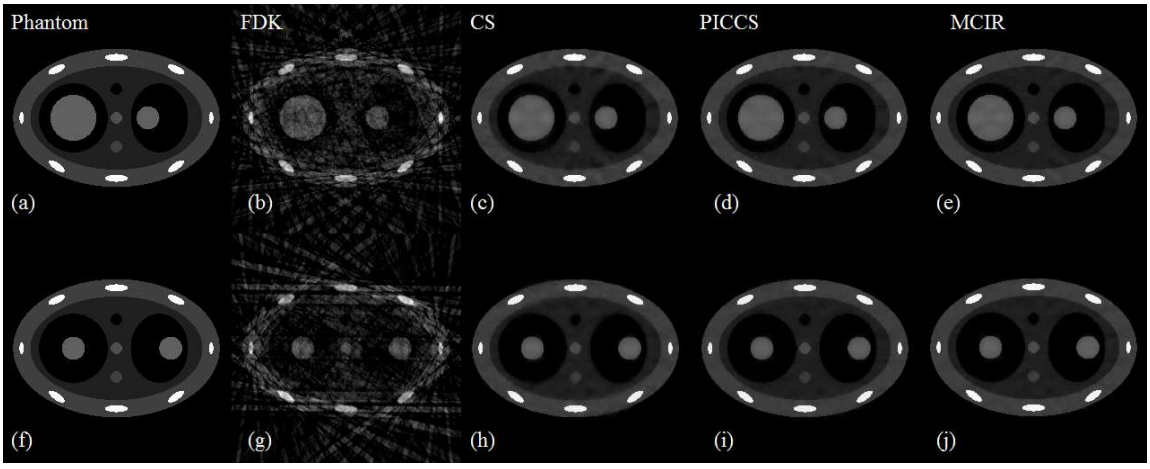

Fig. 6-6. A numerical 4D phantom simulation results. (a),(f) ground truth phantom image at two phases 0 and 50%. (b),(g) 4DCBCT reconstructed using FDK. (c),(h) 4DCBCT reconstructed using CS. (d),(i) 4DCBCT reconstructed using PICCS. (e),(j) 4DCBCT reconstructed using our MCIR algorithm.

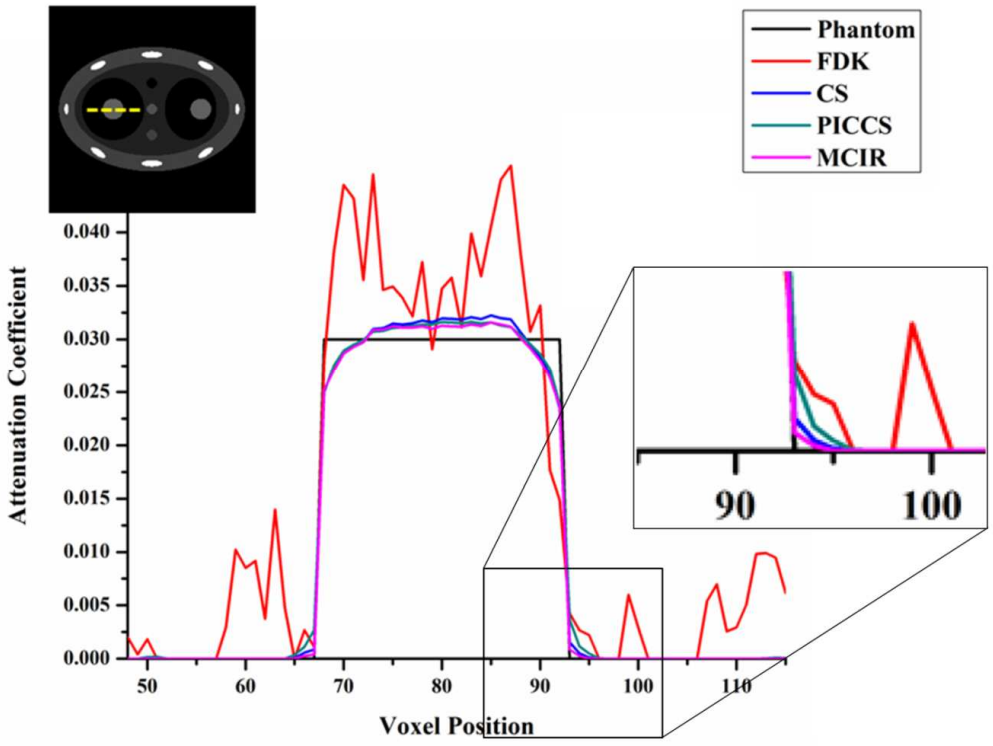

Fig. 6-7. Measured line profile of moving object of phantom at 50% phase. Position of measured line is illustrated by yellow dotted line inside the phantom image.

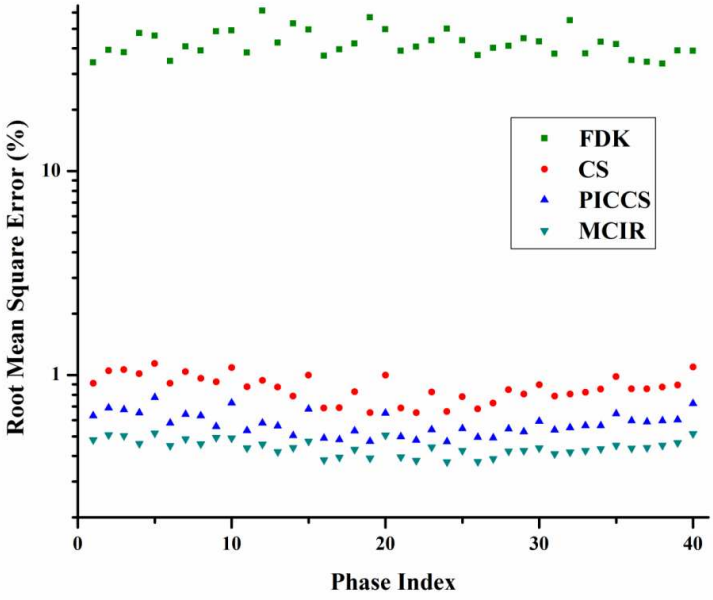

Fig. 6-8. Comparison of root mean square error (RMSE) between 4DCBCT reconstructed using FDK, CS, PICCS and our MCIR across all phases.

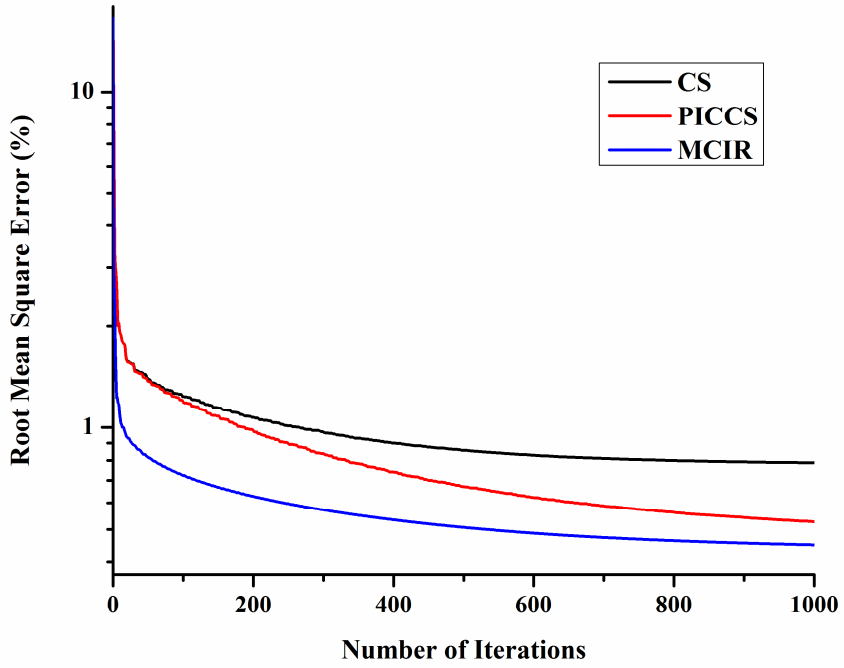

Fig. 6-9. Variation of RMSE measured over each iteration during 4DCBCT reconstruction of 0% phase phantom for CS, PICCS and our MCIR algorithm. Note that FDK is discarded from comparison since it is not iterative reconstruction procedure.

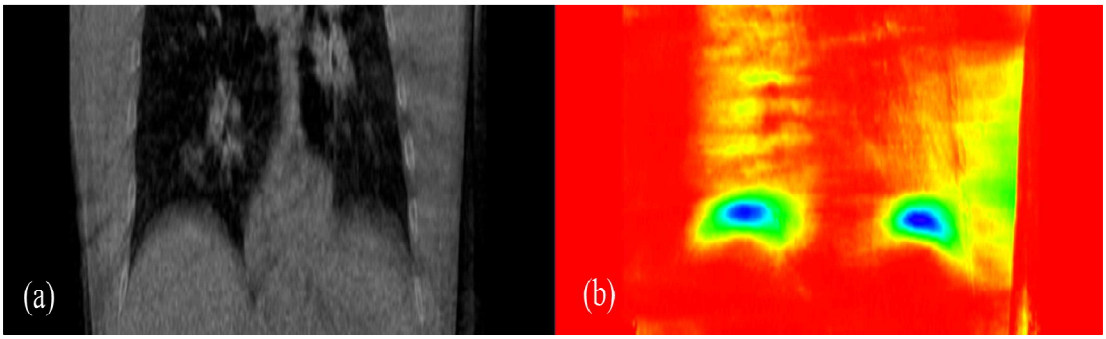

Fig. 6-10. Coronal slice of FB-3DCBCT reconstructed using clinical lung cancer patient data (a) and its corresponding motion-map using proposed motion-map reconstruction approach (b). The motion-map intensity is highest across diaphragm is the highest (blue) which is true when patient is breathing.

Figure 6-10 shows a coronal slice of FB-3DCBCT reconstructed using a clinical lung cancer patient data and its corresponding motion-map generated using the proposed motion-map reconstruction approach (in color scale from 0 to 1). As we expect from our

clinical experience regarding thoracic anatomy, the motion-map intensity should be and is the highest around the diaphragms. It is also evident that the motion-map inside the lungs has varying degrees of intensity as well, which is also expected. One undesirable result, though, is that there is also some intensity in the soft tissue on the left side of the patient. This is due to the fact that the field of view (FOV) in our CBCT scanner is not enough to cover all of the patient's anatomy and, therefore, a truncation error would accumulate when the motion-map is generated. However, this is not an issue of concern as long as the motion-map captures all of the relevant part of the anatomy that are moving, which we absolutely need to visualize for 4D IGRT applications. That is, since the motion-map is a weighting vector that updates the initial FB-3DCBCT with phase-wise sorted projections that have already been used to reconstruct the FB-3DCBCT, updating the non-mobile regions with the phase-wise sorted projections would be really minimal, so there won't be much change in that region anyway.

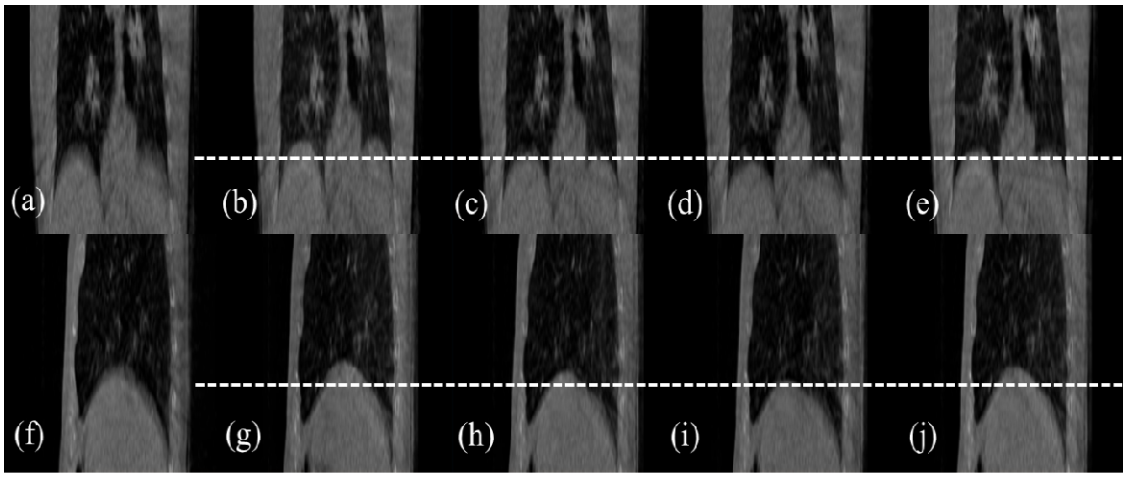

Fig. 6-11. Coronal and Sagittal slice of clinical lung cancer patient of FB-3DCBCT (a),(f), and our proposed MCIR algorithm at 0% phase (b), (g), 25% phase (c),(h), 50% phase (d),(i) and 75% phase (e),(j). The image qualities of MCIR at all phases are almost equivalent to image quality of FB-3DCBCT and well represent the respiratory motion (See diaphragm).

Figure 6-11 shows coronal and sagittal slices of the lung cancer patient with the FB-3DCBCT, and the MCIR algorithm at 0%-peak-exhale, 25%-mid-inhale, 50%-peak-inhale, and 75%-mid-exhale. It is clear that the MCIR's image quality, at all phases, are almost equivalent to that of FB-3DCBCT, in terms of low contrast and noise, but moreover, the diaphragm positions are clearly distinctive. This confirms that although only 34 projections were used to reconstruct each phase, our MCIR algorithm can reconstruct all 20 phases of the breathing curve without the agitating streak artifacts that are caused by insufficient projections.

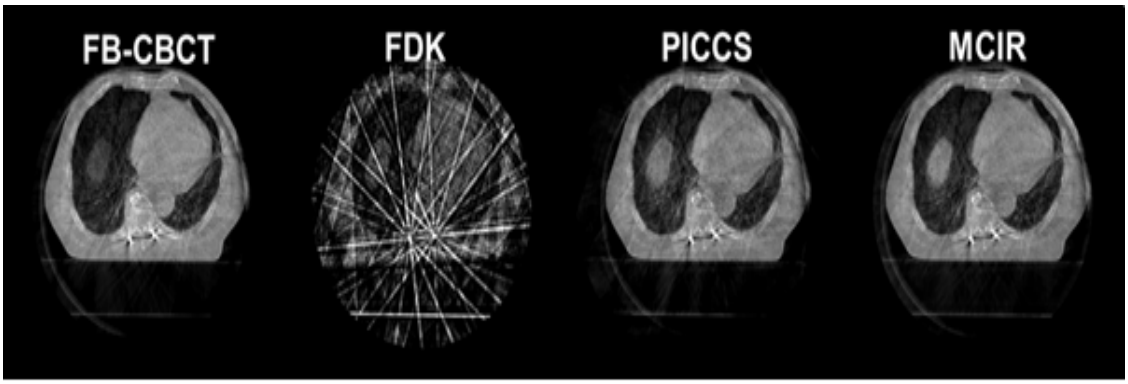

Fig. 6-12. A lung cancer patient results of FB-3DCBCT, 4D-FDK, MCIR and PICCS algorithm.

Finally, Figure 6-12 displays the lung cancer patient's 4DCBCT (50% phase) reconstructed with the FB-3DCBCT (using FDK), 4D-FDK, MCIR, and PICCS algorithms. As expected, severe streaking artifact exists in the 4D-FDK. In contrast, both the MCIR and PICCS algorithms significantly outperform that of the 4D-FDK. In closer visual inspection, it is also observed that the streaking artifact is relatively further reduced in the MCIR as compared to the PICCS result. As an example, the diaphragm boundary show reduced streaks.

6.8 Discussion

A. Algorithm performance

In the evolution of lung cancer IGRT, transitioning from FB-3DCBCT to 4DCBCT is essential due to the fact that the extent of tumor motion is the key information in maximizing target localization accuracy. [24, 145, 165-167] With the use of conventional FDK reconstruction algorithm, the only way to achieve this is to increase the scanning time to acquire more projections, which inevitably increases the radiation exposure to patients.

In this study, we proposed a novel 4DCBCT reconstruction approach called the MCIR, and have successfully shown that at least up to 20 high quality phase images can be reconstructed using the same input dataset as a single clinical CBCT scan, without increasing the imaging dose.

The main innovation comes from recognizing that when a thoracic anatomy is subjected to respiratory motion, not all parts of the anatomy are significantly moving. Therefore, if we could somehow distinguish between the regions that are moving more and less, we could reconstruct a high quality 4DCBCT by updating the voxels with significant motion using the corresponding phase sorted projections while keeping the voxels that don't move from the FB-3DCBCT data.

The results both in numerical simulation as well as a patient data showed that the MCIR algorithm outperforms many other popular-and-advanced algorithms such as the CS and PICCS. It should be noted though, however, that the implementation of the CS and PICCS may not have been exactly reproduced as the ones originally proposed and implemented, as all of these algorithms were interpreted and written in-house. We

attempted to make the fairest comparison by implementing the codes as close to the publications as possible, however, it cannot be guaranteed that the same exact performance was observed. As a result, we fully acknowledge that our evaluation of these algorithms may not represent their best possible performance, although similarities such as the well-known patching artifact in CS [108, 168, 169] was also readily observed in our implementation. It would be quite valuable to compare head-to-head with the original implementations if the chance ever came up with the corresponding investigators, which could be a near-future study.

The performance of our MCIR algorithm is heavily dependent upon the quality of the FB-3DCBCT and the projection data. It was observed that when the initial quality of FB-3DCBCT is poor, that propagated through the subsequent processing with the MCIR. This is, of course, quite obvious since the MCIR algorithm updates phase-specific information from the FB-3DCBCT as its base. Therefore, to maximize the performance of MCIR, it is important to acquire high quality projection data, which will translate to high quality FB-3DCBCT. This characteristic is applicable to PICCS as well, since that algorithm also uses the FB-3DCBCT as a prior knowledge.

The MCIR algorithm involves two independent iterative steps, including 1) sub-motion-error vector, and 2) 4DCBCT calculations. In the clinical patient case, it was shown that $\leq$6 iterations were generally sufficient to calculate the sub-motion-error vector, and $\leq$80 iterations to generate the 4DCBCT. As a result, the overall overhead for computing the motion-map matrix is quite manageable.

B. Motion-map estimation

Precise motion-map estimation is also an important factor that influences the performance of the MCIR algorithm. In this study, we proposed an effective method to obtain the motion-map directly from the X-ray projection data. Results showed that in both the numerical simulations and patient case it effectively distinguished the regions that are stationary and moving. One limitation that was observed in a clinical patient case was the accuracy of the motion-map can be degraded due to a parameter that may be outside our control, which is the physical FOV size, leading to truncation errors that would accumulate during the motion-map calculations. However, as discussed, this is not a critical issue as long as the motion-map captures real mobile regions of the thoracic anatomy, which is mostly within the lungs. Since motion-map is a weighting vector designed to update FB-3DCBCT using phase-wise sorted projections that have already been reconstructed into the initial FB-3DCBCT, updating the non-moving regions with phase-wise sorted projections would have minimal effect in that region. Nevertheless, how such errors would affect the image quality needs to be rigorously validated, which will be part of our future study, as the current study mainly focused on introducing the MCIR algorithm and its concepts. In addition to this, we'll follow-up with additional methods of calculating the motion-map.

C. Regularization parameters

In the MCIR algorithm, there are two different weighting parameters that need to be assigned. That is 1) the TV regularization parameter λ [Eq.(6.3)] and 2) the 1-norm regularization parameter η [Eq.(6.7)]. The former parameter is one of the most influential parameters affecting the image quality of 4DCBCT. That is, when λ is high, the blurrier

and smoother the images, and the smaller it is, the sharper and noisier the images. This is due to the fact that λ is a weighing factor of TV regularization term in the energy function of Equation (6.3). Thus, if λ is high, more emphasis is given to minimize TV and therefore the blurrier but smoother the look. In opposite, if λ is low, then more emphasis will be given to the fidelity term (first term in Equation (6.3)) and therefore preserving the noise and high frequency information.

The latter parameter η, is the parameter that determines the sparseness of the motion map. The higher this value, more sparse the motion-map matrix (i.e., more zeros), which will emphasize the regions that has rigorous motion, while smaller this value, the motion-map matrix has less sparseness, giving non-zero values to regions that show relatively little movement. Therefore, when the *sparse* motion-map matrix, $\boldsymbol{U}$, is uploaded in MCIR, the result would be an image that rigorously emphasize only the voxels that has large data inconsistency due to motion, while other regions are left as that of FB-3DCBCT. Vise versa is true for *less sparse* motion-map matrices.

Although some investigators have proposed ways to optimize the weighing parameters (e.g., λ, η) in iterative optimization problems [26, 125], there is really no global standard in deterministically calculating them. Therefore, the selection of λ and η were subjectively picked through numerous repeat simulations. In this study, we have set $\lambda = 0.001$ and $\eta = 0.5$ for the lung cancer patient case. It is obvious that further research is needed to find a class of optimal λ and η values for various clinical sites and patient sizes, but we emphasize again that the currently study mainly focused on introducing the MCIR concept.

6.9 Conclusion

In this paper, we propose a novel 4DCBCT reconstruction algorithm utilizing a motion-map constraint as part of the framework. Up to 20 phases of clinically viable 4DCBCT images could be reconstructed while requiring no more projection data and imaging dose than a typical clinical CBCT scan. This makes our MCIR algorithm potentially useful in an on-line IGRT environment.

6.10 Acknowledgements

The text of Chapter 6, in part or in full, is a reprint of the material as it appears in the following publication:

Park JC, Kim JS, Park SH, Liu Z, Song B, Song WY. Motion-Map Constrained Image Reconstruction (MCIR): Application to Four-Dimensional Cone-Beam Computed Tomography, Submitted.

The dissertation author was the primary researcher and the co-authors listed in this publication directed and supervised the research which forms the basis for this chapter.

Chapter 7 Liver motion analysis using CBCT imager

7.1 Introduction

Stereotactic body radiation therapy (SBRT) of liver cancer is technically challenging. [170] Similar to lung cancer, there's a significant inter- and intra-fractional organ motion induced by respiration [171-174] and that radiation tolerance of normal liver is very low. [175-177] The former necessitates a use of larger margin, while the latter discourages it. To make the matter worse, the tumor itself is typically not very distinguishable against the normal liver in in-room cone beam computed tomography (CBCT) imaging, leading to uncertainties in image registration and setup. [178-181]

Since dose-response relationship exists in both primary and metastatic liver cancer, with higher dose resulting in improved outcome [182, 183], the narrowest possible safety margin is prerequisite in maximizing the therapeutic ratio. Consequently, the most accurate and precise target localization technique(s), which minimizes margin size, is essential in liver SBRT. To this end, the use of stereotactic body frame (SBF) and abdominal compression (AC) plate have been popular, in limiting most diaphragm motion to <10 mm. [184-189] Even with reduced motion, however, the problem with image registration uncertainty still remains. An effective solution to this lack of soft tissue contrast is the use of percutaneously inserted fiducial markers as a surrogate. [190-198] This approach is quite effective because the metal markers are radio-opaque and hence are readily visible in X-ray projections. Therefore, using markers to characterize the daily liver motion and subsequently adjusting the treatment setup is an effective strategy in increasing the treatment accuracy.

Having said that, a relatively little is known about the motion variations in the liver, especially within different regions in the organ. In our previous report, we have presented an effective, template-based technique in automatically extracting 2D marker positions from the X-ray projections. [194] In this study, we have used this technique to analyze the motion characteristics of liver. Using 2D positional information at each angular projection as input, we employed a robust 3D motion estimation algorithm to construct the motion traces. From such, we analyzed inter- and intra-fractional motion correlation, correlation with that of the motion acquired during 4DCT simulation, marker to marker motion variations within the liver, and variations in the gating window between fractions. With the massive motion information gathered, we systematically deduced useful information that could potentially aid in increasing the overall treatment accuracy of liver SBRT.

7.2 Patient data for liver motion analysis

The Varian Trilogy linear accelerator (Varian Medical Systems, Palo Alto, CA) with the On-Board Imager (OBI™) was used to acquire CBCT X-ray projections of 20 patients undergoing 2-8 fractions per course. Images were acquired using the *half-fan* scan mode, where ~650 projections were acquired over the 360° gantry rotation using either the *pelvis* mode (125kVp, 80mA, 13ms/frame) or the *low-dose thorax* mode (110 kVp, 20 mA, 20ms/frame). The *half-fan* mode is designed to obtain a larger field of view (FOV) especially when the size of detector cannot cover FOV of patient body. In this mode, the detector is shifted laterally to take only half of the projection of the scanned patient for each acquirement angle. This acquisition mode reconstructs FOV of about 45

cm in diameter and 15 cm in axial length. Each patient had 3 fiducial markers (2×5-mm gold) implanted around the tumor for image guidance. In total, 85 fractions with >55,000 X-ray projections were acquired.

Table.7-1. Patient characteristics data.

Patient no.	Fractions treated	Observable marker(s)	Marker distance (mm)			Target Location	Imaging protocol
			(1,2)	(1,3)	(2,3)		
1	5	3	1.9	30.0	29.1	S8	*pelvis mode*
2	2	3	2.08	22.9	21.8	S4	*pelvis mode*
3	7	3	47.7	29.7	19.0	S4, S7	*pelvis mode*
4	2	3	27.3	52.6	26.0	S1	*pelvis mode*
5	4	3	23.1	31.8	21.9	S8	*pelvis mode*
6	8	3	30.3	95.3	79.1	S2	*low-dose thorax*
7	3	2	43.1	-	-	S6, S2	*low-dose thorax*
8	3	2	25.1	-	-	S4	*low-dose thorax*
9	8	2	107.5	-	-	S3, S8	*low-dose thorax*
10	3	2	5.3	-	-	S6	*low-dose thorax*
11	4	3	19.3	27.3	15.7	S6, S7	*low-dose thorax*
12	3	1	-	-	-	S8	*low-dose thorax*
13	4	1	-	-	-	S1	*low-dose thorax*
14	4	3	24.0	39.6	36.9	S5	*low-dose thorax*
15	4	2	43.9	-	-	S4, S8	*low-dose thorax*
16	5	2	30.9	-	-	S4, S8	*low-dose thorax*
17	3	3	26.4	23.5	30.4	S4	*low-dose thorax*
18	6	3	51.9	33.0	47.9	S7	*low-dose thorax*
19	3	2	36.8	-	-	S4	*low-dose thorax*
20	4	3	74.8	90.6	23.8	S4	*low-dose thorax*

Table 7-1 provides the technical details of the patient data. Two to eight fractions were prescribed with three to four being the most popular (accounting for 12/20 cases). One to three markers were embedded in the liver, per patient, with an average of 2.45 markers, with total of 49 markers. The mean marker-to-marker distance was 36.2 mm

(range: 1.9-107.5 mm). In terms of CBCT scans, 5/20 patients were imaged with the high-dose *pelvis* mode and 15/20 patients were imaged with the *low-dose thorax* mode.

7.3 Modified marker extraction algorithm

We recently proposed a novel template-based marker extraction algorithm. [194] The algorithm is robust against any shape, size, orientation, and the number-of-seeds in an X-ray projection image. Briefly, the algorithm consists of: 1) sub-sample a small region of interest (ROI) containing all of the markers in the projection image, 2) apply edge enhancement filter using spatial derivatives to highlight the marker features, 3) calculate fast Fourier transform (FTT), enhance the marker-related signals via multiplication with FFT of an ideal marker image, and apply inverse FFT, 4) apply universal threshold to extract the *shadow* of the marker, and finally, 5) calculate the center-of-mass (COM) position of the *shadow*.

For this study, we have modified our algorithm significantly. In the original implementation, we would choose a single ROI that encompasses all of the markers. After that, the algorithm would extract all maker positions inside the ROI, simultaneously. This procedure was efficient when all markers are closely positioned with each other such that the ROI dimension did not exceed about 200×200 pixels (77.60 mm × 77.60 mm), and that patients are scanned with a high quality *pelvis* mode where the markers are clearly distinguishable from the similarly high-attenuating bones and the couch structures, at all scan angles. However, the accuracy of the algorithm fell significantly beyond the ROI dimension of 200×200 pixels, as well as when patients were imaged with the *low-dose thorax* mode, where the image noise was higher. To overcome

this, we have modified our algorithm/process in that instead of calculating multiple marker positions simultaneously, each marker was calculated separately through assigning a multiple, and much smaller ROIs (30×30 pixels, 11.64 mm × 11.64 mm). The overall workflow of the marker extraction and the subsequent respiratory signal generation procedures are illustrated in Figure 7-1. It is a semi-automatic process where we start by manually assigning the initial position of each marker at the first and the last projections. Then, the marker extraction is performed simultaneously in two opposing directions until either they meet at the last overlapping projection or terminate when the markers are absent. The reason for this approach is that, for the *half-fan* scanning geometry, there are usually a range of scan angles that do not contain the markers due to the off-center position of the detector. This angular range varies from patient to patient and from fraction to fraction, as well as from marker to marker. Therefore, it is efficient to analyze the forward and reverse directions simultaneously and is relatively easy to terminate the process when the markers disappear from the projections. Now, right after manually assigning the marker positions in the first and last projections, an ROI mask of size 30×30 pixels is centered on each marker. Then the algorithm determines the COM positions for each image. As the COM positions are determined, the ROI mask is re-centered on the new position and the search for the next COM position begins on the subsequent image. This process assumes that the marker from one projection to the next would only move within the ROI area defined. With the typical OBI frame rate of 11-12 frames/sec (0.08 sec/frame), we anticipated that it is a safe assumption to make even with abrupt change in patient motion.

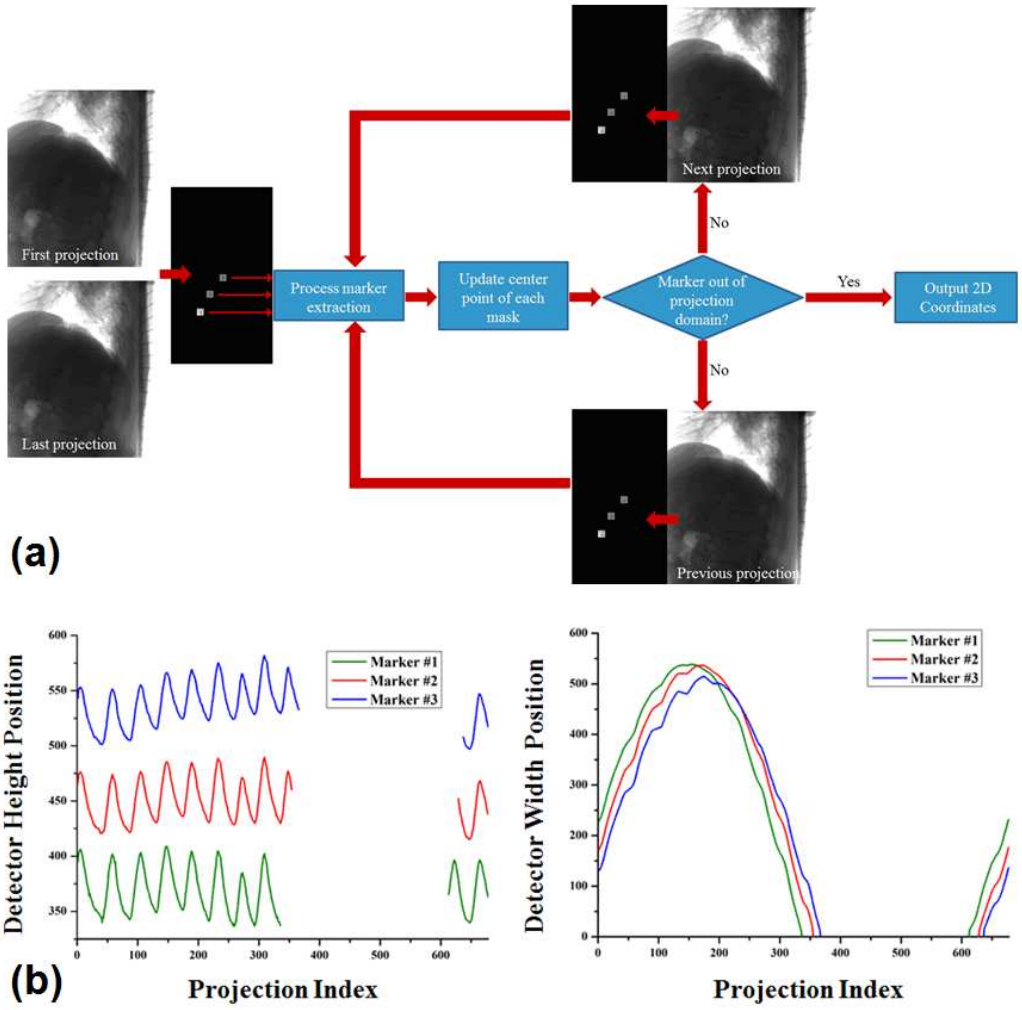

Fig. 7-1. (a) The overall workflow of the marker extraction process. The extraction is performed simultaneously in the two opposing directions until either they meet at the last overlapping projection or the markers are absent in the image. (b) The height and width positions extracted as a function of the projection angle.

7.4 3D position estimation algorithm

After identifying the 2D marker positions on all >55,000 X-ray projection images, each marker was back projected, in the room coordinate system, and the corresponding 3D position was estimated. The main idea behind this is the prior knowledge that the positions are confined within a respiratory/oscillatory motion. Assuming that patient is

immobilized while acquiring CBCT, there would be at least two or more projections at different angles imaged at same 3D position during multiple breathing cycles. Therefore, gathering marker center positions at all different angles would generate 3D distribution of marker centers which they coincide. Since motion is oscillatory, we have assumed that finding a closest point of marker center at given angle to central axis of 3D distribution would give close estimation of marker position in 3D. Such implicit assumption is valuable only if 1) breathing motion is oscillatory, 2) oscillatory motion is confined to fixed axis and 3) patient is immobilized while acquiring CBCT scan. Basically, we project each marker onto *a priori* calculated 3D axial, respiratory motion trajectory, line. And, the 3D axial line is initially calculated by fitting a line that intersects two points that correspond to the average positions of the marker in the inhalation and exhalation phases. This approach is similar to that proposed by Becker *et al*. [199] where they estimate the 3D position by: 1) sorting the marker positions into several phases, 2) each phase is grouped and back projected, 3) an average 3D point of the most-likely intersection is calculated for each phase, and 4) each marker position is then re-projected and the final 3D position is calculated by determining an orthonormal point that is closest to the average 3D position of that phase. Using this approach, the mean root mean square error was <0.4 mm on a phantom study. Once the two average points representing the two phases are calculated, a line vector intersecting the two points are obtained by the following equation (See Figure 7-2):

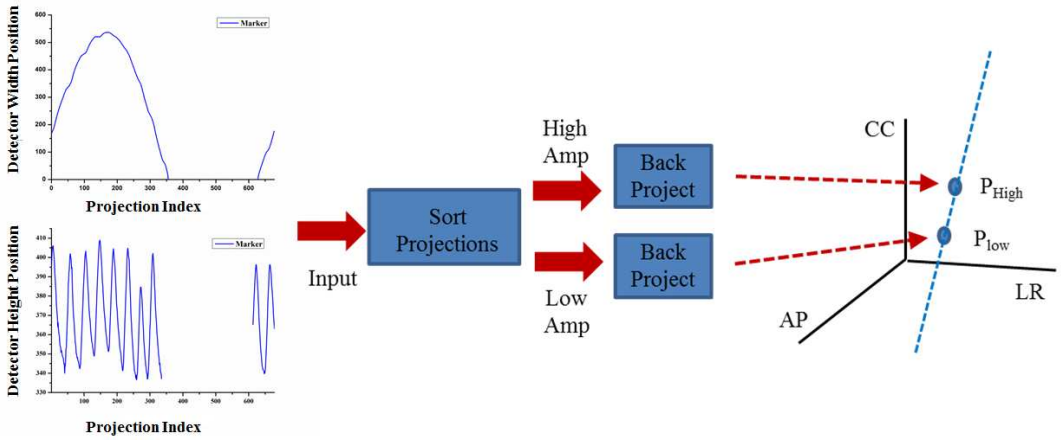

Fig. 7-2. Illustration of the process in which a 1D respiratory motion trajectory line is obtained. The projections are sorted into either a high- or low-amplitude signals. Then a line is drawn to intersect the two average points.

$$f_{axial}(\mu_{axial}) = P_{exhal}(x,y,z) + \mu_{axial}\ (P_{inhal}(x,y,z) - P(x,y,z)) \tag{7.1}$$

where variables x, y, z, f_{axial}, P_{exhal}, P_{inhal}, and μ_{axial} refer to the anterior-posterior (AP) plane, left-right (LR) plane, cranial-caudal (CC) plane, axial line function, average exhalation and inhalation positions, and a scalar weighting variable, respectively. Once the f_{axial} is derived, the next step is to project each marker again to calculate the corresponding 3D coordinate position. Projection of the 2D marker position on the detector plane to a 3D position in the room coordinate space can be first derived by drawing a line vector between the 2D marker positions to the X-ray point source. Mathematically, this can be derived by the following equation:

$$\begin{aligned} f_{fid}(\mu_{fid}) = {} & P_{fid}(x(\theta), IDD(\theta), z) \\ & + \mu_{fid}\ (P_{src}(0(\theta),\ SID(\theta), z) - P_{fid}(x(\theta), IDD(\theta), z)) \end{aligned} \tag{7.2}$$

where f_{fid}, P_{fid}, P_{src}, IDD, SID, and μ_{fid} refer to the projected line vector, the marker position in the detector plane, the X-ray source position, the isocenter-to-detector distance, the X-ray source-to-isocenter distance, and a scalar weighting variable, respectively. Note here that x, y, z coordinates are transformed, with respect to the projection angle θ, since the gantry rotates during the image acquisition. Finally, using the two line vectors obtained in Equations 7.1 and 7.2, the ultimate 3D marker position is estimated by calculating an orthonormal point that lies along the Equation 2 line and is closes to the Equation 1 line (See Figure 7-3). Mathematically, this can be solved using the following equation:

$$f_{3D\,pos}(x,y,z) = \arg\min \left\| f_{axial}(\mu_{axial}) - f_{fid}(\mu_{fid}) \right\|_2^2 \tag{7.3}$$

where $f_{3D\,pos}$(x,y,z) refers to the estimated 3D marker position. Equation 7.3 can be solved by calculating the derivative with respect to μ_{axial}, setting the equation to zero, and solving for the μ_{fid} that satisfies the equality. This calculation was performed on all markers extracted from the >55,000 projection images.

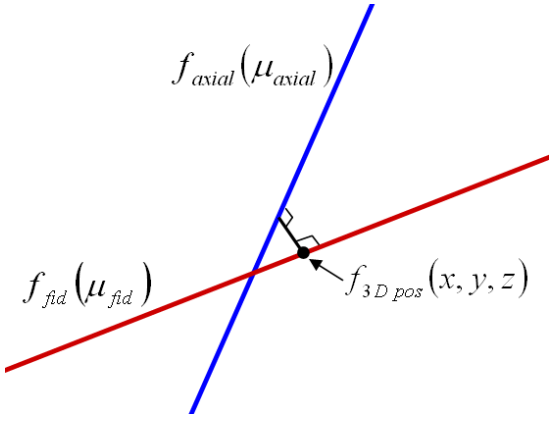

Fig. 7-3. An illustration of how a 3D marker position is estimated. An orthonormal point along the function f_{fid} is calculated that lies closest to the f_{axial} line.

7.5 Data analysis

To analyze accuracy of our modified marker tracking algorithm quantitatively, numerical simulation was performed. We have assume that cylindrically shaped marker located at beam iso-center is moving periodically with cosine wave function of 1) constant and 2) randomly varying amplitude in AP, LR and CC directions simultaneously. Knowing that total time spent to acquire CBCT with single gantry rotation is one minute, total 674 projections of digitally reconstructed radiograph (DRR) were generated to process marker extraction as well as marker tracking algorithm in *half-fan* geometry. Amplitude of motion was assumed to be 1.0 mm, 1.0 mm and 3.0 mm in AP, LR and CC directions when it was constant and 0.6 ~ 1.2 mm for AP, LR and 2.4 mm ~ 3.4 mm for CC when it was random. The breathing period of marker motion was set to be fixed at 4 seconds.

Then, based on the 3D positions estimated, we analyzed a number of liver motion characteristics. First, we evaluated the relative motion tendencies between the three primary directions: LR, AP, and CC. Second, the average and standard deviation of the breathing periods during 4DCT simulation and CBCT scans were calculated. Third, the peak-to-peak motion amplitudes in the LR, AP, and CC directions were calculated. These amplitudes were compared with that of those determined from the maximum intensity projection (MIP) CT images derived from the 4DCT planning dataset. Fourth, the appropriate gating window was retrospectively determined for each fraction. Since the marker motion is generally the greatest in the CC direction, a histogram of the marker positions in the CC direction is calculated, for each CBCT scan. Then, the (relative) gating window was defined using the following equation:

$$\text{Gating Window}(\%) = \frac{Cumul.Hist.(50\%) - Min.CC.}{Max.CC. - Min.CC.} \times 100 \tag{7.4}$$

where *Min.CC.*, *Max.CC.,* and *Cumul.Hist.*(50%), refer to the most caudal location, the most cranial location, and a median CC (z) coordinate position where 50% of the marker positions are below and above. Thus, we define the gating window to be a fraction of the length between the maximum inhalation to the maximum exhalation position that contains half of the marker postions. The algorithms and analysis were implemented on MATLAB (The MathWorks Inc., Natick, MA).

7.6 Results

A. Accuracy of marker extraction algorithm

Figure 7-4 shows the result of marker tracking algorithm where series of DRR with moving marker are extracted and tracked in 3D space. It is evident that the result of marker tracking algorithm is closely related to the motion that has been simulated for all cases. To provide the accuracy of algorithm numerically, we have calculated average relative error of motion at each LR, AP and CC direction as follows:

$$\text{Relative Error}\,(\%) = \frac{1}{\mathrm{N}} \sum_{i} \frac{(p_i - t_i)^2}{t_i^2} \times 100 \tag{7.5}$$

Where, N, i, p_{i} and t_{i} refer to number of simulated DRRs, projection index number, position of estimated marker position and position of true marker position respectively. It was found that relative error of LR, AP and CC directions were 0.68%, 0.68% and 1.69 x 10^{-7}% when amplitude was fixed and 3.35%, 1.44% and 0.01% when amplitude was randomly varying. The maximum displacement error for each direction was measured 0.07 mm (LR), 0.07 mm (AP) and 0.00013 mm (CC) when amplitude was

fixed and 0.18 mm (LR), 0.13 mm (AP) and 0.00013 mm (CC) when amplitude was varying.

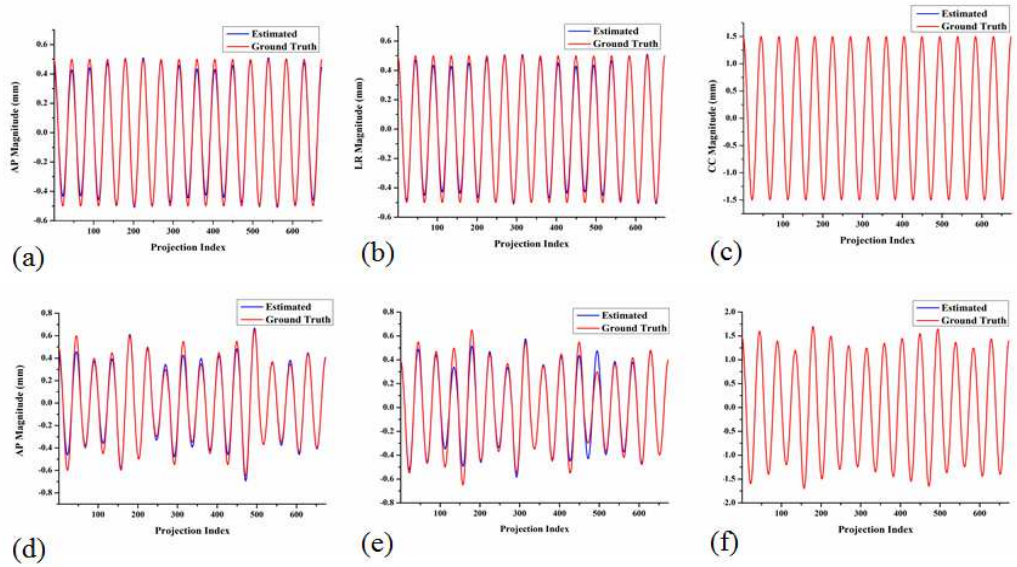

Fig. 7-4. Comparison of simulated marker tracking result with ground truth value on AP (a), LR (b), CC (c) direction with fixed amplitude breathing and AP (d), LR (e), and CC (f) direction with random amplitude breathing. Note that CC motion on both cases (c,f) appear to be single due to almost perfect match with each other.

B. Liver motion types

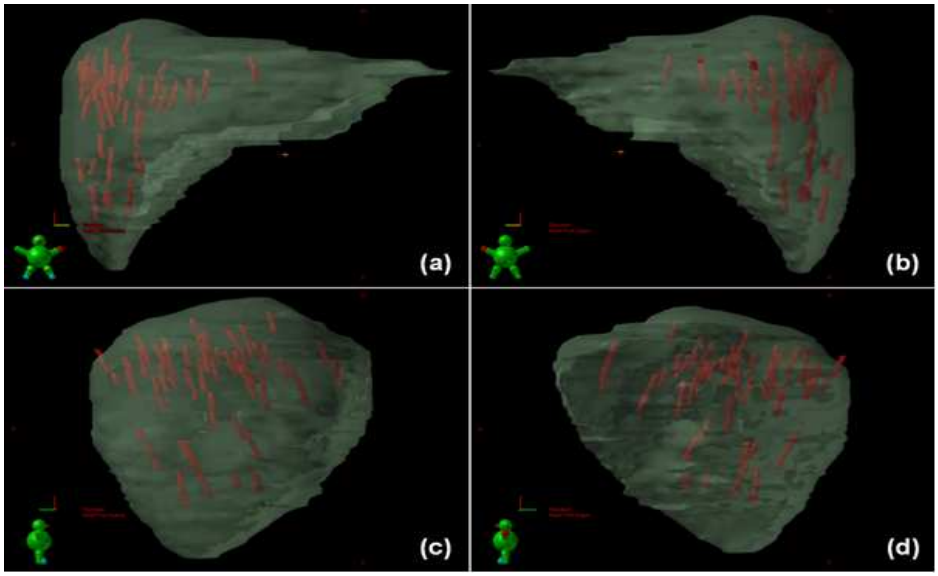

Fig. 7-5. Trajectories of all 49 markers reconstructed, during their 1st fraction CBCT scans, viewed from the (a) anterior, (b) posterior, (c) left, and (d) right beam's eye view.

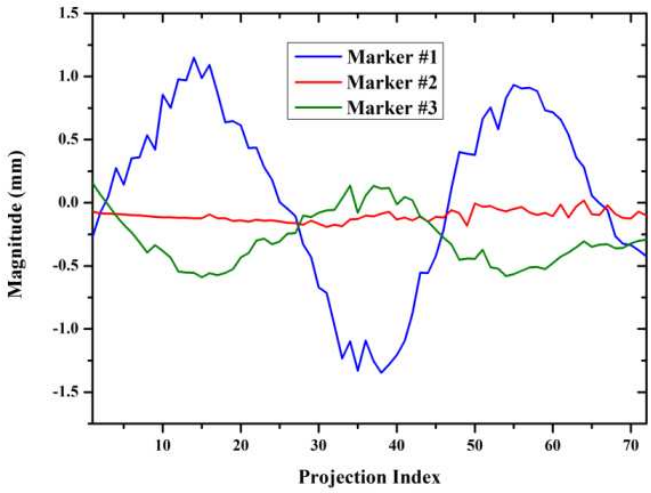

Fig. 7-6. An example patient showing the three types of LR motion with the corresponding three markers implanted.

Figure 7-5 shows the orthogonal projection views of all 49 marker trajectories, overlaid on a representative liver contour. As expected, the most dominant motion is in the CC direction. But more interestingly, there is a non-negligible motion in the AP direction as well, irrespective of their location in the liver. Also, the motion in the AP and CC directions are highly correlated. That is, when the markers move cranially, they tend to move posteriorly, and vice versa. The LR motion had a more variable relationship with the AP/CC motions, and appeared random with respect to the location. That is, when the markers moved towards cranial-posterior direction, 58% of the markers moved to the patient-right (Type I motion), 22% of the markers moved to the patient-left (Type II motion), and 20% of the markers had minimal/none motion (Type III motion). Table 7-2 list the classified motion types for each marker. The motion types were location dependent. Among the 20 patients, only 6/20 patients had all the markers show same type of motion, while 2/20 patients had all markers show different type of motion. The rest of 12/20 patients had markers that were distributed among the three motion classifications.

Figure 7-6 shows the LR motion trajectory of the three markers for a patient (#14 in Table II) illustrating all three different motions.

Table.7-2. Three types of motion relationships identified along the LR and the AP/CC directions, that is, when the marker moves towards the cranial-posterior direction, it also moves to the: (Type I) patient-right, (Type II) patient-left, and (Type III) minimal/none motion.

Patient no.	No. of markers in motion		
	Type I	Type II	Type III
1	3	-	-
2	3	-	-
3	1	-	2
4	1	2	-
5	3	-	-
6	-	1	2
7	-	1	1
8	2	-	-
9	-	1	1
10	2	-	-
11	3	-	-
12	-	-	1
13	1	-	-
14	1	1	1
15	1	-	1
16	1	-	1
17	3	-	-
18	1	1	1
19	2	-	-
20	-	3	-

C. Liver motion variability

Table 7-3 lists the comprehensive peak-to-peak amplitude, across the three dimensions, and the breathing period observed during the 4DCT simulation and the CBCT scans. Breathing period during the 4DCT scans were recorded by the RPM™ system (Varian Medical Systems, Palo Alto, CA). As observed, the CC and LR directions were generally the most and least dominant motions, respectively, except one patient (#9, marker 1) where the LR motion was significantly larger than the AP motion. The range of motion for the twenty patients were 3.00 ± 2.04 mm, 5.08 ± 3.12 mm and 17.93 ± 5.11

mm in the planning 4DCT, and 2.77 ± 1.6 mm, 5.29 ± 3.10 mm and 16.46 ± 5.69 mm in the treatment CBCT, for LR, AP, and CC directions, respectively. The range of respiratory period was 3.94 ± 0.65 and 4.18 ± 0.75 seconds during the 4DCT simulation and the CBCT scans, respectively. Some patients had a considerable disparity in motion characteristics between the simulation and treatment. The absolute difference in the motion magnitude ranged from 0.03-8.60 mm, 0.01-6.81 mm, and 0.15-9.25 mm across LR, AP, and CC directions, respectively. Correspondingly, the absolute mean difference was 0.93 ± 1.33 mm, 0.98 ± 1.12 mm and 3.37 ± 2.55 mm, respectively. It was observed that 4/20 patients had absolute motion difference in the CC direction of at least >5 mm for all markers embedded. 8/20 (40%) patients had the mean motion smaller during the CBCT scans than the 4DCT simulation, while 3/20 (15%) patients had the mean motion greater by at least 2 mm or larger. Change in breathing pattern from during the 4DCT simulation to the CBCT scans ranged from -1.99 to +1.02 seconds, with an average of -0.16 ± 0.75 seconds.

Table.7-3. The comprehensive list of peak-to-peak amplitude, across the three dimensions, and the breathing period observed during the 4DCT simulation and the CBCT scans. The two cases with the most significant inter-marker motion variations are underlined.

Patient	**Modality**	**Mean amplitude (mm ± SD)**									**Breathing Period (Sec ± SD)**
		Marker 1			**Marker 2**			**Marker 3**			
		LR	**AP**	**CC**	**LR**	**AP**	**CC**	**LR**	**AP**	**CC**	
1	MIP	5.38	8.96	27.5	4.41	9.94	27.5	2.77	8.07	25	5.15 (0.45)
	OBI	3.06 (0.52)	10.31 (1.54)	32.38 (3.25)	3.08 (0.59)	10.32 (1.58)	32.40 (3.18)	3.50 (0.71)	9.83 (1.33)	30.11 (3.55)	5.16 (0.41)
2	MIP	2.85	2.77	10	2.03	3.74	10	1.76	3.8	10	4.19 (0.39)
	OBI	2.39 (0.72)	3.89 (0.61)	12.12 (1.17)	2.37 (0.68)	3.86 (0.64)	12.08 (1.21)	2.20 (0.38)	3.75 (0.51)	12.29 (1.07)	3.60 (0.45)
3	MIP	2.75	5.51	12.5	0.98	3.67	12.5	0.98	3.67	12.5	3.90 (0.69)
	OBI	2.24 (0.51)	3.52 (0.60)	9.55 (1.38)	1.30 (0.59)	2.54 (0.58)	8.23 (1.59)	1.05 (0.62)	3.11 (0.49)	9.06 (1.25)	3.23 (0.58)

Table.7-3. Continued

Patient	Modality	Mean amplitude (mm ± SD)									Breathing Period (Sec ± SD)
		Marker 1			Marker 2			Marker 3			
		LR	AP	CC	LR	AP	CC	LR	AP	CC	
4	MIP	2.52	6.72	17.5	0.98	5.88	17.5	2.52	5.88	15	3.84 (0.47)
	OBI	1.11 (0.38)	6.39 (0.83)	16.84 (1.44)	1.8 (0.38)	6.98 (1.13)	16.43 (1.25)	3.65 (0.74)	7.10 (1.51)	13.56 (2.06)	3.92 (0.36)
5	MIP	3.53	3.53	25	0.98	3.53	22.5	0.98	2.64	22.5	4.75 (0.58)
	OBI	1.54 (0.41)	2.37 (0.41)	15.83 (0.99)	1.09 (0.37)	2.33 (0.74)	14.82 (1.03)	1.06 (0.33)	2.89 (0.54)	15.63 (1.10)	3.73 (0.44)
6	MIP	0.98	5.87	17.5	0.98	3.91	17.5	2.94	3.91	17.5	3.95 (0.13)
	OBI	0.92 (0.27)	6.41 (0.66)	18.62 (1.20)	0.95 (0.28)	6.45 (0.62)	19.11 (1.26)	3.44 (0.68)	3.07 (0.57)	18.99 (1.41)	4.58 (0.43)
7	MIP	2.36	4.72	25	0.98	4.72	22.5	0.98	5.7	22.5	3.60 (0.11)
	OBI	2.92 (0.31)	5.91 (0.43)	18.58 (1.25)	1.11 (0.84)	5.79 (0.36)	18.28 (0.89)	N/A			3.90 (0.33)
8	MIP	1.88	1.88	10	1.88	2.85	10	1.88	6.49	17.5	3.71 (0.12)
	OBI	2.54 (0.40)	2.05 (0.56)	11.74 (0.69)	4.06 (1.43)	2.73 (0.82)	10.62 (0.92)	N/A			4.16 (0.23)
9	MIP	5.68	0.98	10	2.84	1.79	20	1.90	4.79	20	4.16 (0.27)
	OBI	5.84 (1.05)	1.15 (0.52)	7.99 (0.78)	1.08 (0.35)	2.09 (0.63)	17.24 (1.82)	N/A			4.54 (0.78)
10	MIP	8.82	13.25	22.5	7.07	16.78	25	6.18	15.89	25	4.60 (0.19)
	OBI	5.97 (0.30)	12.56 (0.76)	20.96 (1.26)	7.01 (5.63)	16.28 (0.76)	23.58 (1.74)	N/A			4.72 (0.32)
11	MIP	3.84	3.84	20.00	4.73	3.78	17.50	3.79	3.78	17.50	3.93 (0.12)
	OBI	4.05 (0.28)	4.16 (0.18)	20.56 (0.87)	3.89 (0.51)	3.72 (0.80)	17.35 (1.07)	3.72 (0.29)	3.55 (0.38)	16.82 (1.03)	4.26 (0.41)
12	MIP	1.65	5.42	12.50	2.64	3.53	10.00	5.30	3.53	12.50	4.09 (0.13)
	OBI	1.15 (0.72)	5.43 (0.66)	10.62 (1.05)	N/A			N/A			4.24 (0.25)
13	MIP	3.15	5.16	20.00	8.60	4.30	22.50	6.87	5.15	17.50	3.54 (0.11)
	OBI	3.42 (0.47)	5.35 (0.70)	17.47 (1.48)	N/A			N/A			3.47 (0.25)
14	MIP	1.85	4.62	17.5	0.98	5.54	20.00	1.85	5.55	22.50	3.86 (0.12)
	OBI	1.95 (0.37)	3.70 (0.52)	15.49 (1.24)	0.92 (0.39)	3.71 (0.80)	14.88 (1.16)	0.86 (0.32)	5.51 (1.68)	15.16 (1.23)	3.61 (0.32)
15	MIP	2.67	0.98	15.00	0.98	2.67	12.50	0.98	2.67	25.00	4.59 (0.33)
	OBI	4.16 (0.42)	7.79 (0.78)	23.43 (1.32)	2.08 (0.57)	5.41 (0.34)	21.75 (1.41)	N/A			6.02 (0.21)

Table.7-3. Continued

Patient	Modality	Mean amplitude (mm ± SD)									Breathing Period (Sec ± SD)
		Marker 1			Marker 2			Marker 3			
		LR	AP	CC	LR	AP	CC	LR	AP	CC	
16	MIP	2.67	6.23	15.00	1.88	9.80	17.50	0.98	8.02	17.50	3.62 (0.53)
	OBI	2.31 (0.40)	8.16 (1.04)	16.07 (1.60)	1.40 (0.45)	7.88 (0.95)	15.18 (1.66)	N/A			3.31 (0.41)
17	MIP	4.28	3.42	15.00	4.28	3.42	15.00	6.26	3.42	15.00	3.10 (0.08)
	OBI	4.81 (1.15)	5.2 (0.53)	12.77 (1.03)	4.70 (0.88)	4.06 (0.84)	14.14 (0.89)	5.66 (1.07)	3.23 (0.44)	13.03 (1.36)	5.09 (0.64)
18	MIP	0.98	2.49	17.50	4.98	3.32	22.50	0.98	2.49	17.50	2.12 (0.22)
	OBI	1.93 (0.50)	2.53 (0.61)	12.43 (1.96)	3.05 (0.74)	3.59 (0.75)	16.47 (3.46)	1.03 (0.42)	1.96 (0.56)	11.79 (1.88)	3.29 (0.59)
19	MIP	4.48	4.48	17.50	3.59	4.49	17.50	3.58	5.38	17.50	4.17 (0.13)
	OBI	2.91 (0.34)	3.17 (0.60)	11.32 (1.05)	2.25 (0.47)	3.84 (0.68)	10.20 (1.22)	N/A			3.26 (0.21)
20	MIP	1.71	3.41	15.00	4.26	6.81	25.00	5.11	8.52	27.50	4.50 (0.32)
	OBI	1.92 (0.48)	3.96 (0.61)	14.37 (0.94)	4.51 (0.44)	9.19 (0.58)	23.62 (1.31)	5.85 (0.53)	10.53 (0.74)	24.92 (1.62)	4.52 (0.39)

Figure 7-7 illustrates inter- and intra-fractional motion variability, in CC direction, of four representative patients. As observed, there are considerable variations in the majority of patients (Figure 7-7a-c). Not only is the peak-to-peak amplitude changing between fractions, the intra-fractional breathing pattern also varies significantly (Figure 7-7c, Fraction 1). And, unless the image registration between the 4DCT (MIP) and CBCT is accurate, sometimes, the motion magnitude extends out of the margin observed in the planning MIP CT, for a significant proportion of the time (Figure 7-7a, Fractions 2-5). The most extreme case is observed in Figure 7-7c, Fraction 1, where up to 1 cm (sudden) shift in the baseline is seen accompanied by a severe irregularity in the breathing pattern. For this fraction, >7 mm deviation out of the MIP margin was observed, potentially compromising the SBRT accuracy significantly.

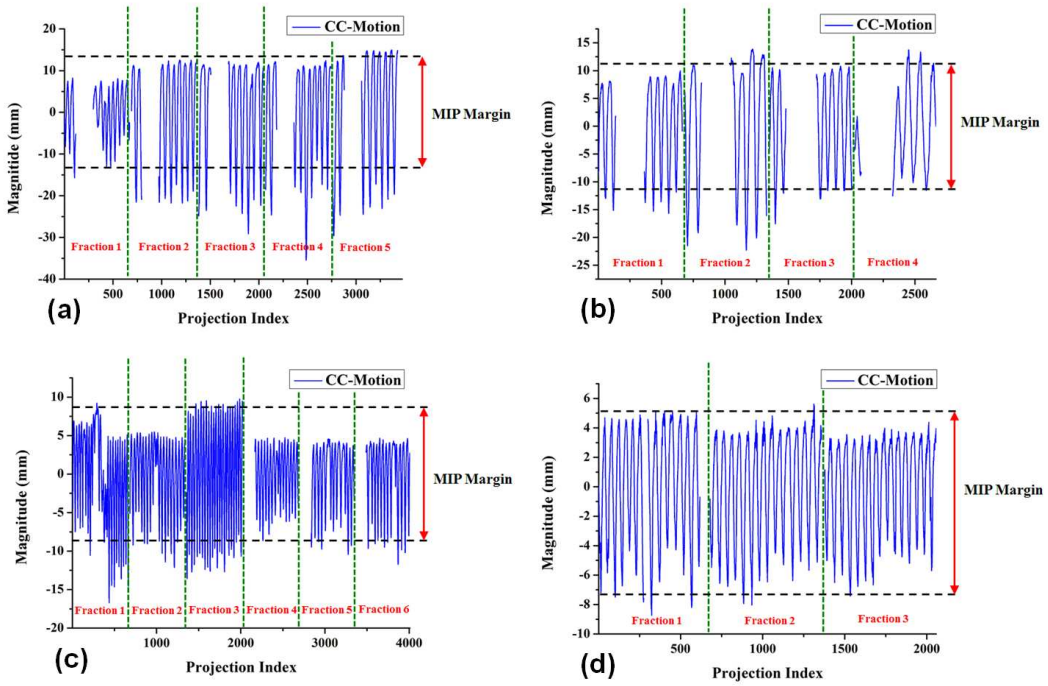

Fig. 7-7. Four representative patients illustrating the typical inter- and intra-fractional motion variations: (a) Patient #1, (b) Patient #14, (c) Patient #18, and (d) Patient #12. Also shown is the "MIP Margin" motion range determined by the planning MIP CT.

The variability in the inter-fractional motion is nicely captured by the necessary gating window needed for each fraction, as illustrated in Figure 7-8. For some patients, the fractional change in the gating window was quite significant (>20% for Patients #3, #5, #13, #14, #15, and #18), with the largest having 29.5-56.4% range between fractions (Patient #14). In all, the gating window ranged between 16.25-56.5%, for the population.

The marker-to-marker motion variability, within different locations in the liver, was also significant in some cases. Two most significant cases are underlined in Table 7-3 (Patients #9 and #20). As can be seen, the difference in the motion magnitude between the markers is nearly 1 cm, in the CC direction. Figure 7-9 shows the Patient #20 motion trajectory between the two markers. It is evident that, at all three directions, the motion magnitude differences are great, with the Marker #3 having a predominantly larger

motion. Figure 7-10 illustrates a clear trend in the absolute difference in the motion magnitude between the markers as the distance increases (R^2=0.69, linear-fit). This suggests that marker(s) in closest proximity to the target should bear more weight when performing image registration for patient setup, which also suggests that the markers should be implanted as close as possible to the gross tumor.

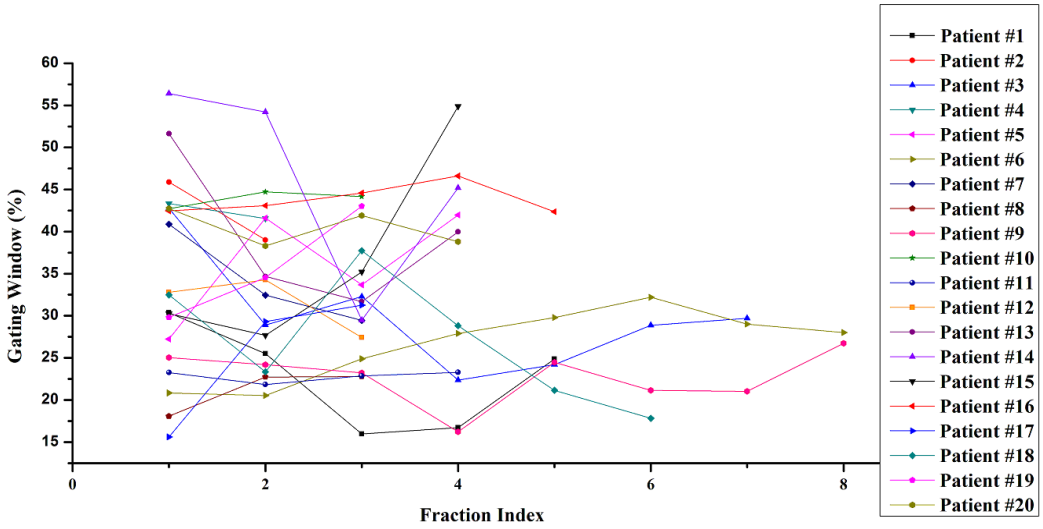

Fig. 7-8. The appropriate % gating window determined based on the marker motion trajectory of each fraction, for each patient.

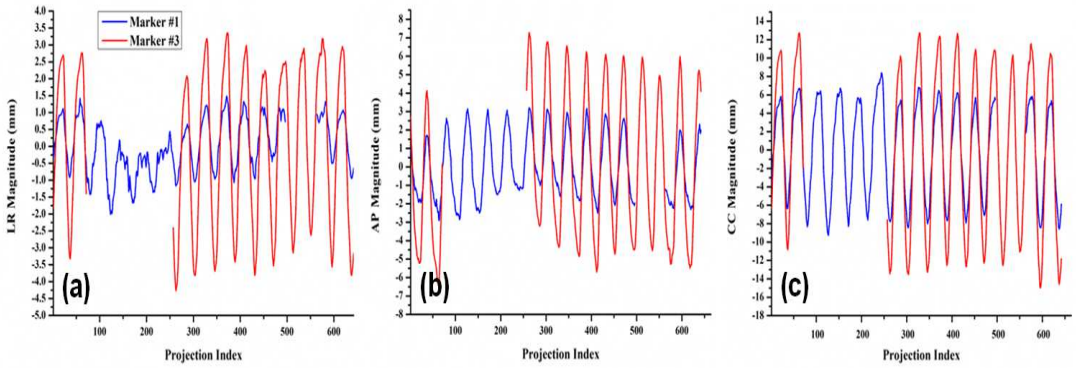

Fig. 7-9. The inter-marker motion variability in the (a) LR, (b) AP, and (c) CC directions, for Patient #20.

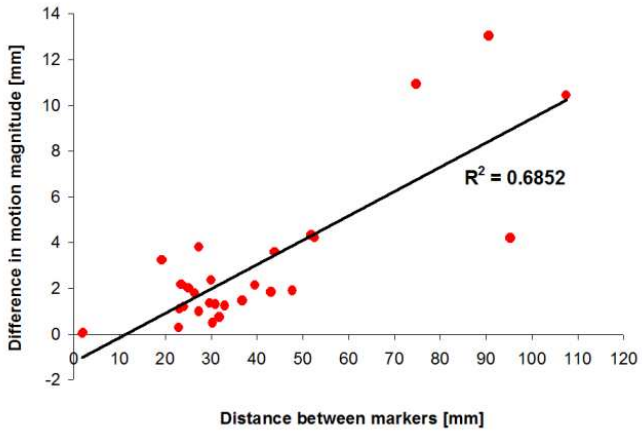

Fig. 7-10. Scatter plot showing the absolute inter-marker motion magnitude difference as a function of the marker-to-marker separation.

7.7 Discussion

A. 3D motion tracking

In liver SBRT, the fiducial markers are important due to the fact that 1) the tumor contrast is very low in the CBCT images, and 2) the motion induced by respiration is significant. This is why liver motion characterization studies have been largely performed with the markers in the past, including with the RTRT system in Japan. [191, 192, 195, 196, 198, 200, 201] For the RTRT system, using fluoroscopic imaging with multiple X-rays, the precise 3D marker positions can be extracted near real-time with sub-millimeter accuracy. Another predominant feature is that it is able to track/verify such information at all/most time during treatment. However, of course, the cost of employing such a design is the added imaging dose.

In this study, we have demonstrated that CBCT X-ray projection images can also be used to track and verify the 3D motion trajectories, as has some investigators in the past. [199, 202, 203] However, to the best of our knowledge, the use of the projections to study the motion characteristics of the liver have not been rigorously studied yet. The

main advantages of utilizing the projection images is that, first, it does not require additional hardware (if you have a CBCT system on your linear accelerator), and second, that the same projection data can be used to reconstruct a 3D image volume for image-guided radiotherapy (IGRT), thus avoiding extra imaging dose to patients. Although the projection images do not provide real-time motion information during treatment, like as in the RTRT or the CyberKnife™ systems (AccuRay, Sunnyvale, CA), the motion data it does provide, prior to the treatment, is still very valuable in understanding and guiding the patient set up [199, 202, 203], for 4DCBCT reconstructions [194], and potentially useful in various adaptive radiotherapy (ART) strategies.

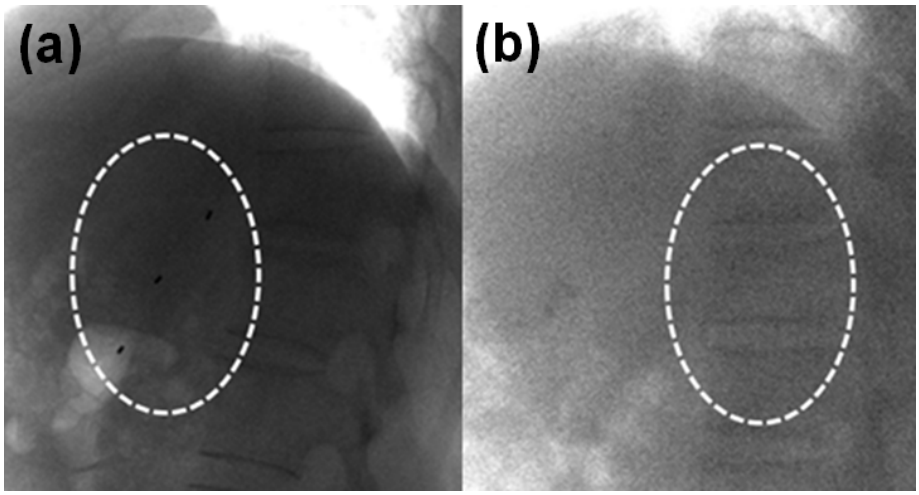

Fig. 7-11. Typical projection images taken with the (a) *pelvis* mode, and the (b) *low-dose thorax* mode. The white dotted circles indicate where the markers should be located.

In this study, a sizable portion of the markers could not be used for analysis (in 9/20 patients, only 1-2 markers were tracked, see Table 7-1), even though all patients had 3 markers implanted each. There were three main reasons for this. First, in the *half-fan* scanning geometry, due to the off-centering of the detector panel, there occasionally exist too large of scan angles with the markers being outside of the field of view (FOV).

Second, some markers were too cranially or caudally located from the isocenter and thus did not appear in the projection images. And, finally, since a large portion of the patients were imaged with the *low-dose thorax* mode (15/20 patients), some projection images were just too noisy to allow visualization of the markers (see Figure 7-11).

On validating the accuracy of our modified marker tracking algorithm, we have limited our investigation to cosine type breathing pattern at each direction (LR, AP and CC). It was found that the relative error to true motion for all directions were << 1.0% when amplitude was fixed and << 4% when amplitude was randomly varying. Moreover, the result showed that relative motion error on CC direction (motion across projection orientation) was significantly less than error on both LR and AP direction (motion along projection orientation). This has also been the observation of earlier work as well [199].

It is noted by the readers that our marker tracking algorithm is based on prior knowledge of 3D marker position gathered from 2D marker positions at all angles. Therefore, it is obvious that more consistent and regular the breathing pattern is; tracking process would more be accurate. Evaluating uncertainty of tracking algorithm with irregular breathing period or abrupt motion (e.g. cough) was beyond scope of our work. However, it is anticipated from our example study that as motion irregularity gets severe, uncertainty of tracking would also increase due to the fact that accuracy of *a priori* calculated 3D axial line (see section 7.4) is to some extent, dependent upon regularity of breathing. Nonetheless, it is entirely necessary to evaluate and improve our algorithm in such severe conditions comprehensively, which is going to be our next step.

In this study, we have limited our investigation upon fiducial markers with single sized cylindrical shaped (2×5-mm gold). The main reason for this is that entire patient

that we analyzed had fixed shaped markers implanted in them. However, we anticipate that our marker extraction as well as modified tracking algorithm would work as accurate as for different shaped or sized markers, as long as feature of marker is clearly visible and extractable from CBCT projections.

B. Liver motion

Our results indicate that, in general, the liver motion is most dominant in the CC direction, followed by the AP direction, and the LR direction. In one exceptional case (Patient #9, Marker #1), we found that the LR motion magnitude was significantly larger than the AP motion magnitude (5.84 vs 1.18 mm). In addition, the motion in the AP and CC directions were highly correlated, where, when the markers moved cranially, they moved posteriorly, and vice versa. The LR motion, however, had a more variable relationship with the AP/CC motions, and appeared random with respect to the location. Thus, since there are some correlations and some randomness to the liver motion, this suggests that a careful attention is needed in characterizing the tumor motion during the planning and the treatment processes.

There were significant motion variability observed between the 4DCT and the CBCT scans. The absolute difference in the motion magnitude ranged from 0.03-8.60 mm, 0.01-6.81 mm, and 0.15-9.25 mm across LR, AP, and CC directions, respectively. It was observed that 4/20 patients had absolute motion difference in the CC direction of at least >5 mm for all markers implanted. Changes in breathing period ranged from -1.99 to +1.02 seconds, with an average of -0.16 ± 0.75 seconds. This suggests that, for some patients, the planning 4DCT images do not accurately represent the patient motion characteristics throughout the treatments. In addition, a recent study by Vergalasova *et al*.

[204] points out that a free-breathing 3DCBCT is very limited in capturing the full range of motion, and that the appearance of the motion-blurred ITV is heavily dependent on the breathing pattern of the day. With this, and since Figure 7-7 has shown the range of possible inter- and intra-fractional variability that can be observed in the liver motion, this strongly suggests that free-breathing 3DCBCT scans may not be accurate enough in guiding the liver SBRT treatments, even with the markers implanted. Perhaps the best solution is to take 4DCBCT scans for all fractions. [194]

We also found that the motion pattern and magnitude depends strongly on the location within the liver. As Figure 10 has shown, the motion magnitude tends to be different as the distance between the markers increased. This finding is consistent with the previous works [178, 180] where the accuracy of the tumor position prediction decreases with the increasing distance between the implanted markers and the tumor. From 20 patients of analysis, we found that difference of motion was significant, when distance of separation exceeded > 7 cm. Thus, it is highly recommended that markers be implanted as closely to the gross tumor as possible (< 7cm in our study), while avoiding implanting directly in the tumor to avoid possible spread of tumor cells.

7.8 Conclusion

This study analyzed the liver motion characteristics of 20 patients undergoing SBRT. A large variation in motion was observed, inter- and intra-fractionally, and that as the distance between the markers increased, the difference in the absolute range of motion also increased. This suggests that marker(s) in closest proximity to the target be used.

7.9 Acknowledgements

The text of Chapter 7, in part or in full, is a reprint of the material as it appears in the following publication:

Park JC, Park SH, Kim JH, Yoon SM, Liu Z, Song B, Sandhu A, Jiang SB, Mell LK, Mundt AJ, Song WY. Liver motion during CBCT-guided SBRT. Medical physics 2012;39:6431-42.

The dissertation author was the primary researcher and the co-authors listed in this publication directed and supervised the research which forms the basis for this chapter.

Chapter 8 Conclusions and future work

This dissertation presents on optimizing the use of CBCT system used under IGRT settings which includes 1) improving the performance of CBCT imagers by correcting the defective pixels inherent to its frequent usage and detector fabrication process, 2) improving the quality of on-board CBCT images with respect to patient dose and respiratory motion, 3) enhancing the speed in which corresponding volumetric imaging modalities can be reconstructed and 4) proposing a way to understand the variation of inter-and intra-fractional tumor motion during the image guided treatment using CBCT system. These methodologies are anticipated to be useful to perform sophisticated radiation therapy techniques in the future which include adaptive radiation therapy, on-line re-planning, real-time dose estimation, and real-time patient monitoring.

The contribution of each chapter is addressed as follows. In chapter 2, we presented a method of identifying defective pixels in the X-ray imagers, particularly used for CBCT imaging based on wavelet analysis. The wavelet transform was applied to the gain and offset X-ray images and the sub-image represented by scaling coefficients was truncation to suppress or remove the large-scale signal variations. And then, inverse wavelet transform was applied. The reconstructed imaged filtered low-spatial-frequency components, and singularities, such as spikes and discontinuities which represent the location of defective pixels were detected. Defective pixels were corrected with simple median filter. Our approach demonstrates an approach to periodically monitor the performance of X-ray imagers and compensate the degradation of its performance due to frequent usage.

In chapter 3, we demonstrated an ultra-fast reconstruction technique for digital tomosynthesis (DTS) imaging using general-purpose graphics processing unit (GPGPU) programming interface. All the computation tasks that need to reconstruct DTS were parallelized as thread in GPU to gain massive speed-up. This resulted speed improvement of up to 87 times compared with the CPU-based implementation with visually identical images and small pixel-value discrepancies and CNR differences. With this achievement, we have shown that time allocation form DTS image reconstruction is virtually eliminated that clinical implementation of this approach has become quite appealing. In addition, with the speed achievement, further image processing and real-time applications that was prohibited prior due to time restrictions can be now tempered with.

In chapter 4, we presented a novel gradient projection algorithm, based on gradient projection Barzilai-Borwein (GP-BB), which handles the total variation (TV)-norm regularization-based least square problem for low-dose CBCT reconstruction in a highly efficient manner, with speed acceptable for routine use in the clinic. In our implementation, CBCT was reconstructed by minimizing an energy function consisting of a data fidelity term and a TV-norm regularization term. Both terms are simultaneously minimized by calculating the gradient projection of the energy function with the step size determined using an approximated Hessian calculation at each iteration, based on Barzilai-Borwein formulation. To speed up the process, the entire algorithm was designed to run with a single GPU card. With this implementation, a clinically viable patient image could be obtained ~34-78 sec while simultaneously cutting the dose by approximately 67%. This demonstrated conventionally time consuming, iterative, low-dose CBCT reconstruction potentially useful in an on-line IGRT setting.

In chapter 5, we demonstrated the method to generate breath induced motion signal of liver for reconstructing 4D DTS as well as CBCT images based on both phase wise and amplitude wise sorting of projection data. The reconstruction process was done in four steps which were 1) selecting region of interest (ROI) of fiducial marker position from projection data, 2) generating of breath induced marker motion signal based on its position and predict motion signal through signal ‘‘profiling’’ on the missing margin of marker due to limited field of view (FOV) in ‘‘half-fan’’ geometry, 3) process both amplitude wise and phase wise sorting with marker motion signal and 4) reconstruct both 4D CBCT and DTS images. With such implementation, we demonstrated that motion tracking as well as 4D reconstruction of CBCT and DTS of liver through tracking of metal markers are possible and can be directed towards utilizing the technique for on-line image-guided adaptive radiotherapy.

In chapter 6, we proposed a novel 4DCBCT reconstruction algorithm framework called Motion-Map Constrained Image Reconstruction (MCIR), that allows reconstruction of high quality and high phase resolution 4DCBCT images with no more than the imaging dose as well as projections used in a standard Free Breathing 3DCBCT (FB-3DCBCT) scan. In MCIR algorithm, the unknown 4DCBCT volume at each phase was mathematically modeled as combination of FB-3DCBCT and phase-specific update vector which has an associated motion-map matrix. The motion-map matrix, which is the key innovation of MCIR algorithm, was defined as the matrix that distinguishes voxels that are moving from stationary ones. This 4DCBCT model was then reconstructed with compressed sensing (CS) reconstruction framework such that the voxels with high motion would be aggressively updated by the phase-wise sorted projections and the

voxels with less motion would be minimally updated to preserve the FB-3DCBCT. Examination of the MCIR algorithm showed that high phase resolution 4DCBCT with sets up to 20 phases using a typical patient's FB-3DCBCT scan could be reconstructed without compromising the image quality. Moreover, both in numerical as well as in real patients' data sets, the image quality of the MCIR algorithm outperformed the other algorithms. With this achievement, we have demonstrated the potential for providing high-quality 4DCBCT information during on-line image-guided radiation therapy (IGRT) and adaptive radiation therapy (ART) environment, without sacrificing imaging dose.

In chapter 7, we have investigated motion characteristics of liver based on fiducial markers tracked with the X-ray projections of the CBCT scans, taken immediately prior to the treatments. The CBCT projections data for each fraction, for each patient, were analyzed and the 2D positions of the markers were extracted using an in-house algorithm. From the 2D extracted positions, a 3D motion trajectory of the markers was constructed, from each CBCT scans, resulting in left-right (LR), anterior-posterior (AP), and cranio-caudal (CC) location information of the markers. We then analyzed the inter- and intra-fraction liver motion variability, within different locations in the organ, and as a function of the breathing cycle. A large variation in motion was observed, inter- and intra-fractionally, and that as the distance between the markers increased, the difference in the absolute range of motion also increased. Our investigation demonstrated that that marker(s) in closest proximity to the target be used while patients are treated during CBCT guided Stereotactic body radiation therapy (SBRT) of liver cancer.

Future work includes larger clinical trials to evaluate the clinical utilities of various methods that we have proposed in this dissertation. This includes investigations

of our various volumetric reconstruction methodologies (low-dose CBCT, DTS and 4D CBCT) on 1) quantifying the improvement in patient positioning and tumor target localization accuracy, 2) usefulness in adaptive radiotherapy (ART) including on-line re-planning.

Determining the optimal CBCT scanning protocols for the use of low-dose CBCT, DTS and 4D CBCT are also promising direction to be investigated. Comprehensive analysis on what minimal number of projections, mAs, and scanning geometry can work with such reconstruction modalities and still produce reasonable quality images for clinical use needs to be done in the future studies.

Finally, we anticipate that our method of analyzing the motion trajectory of liver can be a promising tool to enable further sophisticated image guidance techniques such as real-time tumor tracking. To make such technique realizable, optimizing the computational speed and more rigorously validating accuracy as well as uncertainty of 3D position estimation algorithm is another promising direction that needs to be investigated.

References

[1] Khan FM. The physics of radiation therapy. 4th ed. Philadelphia: Lippincott Williams & Wilkins; 2010.

[2] Tyldesley S, Boyd C, Schulze K, Walker H, Mackillop WJ. Estimating the need for radiotherapy for lung cancer: an evidence-based, epidemiologic approach. International journal of radiation oncology, biology, physics 2001;49:973-85.

[3] Rontgen WK. A New Form of Radiation. Science 1896;3:726-9.

[4] Rontgen WC. On a New Kind of Rays. Science 1896;3:227-31.

[5] Curie MP, Onnes HK. The radiation of Radium at the temperature of liquid hydrogen. P K Akad Wet-Amsterd 1913;15:1430-41.

[6] Greene D, Nelson KA. Performance of a linear accelerator in clinical service. The British journal of radiology 1960;33:336-8.

[7] Holmes KS. The treatment of carcinoma of the middle ear by the 4 MV linear accelerator. Proceedings of the Royal Society of Medicine 1960;53:242-4.

[8] Lichter AS. Three-dimensional conformal radiation therapy: a testable hypothesis. International journal of radiation oncology, biology, physics 1991;21:853-5.

[9] Leibel SA, Ling CC, Kutcher GJ, Mohan R, Cordon-Cordo C, Fuks Z. The biological basis for conformal three-dimensional radiation therapy. International journal of radiation oncology, biology, physics 1991;21:805-11.

[10] Fuks Z, Leibel SA, Kutcher GJ, Mohan R, Ling CC. Three-dimensional conformal treatment: a new frontier in radiation therapy. Important advances in oncology 1991:151-72.

[11] Purdy JA. Intensity-modulated radiation therapy. International journal of radiation oncology, biology, physics 1996;35:845-6.

[12] Verellen D, Linthout N, van den Berge D, Bel A, Storme G. Initial experience with intensity-modulated conformal radiation therapy for treatment of the head and neck region. International journal of radiation oncology, biology, physics 1997;39:99-114.

[13] Xing L, Cotrutz C, Hunjan S, Boyer AL, Adalsteinsson E, Spielman D. Inverse planning for functional image-guided intensity-modulated radiation therapy. Physics in medicine and biology 2002;47:3567-78.

[14] Jaffray DA, Siewerdsen JH, Wong JW, Martinez AA. Flat-panel cone-beam computed tomography for image-guided radiation therapy. International journal of radiation oncology, biology, physics 2002;53:1337-49.

[15] Fuss M, Salter BJ, Herman TS, Thomas CR, Jr. External beam radiation therapy for hepatocellular carcinoma: potential of intensity-modulated and image-guided radiation therapy. Gastroenterology 2004;127:S206-17.

[16] Delpon G, Llagostera C, Le Blanc M, Rio E, Supiot S, Mahe MA, et al. [Use of IGRT for prostate cancers (OBI-CBCT Varian, ExacTrac BrainLAB and MVCT TomoTherapy)]. Cancer radiotherapie : journal de la Societe francaise de radiotherapie oncologique 2009;13:399-407.

[17] Xing L, Thorndyke B, Schreibmann E, Yang Y, Li TF, Kim GY, et al. Overview of image-guided radiation therapy. Medical dosimetry : official journal of the American Association of Medical Dosimetrists 2006;31:91-112.

[18] Jaffray DA. Emergent technologies for 3-dimensional image-guided radiation delivery. Seminars in radiation oncology 2005;15:208-16.

[19] Feldkamp LA, Davis LC, Kress JW. Practical Cone-Beam Algorithm. Journal of Optical Society of America A 1984;1:612-9.

[20] Wu QJ, Godfrey DJ, Wang Z, Zhang J, Zhou S, Yoo S, et al. On-board patient positioning for head-and-neck IMRT: comparing digital tomosynthesis to kilovoltage radiography and cone-beam computed tomography. International journal of radiation oncology, biology, physics 2007;69:598-606.

[21] Godfrey DJ, Yin FF, Oldham M, Yoo S, Willett C. Digital tomosynthesis with an on-board kilovoltage imaging device. International journal of radiation oncology, biology, physics 2006;65:8-15.

[22] Dobbins JT, 3rd, Godfrey DJ. Digital x-ray tomosynthesis: current state of the art and clinical potential. Physics in medicine and biology 2003;48:R65-106.

[23] Guckenberger M, Sweeney RA, Wilbert J, Krieger T, Richter A, Baier K, et al. Image-guided radiotherapy for liver cancer using respiratory-correlated computed tomography and cone-beam computed tomography. International journal of radiation oncology, biology, physics 2008;71:297-304.

[24] Sonke JJ, Zijp L, Remeijer P, van Herk M. Respiratory correlated cone beam CT. Medical physics 2005;32:1176-86.

[25] Sonke JJ, Rossi M, Wolthaus J, van Herk M, Damen E, Belderbos J. Frameless stereotactic body radiotherapy for lung cancer using four-dimensional cone beam CT guidance. International journal of radiation oncology, biology, physics 2009;74:567-74.

[26] Wang J, Guan H, Solberg T. Inverse determination of the penalty parameter in penalized weighted least-squares algorithm for noise reduction of low-dose CBCT. Medical physics 2011;38:4066-72.

[27] Ouyang L, Solberg T, Wang J. Effects of the penalty on the penalized weighted least-squares image reconstruction for low-dose CBCT. Physics in medicine and biology 2011;56:5535-52.

[28] Wierzbicki M, Schaly B, Peters T, Barnett R. Automatic image guidance for prostate IMRT using low dose CBCT. Medical physics 2010;37:3677-86.

[29] Candes EJ, Romberg J, Tao T. Robust uncertainty principles: Exact signal reconstruction from highly incomplete frequency information. IEEE Transactions on Information Theory 2006;52:489-509.

[30] Donoho DL. Compressed sensing. Ieee T Inform Theory 2006;52:1289-306.

[31] Lustig M, Donoho D, Pauly JM. Sparse MRI: The application of compressed sensing for rapid MR imaging. Magnetic resonance in medicine : official journal of the Society of Magnetic Resonance in Medicine / Society of Magnetic Resonance in Medicine 2007;58:1182-95.

[32] Jia X, Lou Y, Lewis J, Li R, Gu X, Men C, et al. GPU-based fast low-dose cone beam CT reconstruction via total variation. Journal of X-ray science and technology 2011;19:139-54.

[33] Sidky EY, Pan X. Image reconstruction in circular cone-beam computed tomography by constrained, total-variation minimization. Physics in medicine and biology 2008;53:4777-807.

[34] Niu T, Zhu L. Accelerated barrier optimization compressed sensing (ABOCS) reconstruction for cone-beam CT: phantom studies. Medical physics 2012;39:4588-98.

[35] Lauzier PT, Tang J, Chen GH. Time-resolved cardiac interventional cone-beam CT reconstruction from fully truncated projections using the prior image constrained compressed sensing (PICCS) algorithm. Physics in medicine and biology 2012;57:2461-76.

[36] Lee H, Xing L, Davidi R, Li R, Qian J, Lee R. Improved compressed sensing-based cone-beam CT reconstruction using adaptive prior image constraints. Physics in medicine and biology 2012;57:2287-307.

[37] Choi K, Wang J, Zhu L, Suh TS, Boyd S, Xing L. Compressed sensing based cone-beam computed tomography reconstruction with a first-order method. Medical physics 2010;37:5113-25.

[38] Yaffe MJ, Rowlands JA. X-ray detectors for digital radiography. Physics in medicine and biology 1997;42:1-39.

[39] Yorkston J. Recent developments in digital radiography detectors. Nuclear Instruments and Methods in Physics Research A 2007;580:974-85.

[40] Kim HK, Cunningham IA, Yin Z, Cho G. On the development of digital radiography detectors : A review. International Journal of Precision Engineeing and Manufacturing 2008;9:86-100.

[41] Gruner SM, Tate MW, Eikenberry EF. Charge-coupled device area x-ray detectors. Review of Scientific Instruments 2002;73:2815-42.

[42] Bigas M, Cabruja E, Forest J, Salvi J. Review of CMOS image sensors. Microelectronics Journal 2006;37:433-51.

[43] Chotas HG, Dobbins JT, Ravin CE. Principles of digital radiography with large-area, electronically readable detectors: A review of the basics. Radiology 1999;210:595-9.

[44] Munro P, Bouius DC. X-ray quantum limited portal imaging using amorphous silicon flat-panel arrays. Medical physics 1998;25:689-702.

[45] Farrier M, Achterkirchen TG, Weckler GP, Mrozack A. Very Large Area CMOS Active-Pixel Sensor for Digital Radiography. IEEE Transarions on Electronic Device 2009;56:2623-31.

[46] Padgett R, Kotre CJ. Assessment of the effects of pixel loss on image quality in direct digital radiography. Physics in medicine and biology 2004;49:977-86.

[47] Kim HK, Lee SC, Cho MH, Lee SY, Cho G. Use of a flat-panel detector for microtomography: A feasibility study for small-animal imaging. IEEE Transactions on Nuclear Science 2005;52:193-8.

[48] Kim HK, Yun SM, Ko JS, Cho G, Graeve T. Cascade modeling of pixelated scintillator detectors for x-ray imaging. IEEE Transactions on Nuclear Science 2008;55:1357-66.

[49] Kwan AL, Seibert JA, Boone JM. An improved method for flat-field correction of flat panel x-ray detector. Medical physics 2006;33:391-3.

[50] Davidson DW, Frojdh C, O'Shea V, Nilsson HE, Rahman M. Limitations to flat-field correction methods when using an X-ray spectrum. Nuclear Instruments and Methods in Physics Research A 2003;509:146-50.

[51] Gonzalez RC, Woods RE. Digital image processing. 3rd ed. Upper Saddle River, N.J.: Prentice Hall; 2008.

[52] Harpen MD. A computer simulation of wavelet noise reduction in computed tomography. Medical physics 1999;26:1600-6.

[53] Michail CM, Spyropoulou VA, Fountos GP, Kalyvas NI, Valais IG, Kandarakis IS, et al. Experimental and Theoretical Evaluation of a High Resolution CMOS Based Detector Under X-Ray Imaging Conditions. IEEE Transations on Nuclear Science 2011;58:314-22.

[54] Aach T, Schiebel U, Spekowius G. Digital image acquisition and processing in medical x-ray imaging. Journal of Electron Imaging 1999;8:7-22.

[55] Xu F, Liu H, Wang G, Alford BA. Comparison of adaptive linear interpolation and conventional linear interpolation for digital radiography systems. Journal of Electron Imaging 2000;9:22-31.

[56] Yan D, Vicini F, Wong J, Martinez A. Adaptive radiation therapy. Physics in medicine and biology 1997;42:123-32.

[57] Amies C, Bani-Hashemi A, Celi JC, Grousset G, Ghelmansarai F, Hristov D, et al. A multi-platform approach to image guided radiation therapy (IGRT). Medical dosimetry : official journal of the American Association of Medical Dosimetrists 2006;31:12-9.

[58] Song W, Schaly B, Bauman G, Battista J, Van Dyk J. Image-guided adaptive radiation therapy (IGART): Radiobiological and dose escalation considerations for localized carcinoma of the prostate. Medical physics 2005;32:2193-203.

[59] Fu W, Yang Y, Yue NJ, Heron DE, Huq MS. A cone beam CT-guided online plan modification technique to correct interfractional anatomic changes for prostate cancer IMRT treatment. Physics in medicine and biology 2009;54:1691-703.

[60] Bissonnette JP, Purdie TG, Higgins JA, Li W, Bezjak A. Cone-beam computed tomographic image guidance for lung cancer radiation therapy. International journal of radiation oncology, biology, physics 2009;73:927-34.

[61] Fuller CD, Scarbrough TJ, Sonke JJ, Rasch CR, Choi M, Ting JY, et al. Method comparison of automated matching software-assisted cone-beam CT and stereoscopic kilovoltage x-ray positional verification image-guided radiation therapy for head and neck cancer: a prospective analysis. Physics in medicine and biology 2009;54:7401-15.

[62] Yoo S, Yin FF. Dosimetric feasibility of cone-beam CT-based treatment planning compared to CT-based treatment planning. International journal of radiation oncology, biology, physics 2006;66:1553-61.

[63] Yang Y, Schreibmann E, Li T, Wang C, Xing L. Evaluation of on-board kV cone beam CT (CBCT)-based dose calculation. Physics in medicine and biology 2007;52:685-705.

[64] Guan H, Dong H. Dose calculation accuracy using cone-beam CT (CBCT) for pelvic adaptive radiotherapy. Physics in medicine and biology 2009;54:6239-50.

[65] Wu QJ, Thongphiew D, Wang Z, Mathayomchan B, Chankong V, Yoo S, et al. On-line re-optimization of prostate IMRT plans for adaptive radiation therapy. Physics in medicine and biology 2008;53:673-91.

[66] Wu C, Jeraj R, Lu W, Mackie TR. Fast treatment plan modification with an over-relaxed Cimmino algorithm. Medical physics 2004;31:191-200.

[67] Birkner M, Yan D, Alber M, Liang J, Nusslin F. Adapting inverse planning to patient and organ geometrical variation: algorithm and implementation. Medical physics 2003;30:2822-31.

[68] Wu Q, Liang J, Yan D. Application of dose compensation in image-guided radiotherapy of prostate cancer. Physics in medicine and biology 2006;51:1405-19.

[69] Song WY, Kamath S, Ozawa S, Ani SA, Chvetsov A, Bhandare N, et al. A dose comparison study between XVI and OBI CBCT systems. Medical physics 2008;35:480-6.

[70] Downes P, Jarvis R, Radu E, Kawrakow I, Spezi E. Monte Carlo simulation and patient dosimetry for a kilovoltage cone-beam CT unit. Medical physics 2009;36:4156-67.

[71] Ding GX, Coffey CW. Radiation dose from kilovoltage cone beam computed tomography in an image-guided radiotherapy procedure. International journal of radiation oncology, biology, physics 2009;73:610-7.

[72] Xu F, Wang J, Bai S, Li Y, Shen Y, Zhong R, et al. Detection of intrafractional tumour position error in radiotherapy utilizing cone beam computed tomography. Radiotherapy and oncology : journal of the European Society for Therapeutic Radiology and Oncology 2008;89:311-9.

[73] Ghilezan MJ, Jaffray DA, Siewerdsen JH, Van Herk M, Shetty A, Sharpe MB, et al. Prostate gland motion assessed with cine-magnetic resonance imaging (cine-MRI). International journal of radiation oncology, biology, physics 2005;62:406-17.

[74] Kerkhof EM, van der Put RW, Raaymakers BW, van der Heide UA, Jurgenliemk-Schulz IM, Lagendijk JJ. Intrafraction motion in patients with cervical cancer: The benefit of soft tissue registration using MRI. Radiotherapy and oncology : journal of the European Society for Therapeutic Radiology and Oncology 2009;93:115-21.

[75] Godfrey DJ, McAdams HP, Dobbins JT, 3rd. Optimization of the matrix inversion tomosynthesis (MITS) impulse response and modulation transfer function characteristics for chest imaging. Medical physics 2006;33:655-67.

[76] Ren L, Godfrey DJ, Yan H, Wu QJ, Yin FF. Automatic registration between reference and on-board digital tomosynthesis images for positioning verification. Medical physics 2008;35:664-72.

[77] Ren L, Yan H, Godfrey D, Yin F. A hybrid multiresolution method for automatic registration between reference and on board digital tomosynthesis. Medical physics 2007;34:2380-.

[78] Ren L, Yan H, Godfrey D, Yin F. Automatic registration between reference and on-board digital tomosynthesis for target localization of head and neck treatment. International journal of radiation oncology, biology, physics 2007;69:S682-S.

[79] Zhang J, Wu J, Godfrey DJ, Fatunase T, Marks LB, Yin FF. Comparing Digital Tomosynthesis to Cone-Beam Ct for Position Verification in Patients Undergoing Partial Breast Irradiation. International journal of radiation oncology, biology, physics 2009;73:952-7.

[80] Zhang J, Wu Q, Godfrey D, Yin F. 3D interfraction position verification for patients undergoing partial breast irradiation: Comparing digital tomosynthesis to cone-beam CT. Medical physics 2007;34:2607-.

[81] Dobbins JT, Godfrey DJ. Digital x-ray tomosynthesis: current state of the art and clinical potential. Physics in medicine and biology 2003;48:R65-R106.

[82] Godfrey DJ, Yin FF, Oldham M, Yoo S, Willett C. Digital tomosynthesis with an on-board kilovoltage imaging device. International journal of radiation oncology, biology, physics 2006;65:8-15.

[83] Wu QJ, Godfrey DJ, Wang ZH, Zhang JA, Zhou SM, Yoo S, et al. On-board patient positioning for head-and-neck imrt: Comparing digital tomosynthesis to kilovoltage radiography and cone-beam computed tomography. International journal of radiation oncology, biology, physics 2007;69:598-606.

[84] Yoo S, Wu QJ, Godfrey D, Yan H, Ren L, Das S, et al. Clinical Evaluation of Positioning Verification Using Digital Tomosynthesis and Bony Anatomy and Soft Tissues for Prostate Image-Guided Radiotherapy. International journal of radiation oncology, biology, physics 2009;73:296-305.

[85] Fuller J, Wu Q, Godfrey D, Zhang I, Wang Z, Yoo S, et al. Clinical evaluation using digital tomosynthesis for positioning verification of breath-hold liver treatment. Medical physics 2007;34:2381-.

[86] Mestrovic A, Nichol A, Clark BG, Otto K. Integration of on-line imaging, plan adaptation and radiation delivery: proof of concept using digital tomosynthesis. Physics in medicine and biology 2009;54:3803-19.

[87] Ren L, Zhang J, Thongphiew D, Godfrey DJ, Wu QJ, Zhou SM, et al. A novel digital tomosynthesis (DTS) reconstruction method using a deformation field map. Medical physics 2008;35:3110-5.

[88] Santoro J, Kriminski S, Lovelock DM, Rosenzweig K, Mostafavi H, Amols HI, et al. Evaluation of respiration-correlated digital tomosynthesis in lung. Medical physics 2010;37:1237-45.

[89] Maurer J, Godfrey D, Wang ZH, Yin FF. On-board four-dimensional digital tomosynthesis: First experimental results. Medical physics 2008;35:3574-83.

[90] Ren L, Zhang J, Thongphiew D, Wu Q, Yan H, Brizel DM, et al. Development and Clinical Evaluation of a Novel 3D Digital Tomosynthesis (DTS) Reconstruction Method using a Deformation Field Map. International journal of radiation oncology, biology, physics 2009;75:S96-S.

[91] Ren L, Zhang J, Thongphiew D, Wu Q, Godfrey DJ, Zhou S, et al. A novel digital tomosynthesis (DTS) reconstruction method using prior information and a deformation model. International journal of radiation oncology, biology, physics 2008;72:S109-S.

[92] Maltz JS, Sprenger F, Fuerst J, Paidi A, Fadler F, Bani-Hashemi AR. Fixed gantry tomosynthesis system for radiation therapy image guidance based on a multiple source x-ray tube with carbon nanotube cathodes. Medical physics 2009;36:1624-36.

[93] Xu F, Mueller K. Real-time 3D computed tomographic reconstruction using commodity graphics hardware. Physics in medicine and biology 2007;52:3405-19.

[94] Sharp GC, Kandasamy N, Singh H, Folkert M. GPU-based streaming architectures for fast cone-beam CT image reconstruction and demons deformable registration. Physics in medicine and biology 2007;52:5771-83.

[95] Xu F, Mueller K. Accelerating popular tomographic reconstruction algorithms on commodity PC graphics hardware. IEEE Transactions in Nuclear Science 2005;52:654-63.

[96] Samant SS, Xia JY, Muyan-Ozcelilk P, Owens JD. High performance computing for deformable image registration: Towards a new paradigm in adaptive radiotherapy. Medical physics 2008;35:3546-53.

[97] Gu XJ, Pan H, Liang Y, Castillo R, Yang DS, Choi DJ, et al. Implementation and evaluation of various demons deformable image registration algorithms on a GPU. Physics in medicine and biology 2010;55:207-19.

[98] Yan H, Ren L, Godfrey DJ, Yin FF. Accelerating reconstruction of reference digital tomosynthesis using graphics hardware. Medical physics 2007;34:3768-76.

[99] Yan H, Godfrey DJ, Yin FF. Fast reconstruction of digital tomosynthesis using on-board images. Medical physics 2008;35:2162-9.

[100] Cho PS, Johnson RH, Griffin TW. Cone-Beam Ct for Radiotherapy Applications. Physics in medicine and biology 1995;40:1863-83.

[101] Godfrey DJ, Ren L, Yan H, Wu Q, Yoo S, Oldham M, et al. Evaluation of three types of reference image data for external beam radiotherapy target localization using digital tomosynthesis (DTS). Medical physics 2007;34:3374-84.

[102] Siddon RL. Fast Calculation of the Exact Radiological Path for a 3-Dimensional Ct Array. Medical physics 1985;12:252-5.

[103] Otto K. Volumetric modulated arc therapy: IMRT in a single gantry arc. Medical physics 2008;35:310-7.

[104] Palma D, Vollans E, James K, Nakano S, Moiseenko V, Shaffer R, et al. Volumetric Modulated Arc Therapy for Delivery of Prostate Radiotherapy: Comparison with Intensity-Modulated Radiotherapy and Three-Dimensional Conformal Radiotherapy. International journal of radiation oncology, biology, physics 2008;72:996-1001.

[105] Park JC, Park SH, Kim JH, Yoon SM, Kim SS, Kim JS, et al. Four-dimensional cone-beam computed tomography and digital tomosynthesis reconstructions using respiratory signals extracted from transcutaneously inserted metal markers for liver SBRT. Medical physics 2011;38:1028-36.

[106] Hatton J, McCurdy B, Greer PB. Cone beam computerized tomography: the effect of calibration of the Hounsfield unit number to electron density on dose calculation accuracy for adaptive radiation therapy. Physics in medicine and biology 2009;54:N329-46.

[107] Bian J, Siewerdsen JH, Han X, Sidky EY, Prince JL, Pelizzari CA, et al. Evaluation of sparse-view reconstruction from flat-panel-detector cone-beam CT. Physics in medicine and biology 2010;55:6575-99.

[108] Chen GH, Tang J, Leng S. Prior image constrained compressed sensing (PICCS): a method to accurately reconstruct dynamic CT images from highly undersampled projection data sets. Medical physics 2008;35:660-3.

[109] Donoho DL, Elad M, Temlyakov VN. Stable recovery of sparse overcomplete representations in the presence of noise. IEEE Transactions on Information Theory 2006;52:6-18.

[110] Ritschl L, Bergner F, Fleischmann C, Kachelriess M. Improved total variation-based CT image reconstruction applied to clinical data. Physics in medicine and biology 2011;56:1545-61.

[111] Szczykutowicz TP, Chen GH. Dual energy CT using slow kVp switching acquisition and prior image constrained compressed sensing. Physics in medicine and biology 2010;55:6411-29.

[112] Tang J, Nett BE, Chen GH. Performance comparison between total variation (TV)-based compressed sensing and statistical iterative reconstruction algorithms. Physics in medicine and biology 2009;54:5781-804.

[113] Wang J, Li TF, Xing L. Iterative image reconstruction for CBCT using edge-preserving prior. Medical Physics 2009;36:252-60.

[114] Yu H, Wang G. A soft-threshold filtering approach for reconstruction from a limited number of projections. Physics in medicine and biology 2010;55:3905-16.

[115] Jia X, Lou Y, Li R, Song WY, Jiang SB. GPU-based fast cone beam CT reconstruction from undersampled and noisy projection data via total variation. Medical physics 2010;37:1757-60.

[116] Park JC, Park SH, Kim JS, Han Y, Cho MK, Kim HK, et al. Ultra-Fast Digital Tomosynthesis Reconstruction Using General-Purpose GPU Programming for Image-Guided Radiation Therapy. Technology in cancer research & treatment 2011;10:295-306.

[117] Barzilai J, Borwein JM. 2-Point Step Size Gradient Methods. Imaging Journal of Numerical Analysis 1988;8:141-8.

[118] Figueiredo MAT, Nowak RD, Wright SJ. Gradient Projection for Sparse Reconstruction: Application to Compressed Sensing and Other Inverse Problems. IEEE Jouranl of Selected Topics in Signal Processing 2007;1:586-97.

[119] Bertsekas DP. Nonlinear programming. 2nd ed. Belmont, Mass.: Athena Scientific; 1999.

[120] Grippo L, Sciandrone M. Nonmonotone globalization techniques for the Barzilai-Borwein gradient method. Comput Optim Appl 2002;23:143-69.

[121] Jia X, Lou YF, Lewis J, Li RJ, Gu XJ, Men CH, et al. GPU-based fast low-dose cone beam CT reconstruction via total variation. Journal of X-ray science and technology 2011;19:139-54.

[122] Jia X, Lou Y, Li R, Lewis J, Men C, Gu X, et al. GPU-based Fast Low Dose Cone Beam CT Reconstruction via Total Variation. International journal of radiation oncology, biology, physics 2010;78:S45-S.

[123] Xu F, Mueller K. Real-time 3D computed tomographic reconstruction using commodity graphics hardware. Physics in medicine and biology 2007;52:3405-19.

[124] Ramirez-Giraldo JC, Trzasko J, Leng S, Yu L, Manduca A, McCollough CH. Nonconvex prior image constrained compressed sensing (NCPICCS): Theory and simulations on perfusion CT. Medical physics 2011;38:2157-67.

[125] Zhu L, Xing L. Search for IMRT inverse plans with piecewise constant fluence maps using compressed sensing techniques. Medical physics 2009;36:1895-905.

[126] Paquin D, Levy D, Xing L. Multiscale registration of planning CT and daily cone beam CT images for adaptive radiation therapy. Medical physics 2009;36:4-11.

[127] Li T, Koong A, Xing L. Enhanced 4D cone-beam CT with inter-phase motion model. Medical physics 2007;34:3688-95.

[128] Lu J, Guerrero TM, Munro P, Jeung A, Chi PCM, Balter P, et al. Four-dimensional cone beam CT with adaptive gantry rotation and adaptive data sampling. Medical physics 2007;34:3520-9.

[129] Li TF, Xing L. Optimizing 4D cone-beam CT acquisition protocol for external beam radiotherapy. International journal of radiation oncology, biology, physics 2007;67:1211-9.

[130] Sonke JJ, Rossi M, Wolthaus J, van Herk M, Damen E, Belderbos J. Frameless Stereotactic Body Radiotherapy for Lung Cancer Using Four-Dimensional Cone Beam Ct Guidance. International journal of radiation oncology, biology, physics 2009;74:567-74.

[131] Case RB, Sonke JJ, Moseley DJ, Kim J, Brock KK, Dawson LA. Inter- and Intrafraction Variability in Liver Position in Non-Breath-Hold Stereotactic Body Radiotherapy. International journal of radiation oncology, biology, physics 2009;75:302-8.

[132] Bissonnette JP, Franks KN, Purdie TG, Moseley DJ, Sonke JJ, Jaffray DA, et al. Quantifying Interfraction and Intrafraction Tumor Motion in Lung Stereotactic Body Radiotherapy Using Respiration-Correlated Cone Beam Computed Tomography. International journal of radiation oncology, biology, physics 2009;75:688-95.

[133] Gierga DP, Chen GT, Kung JH, Betke M, Lombardi J, Willett CG. Quantification of respiration-induced abdominal tumor motion and its impact on IMRT dose distributions. International journal of radiation oncology, biology, physics 2004;58:1584-95.

[134] von Siebenthal M, Szekely G, Lomax AJ, Cattin PC. Systematic errors in respiratory gating due to intrafraction deformations of the liver. Medical physics 2007;34:3620-9.

[135] Shirato H, Harada T, Harabayashi T, Hida K, Endo H, Kitamura K, et al. Feasibility of insertion/implantation of 2.0-mm-diameter gold internal fiducial markers

for precise setup and real-time tumor tracking in radiotherapy. International journal of radiation oncology, biology, physics 2003;56:240-7.

[136] Kitamura K, Shirato H, Shimizu S, Shinohara N, Harabayashi T, Shimizu T, et al. Registration accuracy and possible migration of internal fiducial gold marker implanted in prostate and liver treated with real-time tumor-tracking radiation therapy (RTRT). Radiotherapy and oncology : journal of the European Society for Therapeutic Radiology and Oncology 2002;62:275-81.

[137] Dietrich L, Jetter S, Tucking T, Nill S, Oelfke U. Linac-integrated 4D cone beam CT: first experimental results. Physics in medicine and biology 2006;51:2939-52.

[138] Vedam SS, Keall PJ, Kini VR, Mostafavi H, Shukla HP, Mohan R. Acquiring a four-dimensional computed tomography dataset using an external respiratory signal. Physics in medicine and biology 2003;48:45-62.

[139] Leng S, Tang J, Zambelli J, Nett B, Tolakanahalli R, Chen GH. High temporal resolution and streak-free four-dimensional cone-beam computed tomography. Physics in medicine and biology 2008;53:5653-73.

[140] Mutaf YD, Antolak JA, Brinkmann DH. The impact of temporal inaccuracies on 4DCT image quality. Medical physics 2007;34:1615-22.

[141] Rietzel E, Chen GT. Improving retrospective sorting of 4D computed tomography data. Medical physics 2006;33:377-9.

[142] Ruan D, Fessler JA, Balter JM, Keall PJ. Real-time profiling of respiratory motion: baseline drift, frequency variation and fundamental pattern change. Physics in medicine and biology 2009;54:4777-92.

[143] Dawson LA, Jaffray DA. Advances in image-guided radiation therapy. Journal of clinical oncology : official journal of the American Society of Clinical Oncology 2007;25:938-46.

[144] Keall PJ, Mageras GS, Balter JM, Emery RS, Forster KM, Jiang SB, et al. The management of respiratory motion in radiation oncology report of AAPM Task Group 76. Medical physics 2006;33:3874-900.

[145] Kriminski S, Mitschke M, Sorensen S, Wink NM, Chow PE, Tenn S, et al. Respiratory correlated cone-beam computed tomography on an isocentric C-arm. Physics in medicine and biology 2005;50:5263-80.

[146] Li T, Xing L, Munro P, McGuinness C, Chao M, Yang Y, et al. Four-dimensional cone-beam computed tomography using an on-board imager. Medical physics 2006;33:3825-33.

[147] Lu J, Guerrero TM, Munro P, Jeung A, Chi PC, Balter P, et al. Four-dimensional cone beam CT with adaptive gantry rotation and adaptive data sampling. Medical physics 2007;34:3520-9.

[148] Sonke JJ, Lebesque J, van Herk M. Variability of four-dimensional computed tomography patient models. International journal of radiation oncology, biology, physics 2008;70:590-8.

[149] Li T, Xing L. Optimizing 4D cone-beam CT acquisition protocol for external beam radiotherapy. International journal of radiation oncology, biology, physics 2007;67:1211-9.

[150] Bergner F, Berkus T, Oelhafen M, Kunz P, Pan T, Kachelriess M. Autoadaptive phase-correlated (AAPC) reconstruction for 4D CBCT. Medical physics 2009;36:5695-706.

[151] Ahmad M, Balter P, Pan T. Four-dimensional volume-of-interest reconstruction for cone-beam computed tomography-guided radiation therapy. Medical physics 2011;38:5646-56.

[152] Leng S, Zambelli J, Tolakanahalli R, Nett B, Munro P, Star-Lack J, et al. Streaking artifacts reduction in four-dimensional cone-beam computed tomography. Medical physics 2008;35:4649-59.

[153] Li T, Koong A, Xing L. Enhanced 4D cone-beam CT with inter-phase motion model. Medical physics 2007;34:3688-95.

[154] Zhang Q, Hu YC, Liu F, Goodman K, Rosenzweig KE, Mageras GS. Correction of motion artifacts in cone-beam CT using a patient-specific respiratory motion model. Medical physics 2010;37:2901-9.

[155] Lauzier PT, Chen GH. Characterization of statistical prior image constrained compressed sensing (PICCS): II. Application to dose reduction. Medical physics 2013;40:021902.

[156] Lauzier PT, Chen GH. Characterization of statistical prior image constrained compressed sensing. I. Applications to time-resolved contrast-enhanced CT. Medical physics 2012;39:5930-48.

[157] Andersen AH, Kak AC. Simultaneous algebraic reconstruction technique (SART): a superior implementation of the art algorithm. Ultrasonic imaging 1984;6:81-94.

[158] Choi K, Wang J, Zhu L, Suh TS, Boyd S, Xing L. Compressed sensing based cone-beam computed tomography reconstruction with a first-order method. Medical physics 2010;37:5113-25.

[159] Park JC, Song B, Kim JS, Park SH, Kim HK, Liu Z, et al. Fast compressed sensing-based CBCT reconstruction using Barzilai-Borwein formulation for application to on-line IGRT. Medical physics 2012;39:1207-17.

[160] Park JC, Park SH, Kim JH, Yoon SM, Song SY, Liu Z, et al. Liver motion during cone beam computed tomography guided stereotactic body radiation therapy. Medical physics 2012;39:6431-42.

[161] Song WY, Wong E, Bauman GS, Battista JJ, Van Dyk J. Dosimetric evaluation of daily rigid and nonrigid geometric correction strategies during on-line image-guided radiation therapy (IGRT) of prostate cancer. Medical physics 2007;34:352-65.

[162] Park JC, Park SH, Kim JS, Han Y, Cho MK, Kim HK, et al. Ultra-fast digital tomosynthesis reconstruction using general-purpose GPU programming for image-guided radiation therapy. Technology in cancer research & treatment 2011;10:295-306.

[163] Qi Z, Chen GH. Extraction of tumor motion trajectories using PICCS-4DCBCT: a validation study. Medical physics 2011;38:5530-8.

[164] Park JC, Song BY, Kim JS, Park SH, Kim HK, Liu ZW, et al. Fast compressed sensing-based CBCT reconstruction using Barzilai-Borwein formulation for application to on-line IGRT. Medical physics 2012;39:1207-17.

[165] Nakagawa K, Haga A, Kida S, Masutani Y, Yamashita H, Takahashi W, et al. 4D registration and 4D verification of lung tumor position for stereotactic volumetric modulated arc therapy using respiratory-correlated cone-beam CT. Journal of radiation research 2013;54:152-6.

[166] Chen M, Siochi RA. Feasibility of using respiratory correlated mega voltage cone beam computed tomography to measure tumor motion. Journal of applied clinical medical physics / American College of Medical Physics 2011;12:3473.

[167] Guckenberger M, Weininger M, Wilbert J, Richter A, Baier K, Krieger T, et al. Influence of retrospective sorting on image quality in respiratory correlated computed tomography. Radiotherapy and oncology : journal of the European Society for Therapeutic Radiology and Oncology 2007;85:223-31.

[168] Lauzier PT, Tang J, Chen GH. Prior image constrained compressed sensing: implementation and performance evaluation. Medical physics 2012;39:66-80.

[169] Chen GH, Tang J, Leng S. Prior Image Constrained Compressed Sensing (PICCS). Proceedings - Society of Photo-Optical Instrumentation Engineers 2008;6856:685618.

[170] Benedict SH, Yenice KM, Followill D, Galvin JM, Hinson W, Kavanagh B, et al. Stereotactic body radiation therapy: the report of AAPM Task Group 101. Medical physics 2010;37:4078-101.

[171] Case RB, Moseley DJ, Sonke JJ, Eccles CL, Dinniwell RE, Kim J, et al. Interfraction and intrafraction changes in amplitude of breathing motion in stereotactic liver radiotherapy. International journal of radiation oncology, biology, physics 2010;77:918-25.

[172] Case RB, Sonke JJ, Moseley DJ, Kim J, Brock KK, Dawson LA. Inter- and intrafraction variability in liver position in non-breath-hold stereotactic body radiotherapy. International journal of radiation oncology, biology, physics 2009;75:302-8.

[173] Kitamura K, Shirato H, Seppenwoolde Y, Shimizu T, Kodama Y, Endo H, et al. Tumor location, cirrhosis, and surgical history contribute to tumor movement in the liver, as measured during stereotactic irradiation using a real-time tumor-tracking radiotherapy system. International journal of radiation oncology, biology, physics 2003;56:221-8.

[174] Nishioka T, Nishioka S, Kawahara M, Tanaka S, Shirato H, Nishi K, et al. Synchronous monitoring of external/internal respiratory motion: validity of respiration-gated radiotherapy for liver tumors. Japanese journal of radiology 2009;27:285-9.

[175] Dawson LA, Normolle D, Balter JM, McGinn CJ, Lawrence TS, Ten Haken RK. Analysis of radiation-induced liver disease using the Lyman NTCP model. International journal of radiation oncology, biology, physics 2002;53:810-21.

[176] Dawson LA, Eccles C, Craig T. Individualized image guided iso-NTCP based liver cancer SBRT. Acta Oncologica 2006;45:856-64.

[177] Pan CC, Kavanagh BD, Dawson LA, Li XA, Das SK, Miften M, et al. Radiation-associated liver injury. International journal of radiation oncology, biology, physics 2010;76:S94-100.

[178] Wunderink W, Romero AM, Seppenwoolde Y, de Boer H, Levendag P, Heijmen B. Potentials and Limitations of Guiding Liver Stereotactic Body Radiation Therapy Set-up on Liver-Implanted Fiducial Markers. International journal of radiation oncology, biology, physics 2010;77:1573-83.

[179] Romero AM, Zinkstok RT, Wunderink W, van Os RM, Joosten H, Seppenwoolde Y, et al. Stereotactic Body Radiation Therapy for Liver Tumors: Impact of Daily Setup Corrections and Day-to-Day Anatomic Variations on Dose in Target and Organs at Risk. International journal of radiation oncology, biology, physics 2009;75:1201-8.

[180] Seppenwoolde Y, Wunderink W, Wunderink-van Veen SR, Storchi P, Romero AM, Heijmen BJM. Treatment precision of image-guided liver SBRT using implanted fiducial markers depends on marker-tumour distance. Physics in medicine and biology 2011;56:5445-68.

[181] Case R, Moseley D, Bissonnette JP, Kim J, Dawson L. Variability in the amplitude of liver motion in patients undergoing Cone-Beam CT image-guided free breathing stereotactic body radiotherapy. Radiotherapy and Oncology 2007;84:S38-S.

[182] McCammon R, Schefter T, Zaemisch R, Gravdahl D, Kavanagh B. Improved local control associated with dose-escalated stereotactic body radiation therapy (SBRT) indicates dose-response relationship. International journal of radiation oncology, biology, physics 2007;69:S152-S3.

[183] Park W, Lim DH, Paik SW, Koh KC, Choi MS, Park CK, et al. Local radiotherapy for patients with unresectable hepatocellular carcinoma. International journal of radiation oncology, biology, physics 2005;61:1143-50.

[184] Herfarth KK, Debus J, Lohr F, Bahner ML, Fritz P, Hoss A, et al. Extracranial stereotactic radiation therapy: Set-up accuracy of patients treated for liver metastases. Int International journal of radiation oncology, biology, physics 2000;46:329-35.

[185] Heinzerling JH, Anderson JF, Papiez L, Boike T, Chien S, Zhang G, et al. Four-dimensional computed tomography scan analysis of tumor and organ motion at varying levels of abdominal compression during stereotactic treatment of lung and liver. International journal of radiation oncology, biology, physics 2008;70:1571-8.

[186] Wulf J, Hadinger U, Oppitz U, Thiele W, Flentje M. Impact of target reproducibility on tumor dose in stereotactic radiotherapy of targets in the lung and liver. Radiotherapy and Oncology 2003;66:141-50.

[187] Eccles CL, Dawson LA, Moseley JL, Brock KK. Interfraction Liver Shape Variability and Impact on Gtv Position during Liver Stereotactic Radiotherapy Using Abdominal Compression. International journal of radiation oncology, biology, physics 2011;80:938-46.

[188] Wunderink W, Romero AM, De Kruijf W, De Boer H, Levendag P, Heijmen B. Reduction of respiratory liver tumor motion by abdominal compression in stereotactic body frame, analyzed by tracking fiducial markers implanted in liver. International journal of radiation oncology, biology, physics 2008;71:907-15.

[189] Wulf J, Hadinger U, Oppitz U, Olshausen B, Flentje M. Stereotactic radiotherapy of extracranial targets: CT-simulation and accuracy of treatment in the stereotactic body frame. Radiotherapy and Oncology 2000;57:225-36.

[190] Wiersma RD, Mao WH, Xing L. Combined kV and MV imaging for real-time tracking of implanted fiducial markers. Medical physics 2008;35:1191-8.

[191] Shirato H, Harad T, Harabayashi T, Hida K, Endo H, Kitamura K, et al. Feasibility of insertion/implantation of 2.0-mm-diameter gold internal fiducial markers for precise

setup and real-time tumor tracking in radiotherapy. International journal of radiation oncology, biology, physics 2003;56:240-7.

[192] Shirato H, Oita M, Fujita K, Watanabe Y, Miyasaka K. Feasibility of synchronization of real-time tumor-tracking radiotherapy and intensity-modulated radiotherapy from viewpoint of excessive dose from fluoroscopy. International journal of radiation oncology, biology, physics 2004;60:335-41.

[193] Cho B, Poulsen PR, Sloutsky A, Sawant A, Keall PJ. First Demonstration of Combined Kv/Mv Image-Guided Real-Time Dynamic Multileaf-Collimator Target Tracking. International journal of radiation oncology, biology, physics 2009;74:859-67.

[194] Park JC, Park SH, Kim JH, Yoon SM, Kim SS, Kim JS, et al. Four-dimensional cone-beam computed tomography and digital tomosynthesis reconstructions using respiratory signals extracted from transcutaneously inserted metal markers for liver SBRT. Medical physics 2011;38:1028-36.

[195] Shirato H, Shimizu S, Kitamura K, Nishioka T, Kagei K, Hashimoto S, et al. Four-dimensional treatment planning and fluoroscopic real-time tumor tracking radiotherapy for moving tumor. International journal of radiation oncology, biology, physics 2000;48:435-42.

[196] Shirato H, Shimizu S, Kunieda T, Kitamura K, van Herk M, Kagei K, et al. Physical aspects of a real-time tumor-tracking system for gated radiotherapy. International journal of radiation oncology, biology, physics 2000;48:1187-95.

[197] Liu W, Wiersma RD, Mao W, Luxton G, Xing L. Real-time 3D internal marker tracking during arc radiotherapy by the use of combined MV-kV imaging. Physics in medicine and biology 2008;53:7197-213.

[198] Kitamura K, Shirato H, Shimizu S, Shinohara N, Harabayashi T, Shimizu T, et al. Registration accuracy and possible migration of internal fiducial gold marker implanted in prostate and liver treated with real-time tumor-tracking radiation therapy (RTRT). Radiotherapy and Oncology 2002;62:275-81.

[199] Becker N, Smith WL, Quirk S, Kay I. Using cone-beam CT projection images to estimate the average and complete trajectory of a fiducial marker moving with respiration. Physics in medicine and biology 2010;55:7439-52.

[200] Nishioka T, Nishioka S, Kawahara M, Tanaka S, Shirato H, Nishi K, et al. Synchronous monitoring of external/internal respiratory motion: validity of respiration-gated radiotherapy for liver tumors. Japanese Journal of Radiology 2009;27:285-9.

[201] Kitamura K, Shirato H, Seppenwoolde Y, Shimizu T, Kodama Y, Endo H, et al. Tumor location, cirrhosis, and surgical history contribute to tumor movement in the liver,

as measured during stereotactic irradiation using a real-time tumor-tracking radiotherapy system. International journal of radiation oncology, biology, physics 2003;56:221-8.

[202] Marchant TE, Amer AM, Moore CJ. Measurement of inter and intra fraction organ motion in radiotherapy using cone beam CT projection images. Physics in medicine and biology 2008;53:1087-98.

[203] Poulsen PR, Cho B, Keall PJ. A Method to Estimate Mean Position, Motion Magnitude, Motion Correlation, and Trajectory of a Tumor from Cone-Beam Ct Projections for Image-Guided Radiotherapy. International journal of radiation oncology, biology, physics 2008;72:1587-96.

[204] Vergalasova I, Maurer J, Yin FF. Potential underestimation of the internal target volume (ITV) from free-breathing CBCT. Medical physics 2011;38:4689-99.